# Development of a cluster deposition process for fabricating quantum dot composite materials

by

Shih-Tung Ngiam

B.S. Chemical Engineering-Biomedical Engineering
Carnegie-Mellon University, 1987
M.S. Chemical Engineering Practice
Massachusetts Institute of Technology, 1991

Submitted to the Department of Chemical Engineering in partial fulfillment of the requirements for the degree of

Doctor of Philosophy in Chemical Engineering

at the

Massachusetts Institute of Technology

June 1996

© Massachusetts Institute of Technology. All rights reserved.

Signature of Author: ..............................................
'hemical Engineering
April 26, 1996

Certified by: ..............................................
Klavs F. Jensen
Professor of Chemical Eng... and Engineering
...esis Supervisor

Certified by: ..............................................
... D. Kolenbrander
Associate Professor of Materials Science and Engineering
...rvisor

Accepted by: ..............................................
Robert E. Cohen
Professor of Chemical Engineering
Chairman, Committee for Graduate Students

MASSACHUSETTS INSTITUTE OF TECHNOLOGY

JUN 27 1996 Science

# Development of a cluster deposition process for fabricating quantum dot composite materials

by

Shih-Tung Ngiam

submitted to the Department of Chemical Engineering on April 26, 1996, in partial fulfillment of the requirements for the degree of Doctor of Philosophy in Chemical Engineering

## Abstract

Nanstructured composites have been fabricated by codepositing nanoclusters into solid host matrices. Ge, Si and Er nanoclusters were synthesized by Pulsed Laser Ablation-Supersonic Expansion (PLA-SSE) then codeposited into Si or $SiO_x$ hosts grown by chemical vapor deposition, laser evaporation or reactive laser evaporation.

Electron microscopy of Ge:Si composites showed that they consisted of Ge nanocrystals surrounded by a Si matrix. Rutherford Backscattering (RBS) analysis indicated a Ge content of 1 atomic percent. X-ray diffraction (XRD) showed that the Si host was polycrystalline. No photoluminescence (PL) was observed from the Ge:Si composites.

The $SiO_x$ matrices were sub-stoichiometric because of the formation of micron-scale Si particles within the $SiO_x$ host (a consequence of laser evaporation), and the low $O_2$ flux during deposition. Oxide- or hydride-passivated PLA-SSE Si clusters exhibit visible PL, but Si:$SiO_x$ composites did not exhibit any PL. This shows that Si clusters in the Si:$SiO_x$ composite are poorly passivated. Light emission by radiative recombination of excitons is suppressed in favor of non-radiative recombination at dangling bonds and defects on the surface of the Si cluster.

PL and cathodoluminescence (CL) at 1.54 µm were observed from Er:Si composites, similar to that from other Er-doped systems. The PL intensity falls by half from 4 K to 300 K. This temperature dependence is substantially smaller than that in Er-implanted crystalline Si, and the PL intensity of PLA-SSE Er:Si is greater than that of Er-implanted Si at the same temperature. High concentrations of C and O were detected in PLA-SSE Er:Si composites by Auger spectroscopy and by XPS. Complexes of Er with these two impurities have been shown to be luminescent centers in Er-implanted Si, so the enhanced PL from PLA-SSE Er:Si composites is most likely due to the presence of Er-C and Er-O complexes within the laser-evaporated Si matrix rather than to quantum confinement effects in Er nanoclusters.

Thesis Supervisor: Klavs F. Jensen
Title: Professor of Chemical Engineering and Materials Science and Engineering

Thesis Supervisor: Kirk D. Kolenbrander
Title: Associate Professor of Materials Science and Engineering

# Table of Contents

List of Figures....6
List of Tables....13
**1 INTRODUCTION....14**
1.1 Optoelectronic materials....14
1.2 Quantum dots....15
1.2.1 Quantum confinement and non-linear optics....15
1.2.2 II-VI compound semiconductor quantum dots....16
1.2.3 Group IV quantum dots....17
1.2.3.1 Si....19
1.2.3.2 Ge....20
1.3 Why quantum dot:host codeposition ?....20
**2 PULSED LASER ABLATION-SUPERSONIC EXPANSION....25**
2.1 PLA-SSE cluster source....25
2.1.1 Modelling of the PLA-SSE cluster source....27
2.2 Size selection....28
2.3 Deposition rate....29
2.4 Si nanocluster characterization....29
2.4.1 Photoluminescence....30
2.5 Ge nanocluster characterization....32
2.5.1 Photoluminescence....32
**3 HOST MATRIX DEPOSITION....38**
3.1 Chemical vapor deposition of Si....38
3.1.1 Deposition from disilane....38
3.1.2 Enhancement by Ge....40
3.2 SiO2 deposition....41
3.2.1 Tetraethylorthosilicate(TEOS)....42
3.2.2 Oxidation of silane or disilane....43
3.2.3 Physical Vapor Deposition....43
3.2.4 Active vs. passive oxidation of silicon....45
**4 Ge NANOCLUSTER:Si HOST COMPOSITES....50**
4.1 Deposition system....50
4.2 Film growth kinetics....56

4.3 Macroanalysis ....................58
4.3.1 Rutherford Backscattering Spectrometry....................58
4.4.2 X-ray diffraction....................65
4.4 Microanalysis....................67
4.4.1 Electron Microscopy ....................67
4.5 Photoluminescence....................70
4.6 Summary....................73
**5 Si NANOCLUSTER:SILICON OXIDE HOST COMPOSITES ....................75**
5.1 Silica deposition by oxidation of disilane....................75
5.2 Reactive Laser Evaporation....................76
5.2.1 Minimum oxygen flux for complete oxidation ....................78
5.2.1.1 Si flux....................78
5.2.1.2 Oxygen flux at the substrate....................79
5.3 Overall film stoichiomery ....................82
5.3.1 Factorial experiments for optimizing film stoichiometry....................82
5.4 Microstructure....................86
5.4.1 Chemical bonding....................86
5.4.1.1 X-ray Photoelectron Spectroscopy (XPS) ....................86
5.4.1.2 Silicon monoxide structure....................91
5.4.1.3 Structure of laser evaporated SiOx films....................92
5.4.1.4 Structure of SiOx films with PLA-SSE Si clusters....................95
5.4.2 Crystallinity....................96
5.4.2.1 X-ray Diffraction....................96
5.4.2.2 Scherrer formula line broadening ....................98
5.4.3 Ex-situ oxidation ....................98
5.4.3.1 Si particle size ....................102
5.5 Photoluminescence....................104
5.5.1 Ex-situ oxidation ....................104
5.6 Importance of surface passivation ....................105
5.7 Process improvements ....................105
5.8 Summary....................106
**6 Er NANOCLUSTER:Si HOST COMPOSITES....................110**
6.1 Flexibility of PLA-SSE process....................110
6.2 Er-related luminescence....................111

6.3 Double laser ablation process ........................................................ 112
6.4 Photoluminescence ........................................................ 113
6.5 Electron microscopy ........................................................ 116
6.6 Film composition ........................................................ 120
6.7 Luminescence mechanism ........................................................ 122
6.8 Suggested work ........................................................ 123
6.9 Summary ........................................................ 123
**7 SUMMARY ........................................................ 126**
**8 CONCLUSIONS ........................................................ 129**
**APPENDICES ........................................................ 130**
A.1 Disilane deposition system Standard Operating Procedure ........................................................ 130
A.2 Kinetic model for silicon deposition from Si2H6 ........................................................ 137
A.3 Kinetic model for oxidation of Si particles ........................................................ 138
A.3.1 Oxidation of planar Si wafers ........................................................ 138
A.3.2 Oxidation of spherical Si particles ........................................................ 139

# List of Figures


Figure 1.1 Density of states as a function of energy for different degrees of quantum confinement. 15

Figure 1.2 Change in optical absorption spectra of CdSe nanocrystallites with decreasing nanocrystallite diameter (from Murray, Norris and Bawendi, 1993) 17

Figure 1.3 Exciton energy as a function of quantum dot radius for Si and Ge. Right ordinate indicates the confinement energy $\Delta E$ measured from the indirect band-gap energy of the bulk material. (From Takagahara and Takeda, 1992.) 18

Figure 2.1 Schematic diagram of the Pulsed Laser Ablation-Supersonic Expansion cluster source. A pulse of He flows through the growth channel as the rotating target rod is irradiated with a 532 nm laser pulse. Evaporated material is cooled by the flowing He and condenses into a broad range of cluster sizes. The condensation reaction is then rapidly quenched by the supersonic expansion of He into the primary chamber which is at an operating pressure of $10^{-4}$ torr. 26

Figure 2.2 High Resolution Transmission Electron Microscope image of PLA-SSE Si nanocrystal collected on C-formvar coated TEM grid (from Werwa et al, 1994). 30

Figure 2.3 Photoluminescence spectrum of Si nanoclusters deposited on teflon substrate, (a) as-deposited and (b) after dipping in HF. 31

Figure 2.4 Micrographs of Ge nanoparticle collected on C-coated TEM grid at 400°C. Lattice planes are visible in the highlighted area of part (a) and are shown at higher magnification in part (b). The lattice spacing of 1.9 Å is close to the reference value of 2.0Å for Ge (220) planes (JCPDS Card 4-0545). 33

Figure 2.5 (a) XRD spectrum of PLA-SSE Ge clusters deposited on a Si (100) wafer. Peaks are seen at $2\theta$= 27.3°, 45.3° and 53.7° in curve corresponding to Ge (JCPDS card 4-545). The feature around $2\theta$ = 33.0° is the 800 Si reflection from the single crystal Si wafer substrate. Curves (b)–(d) are simulated spectra for bulk Ge, 10 nm and 5 nm diameter Ge particles respectively, illustrating the broadening of XRD lines as particle size decreases. 34

Figure 3.1 Arrhenius plot for the reaction $Si_2H_6 + O_2$ at atmospheric pressure. Silica is deposited by passing disilane(diluted to 1% in He), $O_2$ and $N_2$ at flow rates of 200, 600 and 1500 cc/min respectively over a heated Si wafer substrate. Points labelled "Photo CVD" are for photoactivated (low pressure Hg lamp) depositions. (From Mishima et al., 1984) 44

Figure 3.2 Critical presssure for transition between active and passive oxidation on Si(100). Below the curve, Si is etched by the formation of gaseous SiO, and above the curve, passive oxidation takes places with the deposition of solid $SiO_2$. 46

Figure 4.1 Pulsed Laser Ablation-Chemical Vapor Deposition (PLA-CVD) apparatus. The system consists of two diffusion-pumped vacuum chambers connected through an 8" gate valve with the PLA-SSE cluster source in the primary chamber and the disilane CVD system in the secondary chamber. 51

Figure 4.2 Schematic diagram of Pulsed Laser Ablation- Chemical Vapor Deposition apparatus. Nanoclusters are collected on a heated substrate in the secondary chamber while a silicon matrix is simultaneously deposited using disilane. The working pressure in the secondary chamber is ~$10^{-6}$ torr while the pressure in the primary chamber is ~$10^{-4}$ torr. 52

Figure 4.3 Comparison of measured growth rates of Ge cluster:Si host composites to predicted growth rates for deposition of pure Si. The Ge content of the Ge:Si composites is less than 1 atomic percent, and the composites grown at $Si_2H_6$ partial pressures of 3–6 x $10^{-6}$ torr. Model predictions were made for $Si_2H_6$ partial pressures of 1 x $10^{-6}$ torr and 5 x $10^{-6}$ torr. The standard deviation of step heights across a sample was 15%, and 2$\sigma$ error bars are shown as arrows for each experimental data point. 57

Figure 4.4 Schematic representation of an elastic collision between a projectile (of mass $M_1$, velocity $v_1$ and energy $E_0$) and a target mass $M_2$ initially at rest. Following collision, the projectile and target have velocities and energies $v_1$, $E_1$ and $v_2$, $E_2$ respectively. 59

Figure 4.5 Schematic representation of channelling effects when a major axis or plane of a single crystal is aligned along the ion beam. The surface peak is due to scattering from the outermost layer of atoms. 61

Figure 4.6 Random and aligned 2 MeV $He^+$ RBS spectra for Ge nanoclusters deposited on a Si(100) wafer without a codeposited Si host matrix. Theoretical peak locations for Si and Ge on the surface are indicated by $E_{Si}$ and $E_{Ge}$ respectively. 62

Figure 4.7 Experimental and simulated RBS spectra for Ge:Si composites. Channelled spectra for Ge:Si composites deposited (a) at 730°C for 3 hours, and (b) at 700°C for 8 hours. Simulated spectra for $Ge_{0.008}Si_{0.992}$ films (c) with a Si capping layer, (d) without a Si cap. 64

Figure 4.8 X-ray diffraction spectrum of Ge:Si composite deposited at 700°C. Bars indicate the position andrelative intensity of diffraction peaks from diamond cubic Si (JCPDS card 27-1402). Additionally there is an 800 reflection from the Si (100) substrate at 33.0° 66

Figure 4.9 STEM images of Ge:Si composite deposited at 500°C on C-coated TEM grid: (a) Annular dark field image; (b) Ge element map; (c) Si element map. The Ge and Si element maps were collected by EDS and represent the same region shown in part (a). Regions of higher Ge or Si density appear darker in parts (b) and (c) respectively. 68

Figure 4.10 High Resolution Transmission Electron Microscope image of Ge:Si composite grown at 500°C on a C-coated TEM grid. Ge (111) lattice fringes are visible with a spacing of 3.3 Å. 69

Figure 4.11 Near infrared photoluminescence spectrum for Ge:Si composite analyzed by RBS prior to PL spectroscopy. The PL behaviour shown is due to radiation-induced centers created by irradiation of the sample with $He^+$ ions during RBS analysis. Ge:Si composites which were not analyzed by RBS do not exhibit any photoluminescence. 71

Figure 5.1 Double laser ablation and oxidation. The Nd:YAG laser beam is split into two beams with one beam (25% of the original beam energy) used for PLA-SSE cluster production and another (75 %) used to laser evaporate a second Si rod placed close to the substrate. Oxygen gas is introduced through a doser and oxidizes the ablated Si to form a silicon oxide film. 77

Figure 5.2 Si deposition rate as a function of laser power. The Si matrix rod was 3.8 cm away from the quartz crystal monitor sensor head. Laser power is measured before splitting the beam, and approximately 75 % of the measured beam energy is used to ablate the Si matrix rod. Filled and open circles represent data taken on two different days. 79

Figure 5.3 Correlation between local oxygen pressure at substrate holder and overall chamber pressure. Local oxygen pressure at the substrate holder is measured with a Fast Ionization Gauge ( ○ ) or a thermocouple gauge (✕) while the chamber pressure is measured with an ionization gauge. 80

Figure 5.4 RBS spectrum of silicon oxide film deposited on (100) Si wafer. Simulated data is for a film with an O/Si ratio of 1.6 and a thickness of 0.5 μm. The film was deposited with an oxygen pressure of 5 x $10^{-4}$ torr, a laser fluence of 33 mJ/pulse and a rod-substrate distance of 3.8 cm. $E_{Si}$ and $E_O$ represent the energy of ions backscattered from Si and O, respectively, on the surface. 83

Figure 5.5 Results of a series of experiments to determine the effect of rod-substrate distance, substrate temperature, and laser power on the composition of $SiO_x$ films deposited by laser vaporization and oxidation. None of the main effects or interactions were found to be significant. The 95% confidence interval was 0.44. 84

Figure 5.6 XPS spectrum of Si wafer with native oxide. Two Si 2p peaks are seen, arising from Si atoms in the oxide layer and in the bulk Si. Spectrum was collected on SSX-100 instrument with monochromatized Al Kα X-rays. Static charge effects were corrected for by setting the adventitious carbon peak (not shown) to 284.6 eV on the binding energy scale. 90

Figure 5.7 XPS spectrum of SiOx film after smoothing and background subtraction. $SiO_x$ film was deposited at room temperature with a laser fluence of 34 mJ/pulse and an oxygen pressure of 1 x $10^{-4}$ torr onto an $Al_2O_3$ substrate. Data were collected on the PE 5100 instrument. 92

Figure 5.8 Si 2p photoelectron spectrum as a function of duration of sputtering with $Ar^+$ ions. The etch rate was approximately 20Å/min. 94

Figure 5.9 Ratio of $Si^{4+}$ to $Si^0$ in $SiO_x$ film as a function of sputter time. The $Si^{4+}/Si^0$ ratio was assumed to be equal to the the ratio of the heights of the $Si^{4+}$ and $Si^0$core-level photoelectron peaks divided by the photoionization cross-section of $Si^{4+}$ relative to $Si^0$ 95

Figure 5.10 X-ray diffraction spectra of $SiO_x$ films deposited on fused silica substrates with and without codeposited PLA-SSE Si nanoclusters. Bars indicate the position andrelative intensity of diffraction peaks from diamond cubic Si (JCPDS card 27-1402). The broad background peak arises from the amorphous fused silica substrate. 97

Figure 5.11 Comparison of $SiO_x$ XRD spectrum to simulated diffraction patterns for Si particles of various sizes. Bottom curve, (a), is that of $SiO_x$ following subtraction of the background signal from the fused silica substrate. Remaining curves are simulated spectra for (b) bulk Si and (c) 10 nm, (d) 5 nm and (e) 3 nm diameter Si particles. 99

Figure 5.12 Time for complete oxidation of a spherical Si particle as a functior of its initial diameter and temperature. Oxidation is carried out in dry $O_2$ at atmospheric pressure. 100

Figure 5.13 X-ray diffraction spectra for $SiO_x$ deposited with Si nanoclusters on a Si wafer following 0, 2 and 5 hours of oxidation at 1000°C. XRD signal from the Si (100) single crystal substrate was suppressed by slightly misorienting the wafer with respect to the diffractometer plane, but some traces of the Si 800 reflection remain around $2\theta = 33°$. Diffraction peaks from Si particles in the deposited $SiO_x$ film remain even after 5 hours of oxidation. 101

Figure 5.14 SEM micrograph of $SiO_x$ film deposited on a Si wafer. The micron-scale particles are characteristic of laser deposition and are due to liquid droplets hitting the substrate surface. 103

Figure 6.1 Double laser ablation process for codepositing Er nanoclusters in a Si host matrix. The Nd:YAG laser beam is split into two beams with one beam (25% of the original beam energy) used in the PLA-SSE cluster source and another (75 %) used to laser evaporate a second Si rod placed close to the substrate. 112

Figure 6.2 Photoluminescence spectra of Er:Si composite before and after a 30 minute anneal in Ar at 500°C. Luminescence from C and O impurity centers is eliminated, while Er-related luminescence is enhanced by annealing. 114

Figure 6.3 Integrated PL intensity as a function of annealing temperature. All anneals are carried out in Ar for 30 minutes. PL spectra were collected at 300 K and 4K. 115

Figure 6.4 SEM micrograph of Er:Si composite deposited on a Si wafer at room temperature for 3 hours. Sample is viewed from the edge at an angle of 15°, and the open area to the right is a portion of the substrate which was masked during deposition. The striated cones are formed by the rapid solidification of liquid Si droplets, and the discs formed by Si droplets which cool off more slowly. The smaller spheres are most likely Er particles. 116

Figure 6.5 SEM image and EDS element maps of an Er:Si composite deposited at room temperature for 3 hours on a Si substrate. (a) SEM image; (b) Er L X-ray map; (c) Si K X-ray map. Areas of higher concentration appear brighter in the element maps. 118

Figure 6.6 Cathodoluminescence map and SEM image of Er:Si composite. Light emission is strongest from cones formed by the rapid solidification of liquid Si droplets. The dark spot in the upper left quadrant of part (a) correponds to an Er particle, seen as a bright sphere in part (b). 119

Figure A.1 Disilane gas handling system 131

Figure A.2 Schematic representation of $O_2$ concentration, $c$, as a function of radius, $r$, for a spherical particle undergoing thermal oxidation and consisting of an unreacted Si core surrounded by a $SiO_2$ shell. $c_i$, $c^*$ and $c_g$ are the concentration of $O_2$ at the Si-$SiO_2$ interface, gas-solid interface, and bulk gas respectively. $\delta$ is the thickness of the oxide layer. 140

# List of Tables

| | | |
|---|---|---|
| Table 4.1 | RBS parameters for selected elements using 2 MeV He2+ projectiles with a backscattering angle of 180°. All values were calculated using average atomic masses based on the natural isotopic distributions of the respective elements. | 60 |
| Table 5.1 | Deposition conditions used in factorial experiment for optimizing O/Si ratio. | 84 |

# Chapter 1
# Introduction

This work is motivated by the search for photonic and optoelectronic materials which could overcome some of the limitations of current electronic materials. A promising avenue for this search is the development of "quantum dots," i.e., materials whose dimensions are comparable to the Bohr radius of electron-hole pairs. Semiconductor quantum dots have been synthesized by several methods, including Pulsed Laser Ablation-Supersonic Expansion (PLA-SSE), and these quantum dots possess interesting optical properties which may be applicable to the development of optoelectronic and photonic materials. For practical purposes, the quantum dots should be combined with another material which controls the quantum dot's environment and which is compatible with existing microelectronic processes. This thesis therefore focuses on the codeposition of PLA-SSE quantum dots in Si and $SiO_2$ host matrices.

## 1.1 Optoelectronic materials

Since the advent of the silicon integrated circuit in the 1960s, the microelectronics industry has maintained a remarkable pace of technological advance, rapidly increasing the speed and power of computers while simultaneously reducing their size and cost.[1] Fundamental limits of semiconductor electronics technology are being approached, however, both in terms of size and speed. Photonic, i.e. light-based, devices could provide an alternative to electronic devices because much higher speeds are theoretically possible than with electronic devices.[2] For the promise of photonics to be realized, a new generation of photonic and optoelectronic materials has to be developed. Optoelectronic materials would be used as interfaces between photonic and electronic systems, similar to III-V devices used today to bridge electronic and optical transmission in fibre-optic communication devices. Optoelectronic materials would also be used in displays such as light-emitting diodes and flat panel displays.

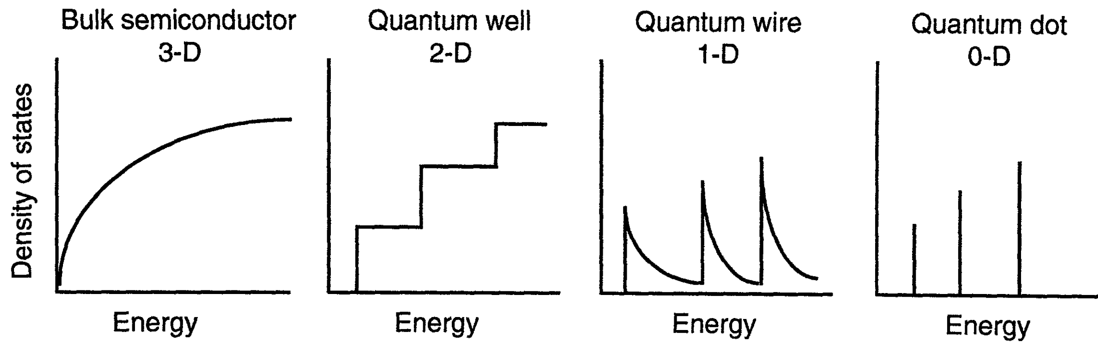


Figure 1.1 Density of states as a function of energy for different degrees of quantum confinement.

## 1.2 Quantum dots

One promising approach to developing optoelectronic and photonic materials has been to use materials in which electrons are confined to a space comparable to the size of electron-hole pairs (excitons). When the material is quantum confined in one-dimension, the electrons are free to move in only two dimensions, and the material is known as a "quantum well." Quantum well devices made of stacks of thin layers of III-V semiconductors are in commercial production and are used as laser diodes or light emitting diodes.[3-6] Materials which are quantum confined in three dimensions are known as "quantum dots" and have been shown in the laboratory to have strongly enhanced non-linear optical properties.[7,8] Quantum dot materials are thus the focus of this research effort.

### 1.2.1 Quantum confinement and non-linear optics

In a bulk semiconductor, the physical properties are largely determined by the periodic nature of the lattice. This gives rise to the band structure of the semiconductor, the electron effective mass and other properties. For a large crystal the overall shape and size have no effect on the physical properties. As the dimensions of the crystallite are reduced until they become comparable to the exciton radius, however, the free carriers become "aware" of the crystal boundaries.[9] The electron and hole wavefunctions must go to zero outside the crystallite, imposing a boundary condition similar to that in

the particle-in-a-box solution to the Schrödinger equation. Discrete molecule-like energy levels are therefore observed in quantum dots rather than continuous energy levels such as those observed in bulk semiconductors. This is illustrated in Figure 1.1 which shows the change in the density of states as the degree of quantum confinement increases.[7,10,11] The density of states, $Z$, is $dN/dE$, where $N$ is the number of states of energy $E$. In a bulk semiconductor, the density of states varies continuously with electron energy, $Z \propto E^{1/2}$ . A two-dimensional quantum well is confined in one dimension and the density of states becomes a step function. A quantum wire is confined in two dimensions and also has sharp steps with $Z \propto E^{-1/2}$ in between the steps. A zero-dimensional quantum dot is confined in all three dimensions and the density of states separates into a discrete set of energy levels. The sharp density of states with finite magnitudes results in non-linear optical properties such as sharp resonances and saturable absorption which could be utilized in a photonic device such as an optical switch.[9,10] Additionally, the allowed energy levels are size-dependent so the optical properties of quantum dots are tunable by varying the size of the dot.

### 1.2.2 II-VI compound semiconductor quantum dots

The best developed technique for synthesizing semiconductor quantum dots is probably the controlled precipitation of II-VI compounds in solution developed by Steigerwald, Brus, Bawendi and co-workers.[12-15] The size of the nanocrystallites is controlled by varying the temperature and time of reaction, and then further refined by size-selective precipitation so that size distributions < 5 % r.m.s. in diameter are routinely achieved. Quantum confinement effects are observed in Figure 1.2 which shows the evolution in absorption spectra with size for CdSe nanocrystallites.[14] Photoluminescence spectra for the CdSe nanocrystallites are also size-dependent and blue-shift with decreasing crystallite size.[16] This shows that the optical properties of the quantum dots can be manipulated by controlling the size of the quantum dots.

A key element of this synthesis technique is the presence of capping groups, e.g., Tri-*n*-octylphosphine (TOP)/Tri-*n*-octylphosphine oxide (TOPO), on the surface of the crystallites that control the reaction rate, and hence the size of the crystallites, and also allows for further manipulation of the size

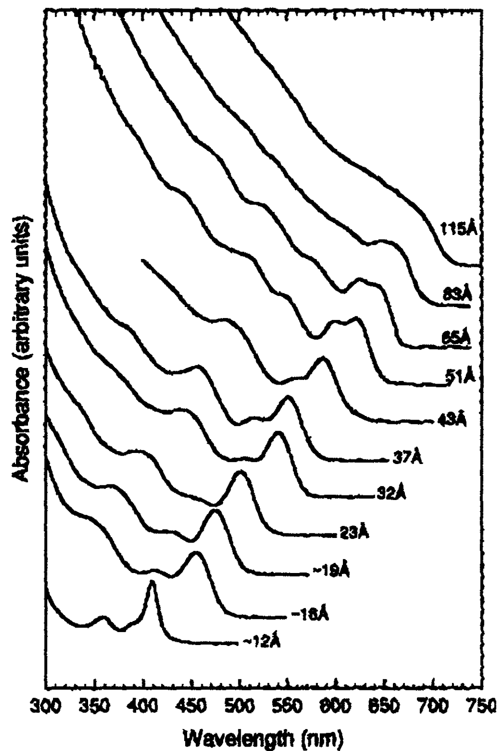


Figure 1.2 Change in optical absorption spectra of CdSe nanocrystallites with decreasing nanocrystallite diameter (from Murray, Norris and Bawendi, 1993)

distribution through the size-selective precipitation step. Photoluminescent and electroluminescent devices have been fabricated from CdSe quantum dots, and the luminescence is tunable by varying the size of the quantum dots.[16]

### 1.2.3 Group IV quantum dots

Si and Ge are indirect-gap semiconductors, unlike GaAs and CdSe, which are direct-gap semiconductors. In direct-gap materials the bottom of the conduction band and the top of the valence band lie at $\mathbf{k} = 0$, where $\mathbf{k}$ is the crystal momentum.[17] An excited electron in the conduction band minimum can spontaneously recombine with a hole in the valence band, emitting a photon of energy equal to the band gap. Direct gap materials are thus efficient light emitters. In indirect-gap materials, however, the conduction band minimum occurs at $\mathbf{k} \neq 0$. An electron cannot make a direct transition from

the bottom of the conduction band to the top of the valence band because momentum would not be conserved in such a transition. For electron-hole recombination to occur, the momentum of the initial conduction band state must be transferred to the crystal through the creation of a phonon. This three-body event (electron, hole and phonon) is much less likely to occur than a direct electron-hole recombination, so indirect gap materials are very inefficient light emitters. Electrons and holes in Si are thefore more likely to recombine by non-radiative processes (e.g., recombination at defects/deep traps and Auger recombination)[18] than by radiative processes.

In a quantum dot, the electron and hole wavefunctions are confined in real space so that qualitatively, the wavefunctions spread out in momentum space through the Heisenberg uncertainty relation.[19,20] Conservation of momentum is lifted and Si quantum dots become pseudo-direct gap materials. Si quantum dots could thus become efficient light emitters. In addition, Takagahara and Takeda[21] have calculated that the exciton energy in

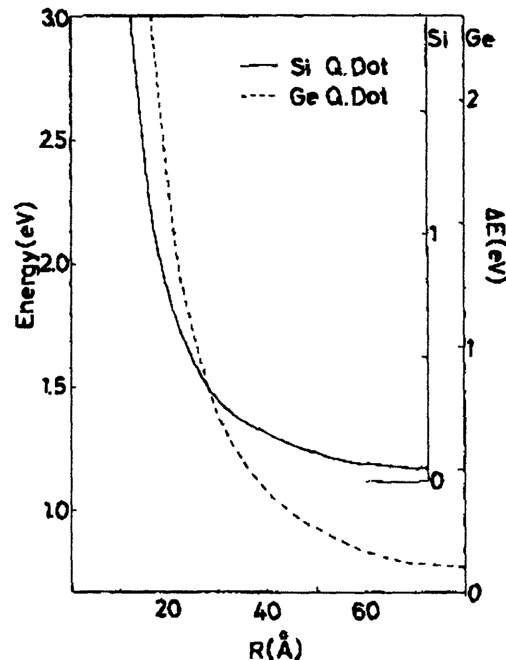


Figure 1.3 Exciton energy as a function of quantum dot radius for Si and Ge. Right ordinate indicates the confinement energy ΔE measured from the indirect band-gap energy of the bulk material. (From Takagahara and Takeda, 1992.)

nanocrystalline Si increases with decreasing crystallite size, as shown in Figure 1.3 Emission from Si could thus takes place in the visible rather than infra-red portion of the spectrum.† This would make quantum confined Si potentially useful as a display material.

1.2.3.1 Si

Visible photoluminescence and electroluminescence have been observed from Si-based materials synthesized by a variety of methods including electrochemical etching (porous Si),[22] aerosol synthesis with size-selective chromatography,[23,24] precipitation from Si-rich glass,[25,26] and Pulsed Laser Ablation-Supersonic Expansion (PLA-SSE).[27,28] Nanocrystalline Si has been identified as the luminescing center in all these materials, and quantum confinement has been shown to play a role in the mechanism, although the details of the mechanism are still under debate.[18,29,30] The PL behaviour of PLA-SSE Si nanocrystals is substantially similar to that of the Brus material and to porous Si, suggesting a common origin – namely, quantum confined Si, for light emission from all these materials.

For PLA-SSE Si nanocrystals, the photoluminescence peak shifts to lower wavelengths for smaller Si nanocrystals but the spectrum is broad with FWHM ~ 100 nm due to a wide particle size distribution (see Section 2.4.1) Si nanoclusters were collected directly on TEM grids coated with amorphous carbon and formvar, and examined with a high resolution TEM.[19] Figure 2.2 shows a crystalline Si particle approximately 3 nm in diameter. The lattice fringes have a spacing of 1.6 Å, corresponding to the (311) lattice spacing of diamond cubic Si (JCPDS Card 27-1402).[50] A wide distribution of particle sizes, with diameters ranging from 2 nm to several hundred nanometers, was also observed.

In all of these materials, surface passivation is shown to be essential for enabling photoluminescence from the Si nanocrystallites. Otherwise, non-radiative recombination at surface defects and deep traps will be favoured, and will extinguish the luminescence.[18,31,32]

† The indirect band gap of bulk Si is 1.12 eV, equivalent to 0.9 μm, in the near-infra-red.

#### 1.2.3.2 Ge

Like Si, Ge is an indirect gap semiconductor that is ordinarily an inefficient light emitter.[19] Because the effective masses of electrons and holes are smaller in Ge than in Si, the exciton Bohr radius is larger in Ge than in Si.[10] Quantum confinement effects are therefore expected to be larger in Ge than in Si for crystallites of the same size (Figure 1.3).[21] For example, a confinement energy of 0.5 eV is calculated for 75Å diameter Ge particles but a similar magnitude effect is not seen in Si until the particles are smaller than 45 Å. Photoluminescence has been reported from Ge nanocrystals embedded in $SiO_2$ matrices, synthesized by ion implanting Ge into $SiO_2$ or co-sputtering Ge and $SiO_2$ then precipitating Ge nanocrystals by heat treatment.[33-36] Heath and co-workers[37,38] have used an inorganic solution-phase technique to synthesize colloids of Ge nanocrystals with sizes ranging from 60–200 Å. Strong size effects are observed in the optical absorption spectra of the Ge nanocrystal colloids, but no photoluminescence has yet been reported.

## 1.3 Why quantum dot:host codeposition ?

The properties of quantum dots are thus seen to be strongly dependent on their size distribution and degree of surface passivation. In addition, for quantum dots to be integrated into contemporary microelectronic devices, they would have to be compatible with existing semiconductor systems. This would require a means of binding the quantum dots in a film that adheres to semiconductor wafers and that can be fabricated with contemporary semiconductor processing technology. The matrix material would also have to control the surface chemistry of the quantum dots so that desired behaviour such as photo- or electroluminescence, is not quenched by parallel non-radiative surface pathways.

These issues have been explored by Danek and co-workers[39-41] who synthesized quantum dot:host composites consisting of CdSe quantum dots in a ZnSe matrix. Overcoated quantum dots were synthesized by growing a thin layer of ZnSe around size-selected CdSe nanocrystallites synthesized by the method of Murray et al.[14] The overcoated CdSe quantum dots were then dispersed into an aerosol using an electrospray apparatus and collected on a heated substrate while a ZnSe film was simultaneously grown by organometallic chemical vapor deposition (OMCVD). These composite films

exhibit optical absorption and photoluminescence spectra similar to those of the CdSe nanocrystallites in solution. However, CdSe:ZnSe composites synthesized from quantum dots without a pre-deposited ZnSe overlayer have substantially lower PL yields than composites synthesized using overcoated CdSe quantum dots. This indicates that the pre-deposited ZnSe overcoat performs a passivating role that enhances luminescence from the CdSe quantum dots.

In the CdSe:ZnSe system, then, the size of the quantum dots is precisely controlled by the size-selective solution-phase synthesis technique, and surface passivation is controlled by pre-depositing a passivating layer of ZnSe on the CdSe quantum dots prior to their incorporation into the OMCVD-deposited ZnSe matrix.

Present-day microelectronics technology is dominated by silicon, however, so it would be ideal to have a silicon-based quantum dot material so that the wealth of knowledge and investment in silicon processing could be utilized. We propose to use the PLA-SSE method to synthesize a variety of elemental quantum dots and codeposit them into Si matrices, and to synthesize Si quantum dots for codeposition into $SiO_2$ matrices.

The PLA-SSE source is a vacuum-based system and produces bare clusters *in vacuo* without any capping groups on the cluster surface. This eliminates the requirement that the host matrix deposition technique be compatible with the capping group and gives us maximum flexibility to use any vacuum-compatible deposition technique for growing the host matrix, and for investigating questions of cluster surface passivation.

Among the issues that are raised in this work are the sharpness of the interface between nanocluster and host, the likelihood of achieving three-dimensional epitaxy, the passivation of the interface and the effect of the nanoclusters on the matrix film growth.

Given the very small length scales involved, will the quantum dots retain their identity after codeposition into the host, or will they interdiffuse with the host matrix? For codeposition of Ge clusters into a Si host matrix, the two materials are lattice mismatched, but in the case of planar heteroepitaxy, say in the growth of quantum wells, lattice coherency is retained for layers thinner than the critical thickness. Is there a corresponding critical radius for Si layers grown around Ge nanocrystals? How thick a Si shell could be grown around a Ge nanocrystal before dislocations occur? Passivation of the

quantum dot surface has been shown to be necessary for quantum confinement effects to be manifested. Will it be possible to eliminate surface defects and dangling bonds on PLA-SSE nanoclusters as they are deposited into the Si and $SiO_2$ host matrices? Nanometer-scale seed crystals have been shown to enhance the growth rate of polycrystalline Si[42]. Would the PLA-SSE nanoclusters have a similar effect on the deposition of the Si and $SiO_2$ host matrices ?

Another interesting issue is the effect of the nanocluster size distribution on the properties of cluster:host composites. Size-selection is being investigated by other workers in the Kolenbrander research group,[43] but is not directly addressed in this thesis. The primary focus of this thesis is on methods of matrix codeposition and surface passivation of the PLA-SSE quantum dots.

In Chapter 2, I describe the PLA-SSE nanocluster source and review previous characterization of Si and Ge quantum dots synthesized by the PLA-SSE technique. Chapter 3 provides a review of techniques used for depositing Si and $SiO_2$, and in Chapters 4 and 5, I describe the combination of PLA-SSE with various host matrix deposition techniques for synthesizing quantum dot:host composites. Chapter 4 focuses on composites based on Ge quantum dots while Chapter 5 focuses on materials based on Si quantum dots. Chapter 6 deals with Er-based composites, and Chapters 7 and 8 summarize the work performed for this thesis and its key conclusions.

## REFERENCES


1. B. E. Deal and J. M. Early, "The evolution of silicon semiconductor technology: 1952-1977," J. Electrochem. Soc. **126** (1), 20C (1979).
2. E. Abraham, C. T. Seaton, and S. D. Smith, "The optical computer," Sci. Am. **248** (February), 85 (1983).
3. A. Y. Cho, "Twenty years of molecular beam epitaxy," J. Cryst. Growth **150** (1), 1 (1995).
4. D. S. Chemla, "Nonlinear optics in quantum confined structures," Phys. Today **46** (June), 46 (1993).
5. H. S. Hinton, "Switching to photonics," IEEE Spectr. **29** (February), 42 (1992).
6. K. Werner, "Higher visibility for LEDs," IEEE Spectr. **31** (July), 30 (1994).
7. E. Corcoran, "Diminishing Dimensions," Sci. Am. **263** (November), 122 (1990).
8. M. A. Reed, "Quantum Dots," Sci. Am. **268** (January), 118 (1993).
9. P. Horan and W. Blau, "Linear and nonlinear optical properties of semiconductor particles," Phase Transit. **24-26**, 605 (1990).
10. A. D. Yoffe, "Low-dimensional systems: quantum size effects and electronic properties of semiconductor microcrystallites (zero-dimensional systems) and some quasi-two-dimensional systems," Adv. Phys. **42** (2), 173 (1993).

11. B. K. Rao, S. N. Khanna, and P. Jena, "Clusters-A new phase of matter," Phase Transit. **24-26**, 35 (1990).
12. M. L. Steigerwald and L. E. Brus, "Synthesis, stabilization, and electronic structure of quantum semiconductor nanoclusters," Annu. Rev. Mater. Sci. **19**, 471 (1989).
13. M. G. Bawendi, M. L. Steigerwald, and L. E. Brus, "The quantum mechanics of larger semiconductor clusters (quantum dots)," Annu. Rev. Phys. Chem. **41**, 477 (1990).
14. C. B. Murray, D. J. Norris, and M. G. Bawendi, "Synthesis and Characterization of Nearly Monodisperse CdE (E = S, Se, Te) Semiconductor Nanocrystallites," J. Am. Chem. Soc. **115**, 8706 (1993).
15. D. J. Norris, M. Nirmal, C. B. Murray, A. Sacra, and M. G. Bawendi, "Size Dependent Optical Spectroscopy of II-VI Semiconductor Nanocrystallites (Quantum Dots)," Z. Phys. D **26** (1-4), 355 (1993).
16. B. O. Dabboussi, M. G. Bawendi, O. Onitsuka, and M. F. Rubner, "Electroluminescence from CdSe quantum dot/polymer composites," Appl. Phys. Lett. **66** (11), 1316 (1995).
17. M. A. Omar, *Elementary solid state physics* (Addison-Wesley, Reading, MA, 1975).
18. L. E. Brus, P. F. Szajowski, W. L. Wilson, T. D. Harris, S. Schuppler, and P. H. Citron, "Electronic spectroscopy and photophysics of Si nanocrystals: Relationships to bulk c-Si and porous Si," J. Am. Chem. Soc. **117**, 2915 (1995).
19. S. S. Iyer and Y. H. Xie, "Light emission from silicon," Science **260**, 40 (1993).
20. M. S. Hybertson, "Absorption and emission of light in nanoscale silicon structures," Phys. Rev. Lett. **72** (10), 1514 (1994).
21. T. Takagahara and K. Takeda, "Theory of the quantum confinement effect on excitons in quantum dots of indirect-gap materials," Phys. Rev. B **46** (23), 15578 (1992).
22. L. T. Canham, "Silicon quantum wire array fabrication by electrochemical and chemical dissolution of wafers," Appl. Phys. Lett. **57** (10), 1046 (1990).
23. K. A. Littau, P. J. Szajowski, A. J. Muller, A. R. Kortan, and L. E. Brus, "A luminescent silicon nanocrystal colloid via a high-temperature aerosol reaction," J. Phys. Chem. **97**, 1224 (1993).
24. W. L. Wilson, P. F. Szajowksi, and L. E. Brus, "Quantum confinement in size-selected surface-oxidized silicon nanocrystals," Science **262**, 1242 (1993).
25. S. Hayashi, S. Tanimoto, and K. Yamamoto, "Analysis of surface oxides of gas-evaporated Si small particles with infrared spectroscopy, high-resolution electron microscopy, and x-ray photoemission spectroscopy," J. Appl. Phys. **68** (10), 5300 (1990).
26. K. Kohno, Y. Osaka, F. Toyomura, and H. Katayama, "Photoluminescence of Si microscrystals embedded in $SiO_2$ glass films," Jpn. J. Appl. Phys. **33 (Part 1)** (12A), 6616 (1994).
27. L. A. Chiu, A. A. Seraphin, and K. D. Kolenbrander, "Gas phase synthesis and processing of silicon nanocrystallites: Characterization by photoluminescence emission spectroscopy," J. Electron. Mater. **23** (3), 347 (1994).
28. E. Werwa, A. A. Seraphin, L. A. Chiu, C. Zhou, and K. D. Kolenbrander, "Synthesis and processing of silicon nanocrystallites using a pulsed laser ablation supersonic expansion method," Appl. Phys. Lett. **64** (14), 1821 (1994).
29. A. G. Cullis and L. T. Canham, "Visible light emission due to quantum size effects in highly porous crystalline silicon," Nature **353**, 335 (1991).
30. Y. Kanemitsu, "Luminescence properties of nanometer-sized Si crystallites: Core and surface states," Phys. Rev. B **49** (23), 16845 (1994).
31. A. A. Seraphin, E. Werwa, L. A. Chiu, and K. D. Kolebrander, "The enabling role of surface passivation in visible photoluminescence from Si nanoparticles," in *Interface control of electrical, chemical and mechanical properties*, edited by S. P. Murarka, K. Rose, T. Ohmi, and T. Seidel (Materials Research Society, Pittsburgh, PA, 1994), p. 433.
32. A. A. Seraphin, S.-T. Ngiam, and K. D. Kolenbrander, "Control of silicon nanocrystallite luminescence behavior through surface treatments," in *Materials Research Society symposia proceedings*, edited by R. C. Cammarata (Materials Research Society, Pittsburgh, PA, (in press)), Vol. 405.

33. Y. Maeda, N. Tsukamoto, Y. Yazawa, Y. Kanemitsu, and Y. Masumoto, "Visible photoluminescence of Ge microcrystals embedded in $SiO_2$ glassy matrices," **59**, 3168 (1991).
34. Y. Kanemitsu, H. Uto, Y. Masumoto, and Y. Maeda, "On the origin of visible photoluminescence in nanometer-size Ge crystallites," Appl. Phys. Lett. **61**, 2187 (1992).
35. Y. Maeda, "Visible photoluminescence fron nanocrystallite Ge embedded in a glassy $SiO_2$ matrix: Evidence in support of the quantum-confinement mechanism," Phys. Rev. B **51** (3), 1658 (1995).
36. K. V. Shcheglov, C. M. Yang, K. J. Vahala, and H. A. Atwater, "Electroluminescence and photoluminescence of Ge-implanted $Si/SiO_2/Si$ structures," Appl. Phys. Lett. **66** (6), 745 (1995).
37. J. R. Heath and F. K. LeGoues, "A liquid solution synthesis of single crystal germanium quantum wires," Chem. Phys. Lett. **208** (3,4), 263 (1993).
38. J. R. Heath, J. J. Shiang, and A. P. Alivisatos, "Germanium quantum dots: optical properties and synthesis," J. Chem. Phys. **101** (2), 1607 (1994).
39. M. Danek, K. F. Jensen, C. B. Murray, and M. G. Bawendi, "Preparation of II-VI quantum dot composites by electrospray organometallic chemical vapor deposition," J. Cryst. Growth (1994).
40. M. Danek, K. F. Jensen, C. B. Murray, and M. G. Bawendi, "Electrospray organometallic chemical vapor deposition - A novel technique for preparation of II-VI quantum dot composites," Appl. Phys. Lett. **65** (22), 2795 (1994).
41. M. Danek, "Chemical approaches to organometallic chemical vapor deposition of wide band-gap II-VI layers and nanocrystal composites," PhD. thesis, Massachusetts Institute of Technology, 1995.
42. J. R. Heath, S. M. Gates, and C. A. Chess, "Nanocrystal seeding: A low temperature route to polycrystalline Si films," Appl. Phys. Lett. **64** (26), 3569 (1994).
43. E. Werwa and K. D. Kolenbrander, "Synthesis of thin films of size-selected silicon nanocrystallites using pulsed laser ablation supersonic expansion," presented at the Materials Research Society Fall Meeting, Boston, MA, 1995 (unpublished).

# Chapter 2
# Pulsed Laser Ablation-Supersonic Expansion

Nanoclusters produced by Pulsed Laser Ablation-Supersonic Expansion (PLA-SSE) are at the core of this research work. This chapter describes the PLA-SSE process, and Si and Ge nanoclusters produced in the system.† The cluster production rate is on the order of $10^2$ ng/cm$^2$ hr, and a wide range of cluster sizes is produced, ranging from particles with a diameter of hundreds of nanometers to diatomic clusters. PLA-SSE is shown to produce nanometer-scale Si and Ge crystals. Whereas bulk Si is a poor light emitter, visible orange-red photoluminescence is observed from PLA-SSE Si nanoclusters. This is above the band-gap of bulk Si and the blue-shift is believed to be due to quantum confinement effects in Si nanocrystallites.

## 2.1 PLA-SSE cluster source

Nanoclusters are generated in the gas phase using a Pulsed Laser Ablation-Supersonic Expansion (PLA-SSE) system.[1] This system is a descendant of cluster sources developed by Richard Smalley and co-workers at Rice University[2,3] and also used by Mandich and co-workers at A. T. & T. Bell Laboratories.[4,5] Cluster sources of this design first appeared in the early 1980s and were initially used to study the structure and reactivity of clusters of < 100 atoms. Fullerenes, e.g., $C_{60}$, were discovered by Smalley's group in 1985 using a PLA-SSE apparatus.[6] Briefly, a pulsed laser beam is used to rapidly heat a solid target and generate a vapor which is rapidly cooled by a synchronized gust of helium flowing over the target. The vapor condenses into multi-atom clusters which are carried into a vacuum chamber by the He gas which experiences rapid adiabatic cooling as it expands into the vaccum. The condensed clusters are rapidly cooled as well and the condensation process arrested, preventing further growth of the clusters.

Our PLA-SSE cluster source is shown schematically in Figure 2.1 The $^1/_4$ inch diameter target rod is rotated by mechanical connection to a motor-driven screw and is located along the side of a 1 mm diameter channel drilled

---

† Characterization of PLA-SSE Si nanoclusters was primarily performed by Chuxin Zhou, Leon Chiu, Arun Seraphin and Eric Werwa of the Kolenbrander research group.

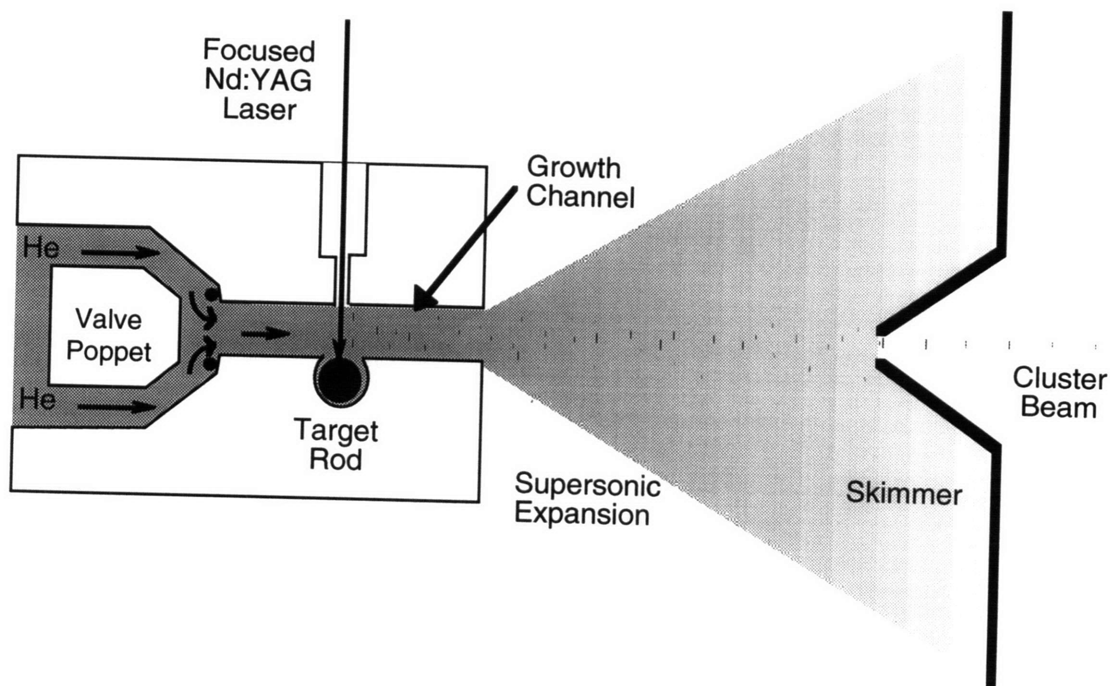


Figure 2.1 Schematic diagram of the Pulsed Laser Ablation-Supersonic Expansion cluster source. A pulse of He flows through the growth channel as the rotating target rod is irradiated with a 532 nm laser pulse. Evaporated material is cooled by the flowing He and condenses into a broad range of cluster sizes. The condensation reaction is then rapidly quenched by the supersonic expansion of He into the primary chamber which is at an operating pressure of $10^{-4}$ torr.

through a $^1/_4$ inch thick stainless steel block. The target rod is ablated with a Continuum NY60 Neodynium-doped Yttrium Aluminum Garnet (Nd:YAG) pulsed laser focused onto the surface of the target rod and delivering 3-10 mJ/pulse at 20 Hz onto an approximately 0.7 mm diamter spot, corresponding to a power density of 15–50 W/cm$^2$. Helium gas is pulsed into the growth channel from a 550 psi reservoir, through a General Valves Corporation Series 9 high-speed solenoid valve with a nominal pulse width of 100 μs.

Laser-ablated material from the target is cooled by the He pulse and starts to condense in the growth channel.[2] The cluster condensation reactions are then rapidly quenched as the He undergoes a supersonic free jet expansion

into the $10^{-4}$ torr vacuum of the primary chamber. A broad distribution of cluster sizes is produced, ranging from diatomic clusters to large clusters hundreds of nanometers in diameter. This cluster size distribution may be controlled by varying the operating conditions of the PLA cluster source. For example, increasing the length of the growth channel, or increasing the delay between the helium and laser pulses, increases the average size of the clusters.[1] Hopkins et al. have also found that the clustering process is influenced by the gas pressure behind the nozzle and the laser fluence.[2] The exact mechanism of nanocluster growth in PLA-SSE is still unclear, however, and it is likely that a variety of processes, including homogeneous and heterogeneous nucleation, condensation, coagulation and agglomeration [7-10]) are at work. Some clusters may also be formed directly by the ejection of solid fragments or liquid droplets from the target rod as a result of laser ablation.

**2.1.1 Modelling of the PLA-SSE cluster source**

The He pressure behind the nozzle is ~ 30,000 torr (550 psi) while the background pressure in the vacuum chambers is $10^{-4}$ – $10^{-6}$ torr. The Knudsen number (i.e., the ratio of mean free path to characteristic length scale) in our system ranges from $<< 10^{-2}$ in the growth channel to ~ $10^{3}$ in the vacuum chamber. The entire range of flow regimes from continuum to transition to collisionless flow is therefore encountered in the PLA-SSE process.

In the continuum regime ($Kn < 0.1$), the gas behaves as a viscous fluid and can be modelled using the Navier-Stokes equations. At the other extreme, in the collisionless or free molecular limit ($Kn \to \infty$), intermolecular collisions become very rare and flow is dominated by gas-surface interactions. Gas flow in this regime is typically modelled using test particle Monte Carlo techniques.[11,12] Between these two limits, in the transition regime, the Direct Simulation Monte Carlo (DSMC) technique is used to model gas flow.[13]

Individual components of the PLA-SSE process have previously been modelled by other workers in the field. For example, Singh et al.[14] have modelled laser ablation and plasma plume formation using continuum models. Steady-state free jet expansions and supersonic beam skimmers have been extensively studied by Bird[15] and Boyd[16] using the DSMC method. The laser ablation and He pulse with cluster condensation within a confined

growth channel also bear some similarity to shock tube techniques used in chemical kinetic studies.[17]

Simulation of the PLA-SSE process is complicated by the transient nature of the process, the unknown composition and reactivity of neutral and ionized species ejected from the target during laser ablation, and the range of flow regimes involved. In addition, Hopkins et al.[2] have found that the mechanical response of the high speed valve also influences cluster formation, so the valve behavior would also have to be incorporated into a detailed model of the PLA-SSE process.

A greater understanding of the cluster size and velocity distribution would contribute to current efforts to size-select clusters based on velocity slip between larger and smaller clusters, and to optimize the PLA-SSE cluster source. Unfortunately, the knowledge that could be gained from the simulation would be limited by the large number of assumptions and simplifications required to make the simulation problem tractable. It was therefore felt that the cost of developing a detailed simulation of the PLA-SSE process could not be justified by the returns.

## 2.2 Size selection

A wide range of particle sizes is produced by the PLA-SSE cluster source, ranging from monatomic and polyatomic species to nanometer-scale clusters and micron-scale particles. A limited degree of control is obtained by varying the length of the growth channel and the timing of the helium and laser pulses, as evidenced by changes in the size-dependent PL spectra of Si clusters as these parameters are varied.[18] A very wide size distribution is still produced, however, as seen by TEM analysis and by the width of the PL peak. Ideally, we would like to be able to control the average size as well as the range of sizes of the clusters.

One approach to this problem is to take advantage of the phenomenon of velocity slip, which results in lighter clusters having a higher velocity than heavier clusters.[19,20] A cluster packet is produced by each laser pulse, within which the lighter clusters have a higher velocity than the the heavier clusters. A velocity filter such as a mechanical chopper wheel which separates the clusters on the basis of velocity will therefore also yield a size separation. Early results in this avenue show that it is possible to shift the peak PL

wavelength of Si clusters from 670 nm to 550 nm using a rotating chopper wheel, and that the FWHM of the PL peak is halved by size-separating the Si clusters.[20]

## 2.3 Deposition rate

The deposition rate was measured with a quartz crystal monitor placed 24 cm away from the nozzle along the center-line of the apparatus. The deposition rate for Si nanocrystals was approximately 250 ng/cm$^2$ hr while that for Ge nanocrystals was approximately 150 ng/cm$^2$ hr with a laser power of 5 mJ/pulse. The heat of vaporization of Ge is one-third that of Si on a mass basis, and the boiling point of Ge is also lower than that of Si, so the cluster production rate cannot be inversely proportional to heat of vaporization and boiling point, otherwise the Ge cluster production rate would be expected to be larger than that for Si. Other factors such as the absorptivity and thermal conductivity of the target may thus be controlling the cluster production rate. The relative timing of the laser and helium pulses may also affect the cluster production rate. The same timing was used for Si and Ge, however, and this may have been sub-optimal for Ge, resulting in a lower production rate compared to Si.

Assuming that the angular distribution of clusters leaving the PLA-SSE source is described by a cosine law, the deposition rate 6.3 cm above the center-line (horizontal separation remaining at 24 cm) is predicted to be 87% of the center-line value.[21] For a spherical distribution, the deposition rate would be expected to be 92% of the center-line value. The measured deposition rate, however, is 200 ng/cm$^2$ hr, or only 80% of the center-line value. The angular distribution of clusters is thus even more strongly forward peaked than a cosine distribution and falls off rapidly with displacement from the center-line.

## 2.4 Si nanocluster characterization

Si nanoclusters were collected directly on TEM grids coated with amorphous carbon and formvar, and examined with a high resolution TEM.[22] Figure 2.2 shows a crystalline Si particle approximately 3 nm in diameter. The lattice fringes have a spacing of 1.6 Å, corresponding to the (311) lattice spacing of diamond cubic Si (JCPDS Card 27-1402).[23] A wide

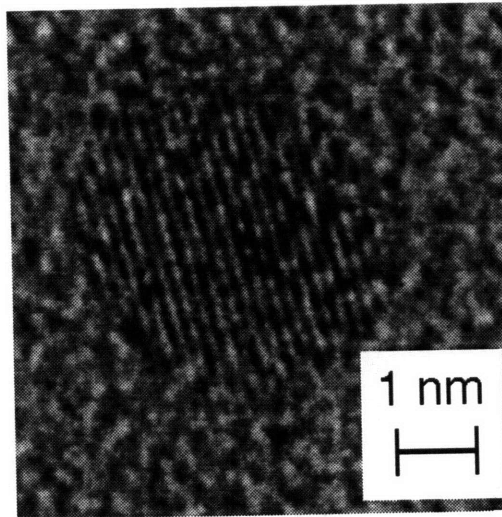


Figure 2.2 High Resolution Transmission Electron Microscope image of PLA-SSE Si nanocrystal collected on C-formvar coated TEM grid (from Werwa et al, 1994).

distribution of particle sizes, with diameters ranging from 2 nm to several hundred nanometers, was also observed.

**2.4.1 Photoluminescence**

PLA-SSE nanoclusters exhibit visible orange photoluminescence under ultraviolet excitation (Figure 2.3). Curve (a) shows that no PL is observed from clusters immediately after deposition, while curve (b) shows the PL spectrum following a 60 s dip in 48 % hydrofluoric acid. The PL spectrum is similar to that observed from electrochemically-etched porous silicon and nanocrystalline silicon synthesized by an aerosol process.[24,25] PLA-SSE Si nanoclusters do not exhibit PL in the gas phase prior to deposition, nor do they exhibit PL when deposited on a solid substrate and allowed to age *in vacuo*. PL is only observed when the Si nanoclusters are aged in air or dipped in HF or $HNO_3$.[26]

An oxide layer is formed on the surface of the Si nanoclusters following atmospheric oxidation or oxidation in $HNO_3$, while a hydride adlayer is formed by dipping in HF. These oxide and hydride layers passivate the Si nanoclusters and allow PL to be observed. In the absence of these treatments, a high density of states is present on the surface of the clusters which

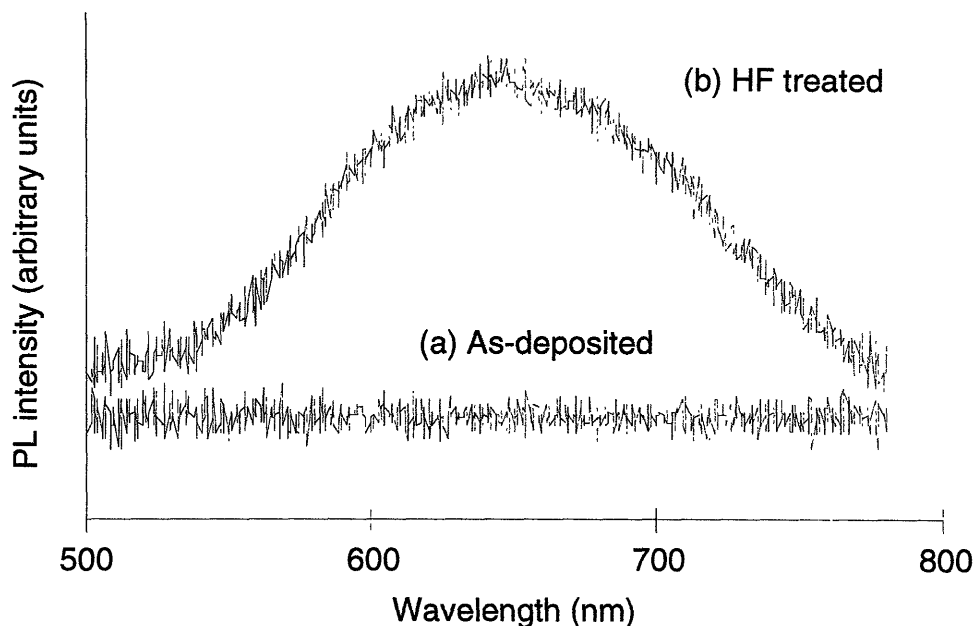


Figure 2.3 Photoluminescence spectrum of Si nanoclusters deposited on teflon substrate, (a) as-deposited and (b) after dipping in HF.

quenches photoluminescence by providing alternative non-radiative pathways for exciton recombination.

The peak wavelength of the PL can be varied by adjusting the operating conditions of the source to generate larger or smaller clusters.[1] The peak wavelength is also blue-shifted by successive etches in HF or $HNO_3$ due to the reduction in particle size with each etch cycle. This size-dependence of the PL peak wavelength is similar to that observed by Wilson et al.[27] for aerosol-synthesized Si nanocrystals and indicates that the photoluminescence is due to quantum confinement effects.

Quantum confinement alone is not sufficient to activate photoluminescence from Si nanocrystals, however. Radiative recombination competes with non-radiative recombination and the non-radiative pathways must be suppressed for luminescence to be observed. For example, defects or dangling bonds at the surface of the nanocrystallite create states within the band gap that trap carriers and prevent radiative recombination.[28] Surface passivation by oxide or hydride species that tie up dangling bonds is therefore necessary to enable photoluminescence from the Si nanoclusters. Both quantum

confinement and surface passivation must therefore be present for luminescence to be observed from nanocrystalline Si.[29]

## 2.5 Ge nanocluster characterization

Ge nanoclusters were collected in the secondary chamber on a C-coated TEM grid heated to 400°C. The TEM grid was heated so that the Ge nanoclusters collected under these conditions could be compared to the Ge cluster:Si host composites described in Section 4, which are grown on a heated substrate. Particles from 5 to 500 nm in diameter were observed with a 200 kV Akashi EM 002B High Resolution Transmission Electron Microscope (HREM), but we did not further characterize the size distribution. Diffraction planes are visible in the 10 nm diameter particle shown in Figure 2.4, indicating that some of the particles are crystalline. The lattice planes had a spacing of 1.9 Å, which is reasonably close to the standard value of 2.0 Å for Ge (220) planes (JCPS card 4-0545).[23]

The X-ray diffraction spectrum of Ge clusters collected on a Si wafer are shown in curve (a) of Figure 2.5 The spectrum was collected on a Rigaku RU 300 diffractometer using Cu Kα radiation. Three peaks are seen at $2\theta = 27.3°$, 45.3° and 53.7°, corresponding to the 111, 220 and 311 reflections of Ge (JCPDS card 4-545). In addition, Bragg diffraction from Si (800) planes in the Si (100) substrate give rise to the strong peak around 33.0°.

The calculated effects of finite particle size on the XRD line width are shown in curves (b) – (d), which show simulated XRD spectra for bulk Ge, 10 nm and 5 nm diameter Ge particles, respectively (The theory of X-ray diffraction is discussed further in Section 5.4.2) The widths of the Ge diffraction peaks are essentially the same as that for bulk Ge, indicating that some of the Ge particles present are larger than 100 nm in diameter. The HREM images and XRD data therefore show that a very wide particle size distribution is obtained by PLA-SSE, ranging from smaller than 10 nm to several hundred nanometers in diameter.

### 2.5.1 Photoluminescence

Visible PL spectra were collected by excitation with a tripled Nd:YAG laser (355 nm) using a 0.25 m monochromator and a Si detector. Near infra-red PL spectra were collected by excitation with an $Ar^+$ laser (488 nm) using a 0.75 m

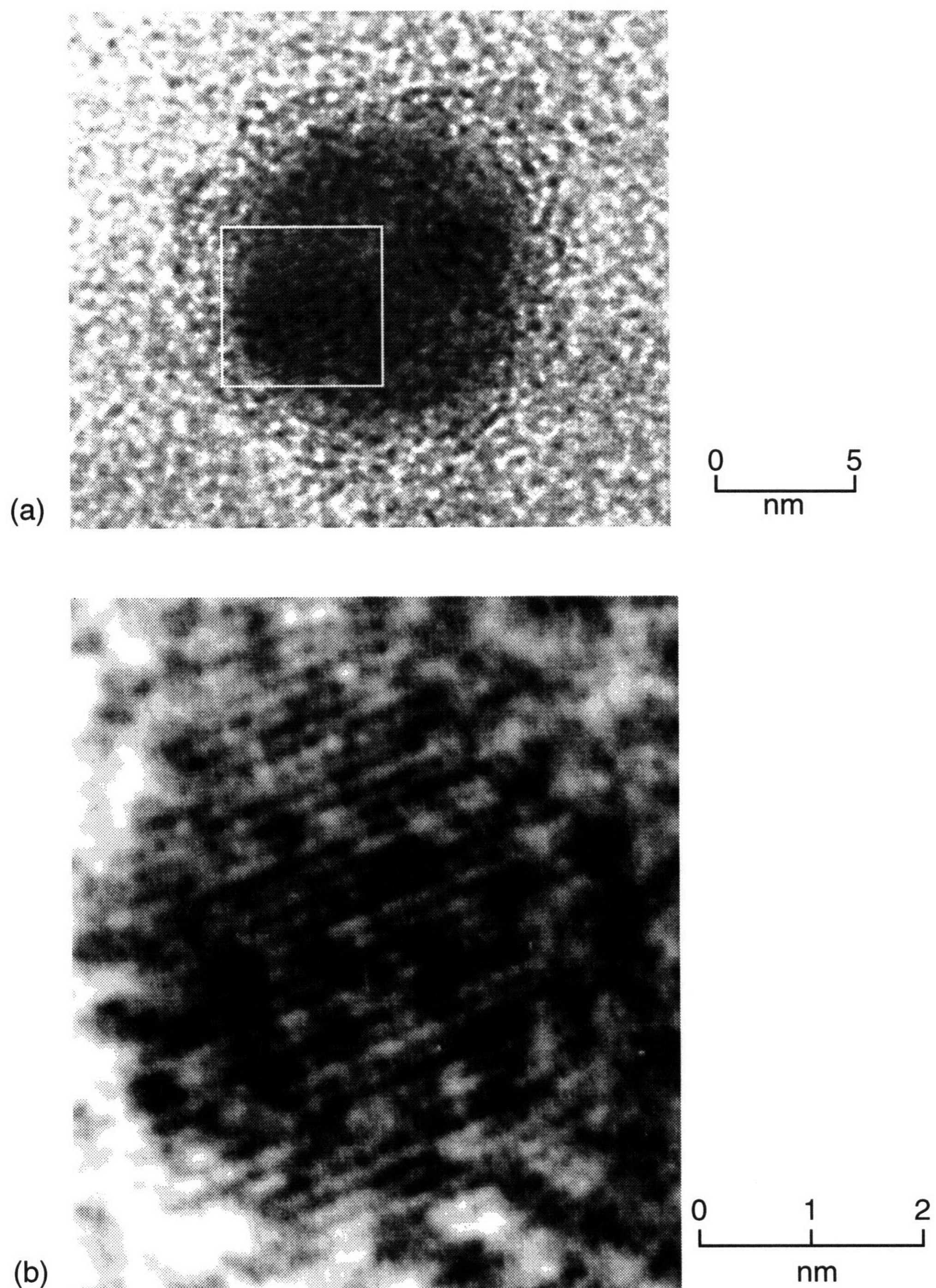


Figure 2.4 Micrographs of Ge nanoparticle collected on C-coated TEM grid at 400°C. Lattice planes are visible in the highlighted area of part (a) and are shown at higher magnification in part (b). The lattice spacing of 1.9 Å is close to the reference value of 2.0Å for Ge (220) planes (JCPDS Card 4-0545).

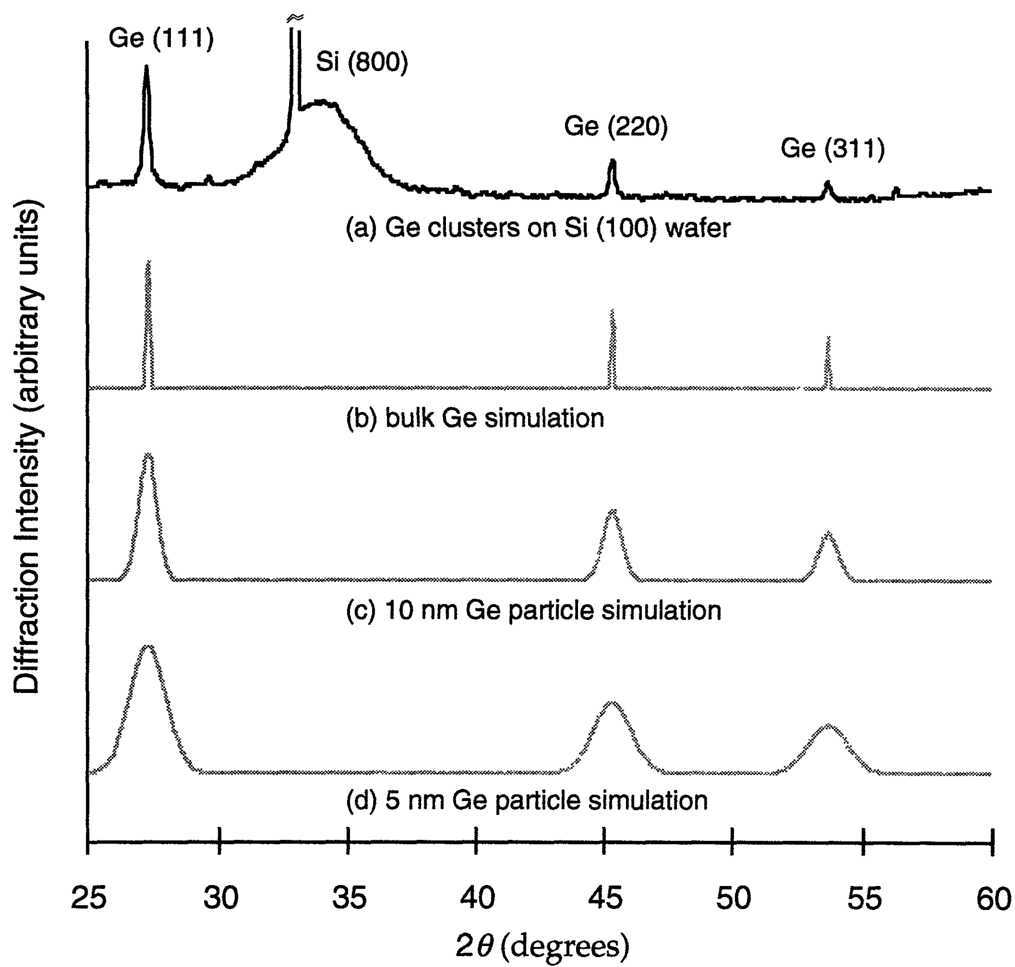


Figure 2.5 (a) XRD spectrum of PLA-SSE Ge clusters deposited on a Si (100) wafer. Peaks are seen at $2\theta$= 27.3°, 45.3° and 53.7° in curve corresponding to Ge (JCPDS card 4-545). The feature around $2\theta$ = 33.0° is the 800 Si reflection from the single crystal Si wafer substrate. Curves (b)–(d) are simulated spectra for bulk Ge, 10 nm and 5 nm diameter Ge particles respectively, illustrating the broadening of XRD lines as particle size decreases.

monochromator and a Ge detector. No visible or infra-red PL was detected from the Ge clusters, however, despite theoretical predictions that quantum confinement effects in Ge are even stronger than in Si.[30] Unlike Si, however, Ge is not passivated by its oxide[31], so PL might not be observed in PLA-SSE Ge nanoclusters because of the high density of states at the interface. Non-radiative recombination at the surface is then favored and luminescence is quenched.

Heath[32-34] has reported evidence of size-dependence in the extinction spectra of colloids of Ge nanocrystals in acetonitrile, but has not reported any photoluminescence behaviour. There have been several reports of visible PL from Ge-implanted $SiO_2$[35,36] and $H_2$-reduced Si-Ge oxides[37] where the photoluminescence is attributed to quantum-confined nanocrystalline Ge. The reported PL spectra are remarkably similar to that of silica glass, however, so the PL may in fact be due to $SiO_2$.

On a historical note, Ge was in fact the earliest semiconductor transistor material and was only replaced by Si in the 1960s due to the rise of planar processing technologies which gave Si the advantage because Si has a robust, easily grown oxide that ties up dangling bonds on the surface and provides excellent surface passivation. The interface trap density on Ge is several orders of magnitude larger than for Si-$SiO_2$ systems[31], and Ge oxides are water-soluble. This makes the Ge-$GeO_2$ sytem unsuitable for aqueous etching steps and further degrades the interface quality in humid atmospheres.

The factors that made Si the premier material for microelectronic applications also apply in the field of nanoscale quantum dots. Si nanocrystals synthesized by a variety of techniques are physically protected and chemically and electronically passivated by an $SiO_2$ layer grown by thermal oxidation or by spontaneous oxidation in air. Ge nanocrystals, in contrast, are not passivated by their oxide and even if their energy levels were modified by quantum confinement, this is not manifested as photoluminescence because of non-radiative recombination at the Ge cluster surface.

## REFERENCES

1. L. A. Chiu, A. A. Seraphin, and K. D. Kolenbrander, "Gas phase synthesis and processing of silicon nanocrystallites: Characterization by photoluminescence emission spectroscopy," J. Electron. Mater. **23** (3), 347 (1994).

2. J. B. Hopkins, P. R. R. Langridge-Smith, M. D. Morse, and R. E. Smalley, "Supersonic metal cluster beams of refractory metals: Spectral investigations of ultracold $Mo_2$," J. Chem. Phys. **78** (4), 1627 (1983).
3. M. A. Duncan and D. H. Rouvray, "Microclusters," Sci. Am. **265** (December), 110 (1989).
4. K. D. Kolenbrander and M. L. Mandich, "Optical and near-infrared spectroscopy of neutral indium phosphide clusters," J. Chem. Phys. **92** (8), 4759 (1990).
5. K.-D. Rinnen and M. L. Mandich, "Spectroscopy of neutral silicon clusters, $Si_{18}$–$Si_{41}$: Spectra are remarkably size independent," Phys. Rev. Lett. **69** (12), 1823 (1992).
6. R. F. Curl and R. E. Smalley, "Fullerenes," Sci. Am. **265** (October), 54 (1991).
7. M. Kappes and S. Leutwyler, "Molecular beams of clusters," in *Atomic and molecular beam methods*, edited by G. Scoles (Oxford University Press, New York, 1988), Vol. 1, p. 380.
8. W. Knauer, "Formation of large metal clusters by surface nucleation," J. Appl. Phys. **62** (3), 841 (1987).
9. S. K. Friedlander, *Smoke, dust and haze* (John Wiley & Sons, Inc., New York, 1977).
10. N. A. Fuchs, *The mechanics of aerosols* (The MacMillan Company, New York, 1964).
11. D. H. Davis, "Monte Carlo calculation of molecular flow rates through a cylindrical elbow and pipes of other shapes," J. Appl. Phys. **31** (7), 1169 (1960).
12. J. F. O'Hanlon, *A User's Guide to Vacuum Technology* (John Wiley & Sons, New York, 1989).
13. G. A. Bird, "Monte Carlo simulation of gas flows," Annu. Rev. Fluid Mech. **10**, 11 (1978).
14. R. K. Singh, O. W. Holland, and J. Narayan, "Theoretical model for deposition of superconducting thin films using pulsed laser evaporation technique," J. Appl. Phys. **68** (1) (1990).
15. G. A. Bird, *Molecular Gas Dynamics* (Clarendon, Oxford, UK, 1976).
16. I. D. Boyd, "Vectorization of a Monte Carlo simulation scheme for nonequilibrium gas dynamics," J. Comput. Phys. **96**, 411 (1991).
17. J. V. Michael and K. P. Lim, "Shock tube techniques in chemical kinetics," Annu. Rev. Phys. Chem. **44**, 429 (1993).
18. L. A. Chiu, "Gas phase synthesis of silicon nanoclusters: Mass characterization by photoluminescence," S. M. thesis, Massachusetts Institute of Technology, 1993.
19. M. Broyer, B. Cabaud, A. Hoareau, P. Melinon, D. Rayane, and B. Tribollet, "Velocity slip measurements of bismuth clusters produced by the inert gas condensation technique," Mol. Phys. **62** (3), 559 (1987).
20. E. Werwa and K. D. Kolenbrander, "Synthesis of thin films of size-selected silicon nanocrystallites using pulsed laser ablation supersonic expansion," in *Materials Research Society Symposia Proceedings*, edited by R. Singh, J. Narayan, D. Norton, J. Cheung, and L. D. Laude (Materials Research Society, Pittsburgh, PA, 1996).
21. S. M. Sze, *VLSI Technology* (McGraw-Hill, New York, 1988).
22. E. Werwa, A. A. Seraphin, L. A. Chiu, C. Zhou, and K. D. Kolenbrander, "Synthesis and processing of silicon nanocrystallites using a pulsed laser ablation supersonic expansion method," Appl. Phys. Lett. **64** (14), 1821 (1994).
23. Joint Committee on Powder Diffraction Standards, *Powder diffraction file* (JCPDS International Centre for Diffraction Data, Swarthmore, Pa., ).
24. L. E. Brus, P. F. Szajowski, W. L. Wilson, T. D. Harris, S. Schuppler, and P. H. Citron, "Electronic spectroscopy and photophysics of Si nanocrystals: Relationships to bulk c-Si and porous Si," J. Am. Chem. Soc. **117**, 2915 (1995).
25. L. Brus, "Luminescence of Silicon Materials: Chains, Sheets, Nanocrystals, Nanowires, Microcrystals, and Porous Silicon," J. Phys. Chem. **98** (14), 3575 (1994).
26. A. A. Seraphin, S.-T. Ngiam, and K. D. Kolenbrander, "Control of silicon nanocrystallite luminescence behavior through surface treatments," in *Materials Research Society symposia proceedings*, edited by R. C. Cammarata (Materials Research Society, Pittsburgh, PA, (in press)), Vol. 405.

27. W. L. Wilson, P. F. Szajowksi, and L. E. Brus, "Quantum confinement in size-selected surface-oxidized silicon nanocrystals," Science **262**, 1242 (1993).
28. A. Seraphin, "Photoluminescence properties of Si nanocrystallites," PhD. thesis, Massachusetts Institute of Technology, 1996.
29. A. A. Seraphin, E. Werwa, L. A. Chiu, and K. D. Kolebrander, "The enabling role of surface passivation in visible photoluminescence from Si nanoparticles," in *Interface control of electrical, chemical and mechanical properties*, edited by S. P. Murarka, K. Rose, T. Ohmi, and T. Seidel (Materials Research Society, Pittsburgh, PA, 1994), p. 433.
30. T. Takagahara and K. Takeda, "Theory of the quantum confinement effect on excitons in quantum dots of indirect-gap materials," Phys. Rev. B **46** (23), 15578 (1992).
31. P. Balk, "Introduction," in *The $Si$-$SiO_2$ system*, edited by P. Balk (Elsevier, Amsterdam, 1988), p. 3.
32. J. R. Heath, "A liquid-solution-phase synthesis of crystalline silicon," Science **258**, 1131 (1992).
33. J. R. Heath and F. K. LeGoues, "A liquid solution synthesis of single crystal germanium quantum wires," Chem. Phys. Lett. **208** (3,4), 263 (1993).
34. J. R. Heath and P. F. Seidler, "Separation of nucleation and crystallization in the solution-phase synthesis of group IV quantum structures," in *Materials Research Society Symposium* (Materials Research Society, 1993), Vol. 298, pp. 91.
35. Y. Kanemitsu, T. Ogawa, K. Shirasishi, and K. Takeda, "Exciton confinement on a spherical shell: visible photoluminescence from oxidized Si and Ge nanoballs," J. Lumin. **60-61**, 337 (1994).
36. K. V. Shcheglov, C. M. Yang, K. J. Vahala, and H. A. Atwater, "Electroluminescence and photoluminescence of Ge-implanted $Si/SiO_2/Si$ structures," Appl. Phys. Lett. **66** (6), 745 (1995).
37. D. C. Paine, C. Caragianis, T. Y. Kim, Y. Shigesato, and T. Ishara, "Visible photluminescence from nanocrystalline Ge formed by H2 reduction of $Si_{0.6}Ge_{0.4}O_2$," Appl. Phys. Lett. **62** (22), 2842 (1993).

# Chapter 3
# Host Matrix Deposition

Methods of depositing films of silicon and silicon dioxide are reviewed in this chapter. Chemical Vapor Deposition from disilane was chosen to deposit Si films because of the greater reactivity of $Si_2H_6$ compared to $SiH_4$, resulting in higher growth rates at lower temperatures and pressures. Deposition of Si is also known to be enhanced by the presence of Ge, and this would be an advantage in the codeposition of Ge:Si composites. Reactive laser evaporation of Si in the presence of $O_2$ was chosen to deposit $SiO_2$ films, because alternative CVD techniques such as the reaction of $Si_2H_6$ with $O_2$ have extremely low deposition rates under low pressure conditions.

## 3.1 Chemical vapor deposition of Si

### 3.1.1 Deposition from disilane

Silane ($SiH_4$) and chlorosilanes ($SiH_2Cl_2$, $SiHCl_3$, $SiCl_4$) are the most widely used source gases for the chemical vapor deposition of silicon at atmospheric pressure.[1] At low pressures and temperatures, however, the growth rate from these gases drops off dramatically,[2] making them unsuitable for use in the the PLA-SSE vacuum system. Chlorosilanes also produce HCl or $Cl_2$ as by-products, and extra precautions would have to be taken to handle these toxic and corrosive gases.

Higher silanes ($Si_2H_6$ or $Si_3H_8$) can also be used for Si CVD, and higher growth rates are achieved than with monosilane. Hirayama et al.[3,4] have reported the growth of high quality epitaxial silicon using disilane at temperatures as low as 630°C, compared to the 1000°C typically used in $SiH_4$ CVD. The pressure during deposition with $Si_2H_6$ was $2 \times 10^{-5}$ torr, and the growth rate using $Si_2H_6$ was several times higher than that achieved using $SiH_4$ under similar conditions.[3]

The decomposition of $SiH_4$ under low pressure conditions (negligible gas-phase reaction) is well established as proceeding by the following mechanism:[5,6]

$$SiH_4(g) + 2\sigma \rightarrow H(a) + SiH_3(a) \quad (1)$$

$$SiH_3(a) + \sigma \rightarrow H(a) + SiH_2(a) \quad (2)$$

$$2SiH_2(a) \rightarrow H_2\ (g) + 2\ SiH(a) \quad (3)$$

$$2SiH(a) \rightarrow H_2\ (g) + 2\ Si(a) \quad (4)$$

$$2H(a) \rightarrow H_2(g) + 2\sigma \quad (5)$$

$$Si(a) \rightarrow FILM + \sigma \quad (6)$$

where $\sigma$ denotes a surface site, and (a) represents adsorbed species on the surface. At high temperatures, Si growth is adsorption-limited, with the growth rate controlled by $SiH_4$ sticking probability. At low temperature, film growth becomes hydrogen desorption-limited with the growth rate controlled by the decomposition of silicon monohydride, reactions (4) and (5).

In the case of disilane, two channels are possible, incorporation of both Si atoms into the growing film with release of $H_2$:

$$Si_2H_6 \rightarrow 2\ Si(s) + 3\ H_2\ (g) \quad (7)$$

or, incorporation of only one Si atom into the film with release of $SiH_4$ and $H_2$:

$$Si_2H_6 \rightarrow Si(s) + SiH_4\ (g) + H_2\ (g) \quad (8)$$

Kulkarni et al.[7,8] find that for Si (111) substrates at low temperatures, 250°C $< T <$ 425°C, reaction (7) dominates, but above 500°C, $SiH_4$ production increases dramatically and reaction (8) dominates. Xia et al.[9] propose that adsorption of $Si_2H_6$ takes place via:

$$Si_2H_6\ (g) + 2\sigma \rightarrow Si_2H_5(a) + H(a) \quad (9)$$

The adsorbed silasilyl species, $Si_2H_5(a)$, could then undergo a unimolecular decomposition to $SiH_4$:

$$Si_2H_5(a) \rightarrow SiH_4\ (g) + SiH(a) \quad (10)$$

or it could react further on the surface via

$$Si_2H_5(a) + \sigma \rightarrow SiH_2(a) + SiH_3(a) \quad (11a)$$

and

$$Si_2H_5(a) + 2\sigma \rightarrow Si_2H_4(a) + H(a) \quad (11b)$$

which do not produce $SiH_4$ as an end-product. In reaction (10), only one of the Si atoms is incorporated into the growing film with the other Si evolved as $SiH_4$, while in reactions (11a) and (11b), both Si atoms are incorporated into the film.

The relative predominance of the two channels depends on the surface structure and adlayer composition. $SiH_4$ production is observed for Si(111)-(7x7) surfaces and for Si(100)-(2x1) surfaces in the presence of adsorbed H or P atoms but complete pyrolysis to Si and $H_2$ (no $SiH_4$) is observed on clean

Si(100)-(2x1) and Si(111)-"(1x1)" surfaces without production of $SiH_4$. This is explained in terms of steric limitations on the Si(111)-(7x7) surface which retard reaction (11) and favor the production of $SiH_4$ by reaction (10). Comparing clean Si(100)-(2x1) surfaces to those with adsorbed H or P atoms on the surface, the presence of adatoms on the latter would lead to a lower density of dangling bonds and promote the unimolecular decomposition of $Si_2H_5$(a) to $SiH_4$. On Si(100) surfaces, therefore, the desorption of hydrogen continues to play a significant role in the kinetics of Si deposition from disilane.[9,10]

### 3.1.2 Enhancement by Ge

The adsorption of $Si_2H_6$ on Ge has not been as extensively studied as that on Si, and no studies on the adsorption of $Si_2H_6$ on Ge at high temperature have been reported, so it is unclear whether a pathway producing $SiH_4$, analogous to reactions (9) and (10), exists for Ge as well as for Si. At low temperatures ($T < 600°C$), however, adsorption of $Si_2H_6$ is postulated to take place via cleavage of the Si-Si bond to form silicon surface hydrides which decompose to hydrogen,[11,12] in a manner analogous to the reaction of $Si_2H_6$ with Si at low temperatures.

In the deposition of $Si_{1-x}Ge_x$ alloys from mono- or disilane and germane, $GeH_4$, the deposition rate is substantially higher than that for deposition of Si from $SiH_4$ or $Si_2H_6$ alone.[13-17] This growth rate enhancement is attributed to the more rapid desorption of hydrogen from Ge and $Si_{1-x}Ge_x$ alloy surfaces than from pure Si surfaces.[10,13,18,19] The enhanced desorption may occur either through the weakening of Si-H bonds in the presence of Ge, or by migration of H adatoms to Ge sites which then act as desorption centers (the latter model is favoured by most authors).[10,13,18] A corollary of the enhanced $H_2$ desorption from Ge-containing alloys is that the transition from desorption-limited growth to adsorption-limited growth takes place at lower temperatures as the Ge content increases. In an Arrhenius plot of the growth rate of $Si_{1-x}Ge_x$ from $SiH_4$ and $GeH_4$ reported by Jang and Reif,[20] the change in slope associated with the transition from desorption- to adsorption-limited growth occurs at lower substrate temperatures as $x$ increases.

Surface segregation of Ge is observed in the growth of $Si_{1-x}Ge_x$ alloys from $SiH_4$ and $GeH_4$, and in MBE of Si on Ge substrates.[9,21-23] Si diffuses into the

film and the surface of the growing film is richer in Ge than the underlying layers, presumably because the surface energy of Ge is lower than that of Si. This has serious implications for the abruptness of the Si-Ge interface, but the successful fabrication of $Si/Si_{1-x}Ge_x$ quantum well devices suggests that this phenomenon is not an obstacle to the growth of quantum device structures.[24]

The surface "catalytic" effect of Ge is expected to result in the enhanced growth of a Si shell around each Ge cluster. Under appropriate growth conditions, a well passivated Si-Ge interface may also be achieved with a low density of surface defects. We hypothesize that as the Ge nanoclusters land on the substrate they are preferentially coated by Si deposited from $Si_2H_6$, and the space between the Ge nanoclusters would be filled in by polycrytalline or amorphous Si. Ge:Si composites grown by codeposition of PLA-SSE Ge nanoclusters with CVD Si would therefore consist of randomly oriented Ge nanocrystals embedded in a polycrystalline or amorphous Si matrix.

## 3.2 $SiO_2$ deposition

Among the reasons for the continued dominance of silicon in the semiconductor industry are the excellent mechanical and electrical properties of its oxide.[25] In Si nanoclusters, where there is a competition between radiative and non-radiative pathways for exciton recombination, the oxide shell enables photoluminescence by passivating the surface of the nanoclusters and eliminating the non-radiative pathways associated with surface traps (Section 2.4.1) Si nanoclusters were collected directly on TEM grids coated with amorphous carbon and formvar, and examined with a high resolution TEM.[19] Figure 2.2 shows a crystalline Si particle approximately 3 nm in diameter. The lattice fringes have a spacing of 1.6 Å, corresponding to the (311) lattice spacing of diamond cubic Si (JCPDS Card 27-1402).[50] A wide distribution of particle sizes, with diameters ranging from 2 nm to several hundred nanometers, was also observed.

Thin films (8–40 nm) of silica such as that used in gate oxides, capacitor dielectrics, tunneling oxides, diffusion barriers or passivating layers [1] are typically grown by thermal oxidation as that produces high quality oxide films with conformal step coverage, low electrical defect density and high breakdown field strength.[26]

Chemical vapor deposited oxides have higher contaminant concentrations and trap densities than thermal oxides, but have a much higher growth rate. For example, a 100 nm-thick oxide layer can be deposited within 2 minutes by reacting silane and oxygen, $SiH_4 + O_2 \rightarrow SiO + H_2$, at 450°C.[27] It would take one hour of dry oxidation at 1000°C to grow a thermal oxide film of the same thickness. CVD is therefore used to grow thicker (100-700 nm) oxide films such as those used as intermetal insulators, sidewall spacers and protective masks where the advantages of higher growth rate and lower growth temperature outweigh the disadvantage of inferior film quality. A compromise solution is sometimes used where a thin thermal oxide layer is grown first to passivate the silicon surface then a thick CVD oxide film is deposited on top of the thermal oxide.

**3.2.1 Tetraethylorthosilicate(TEOS)**

Tetraethylorthosilicate, also known as tetraethoxysilane ($Si(C_2H_5O)_4$, abbreviated as TEOS), is used as a precursor for $SiO_2$ deposition. Silica films grown from TEOS have excellent uniformity, conformal step coverage and good step coverage.[28] Stoichiometric $SiO_2$ can be deposited using TEOS alone without adding an oxidant by depositing at reactor temperatures above 600°C[29]

$$Si(C_2H_5O)_4 \rightarrow SiO_2 + H_2O + C_2H_4$$

It is more typical, however, to add an oxidant such as oxygen[27,28] or ozone[30]

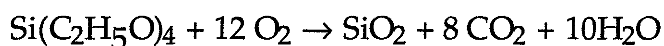

$$Si(C_2H_5O)_4 + 12\ O_2 \rightarrow SiO_2 + 8\ CO_2 + 10H_2O$$

The growth temperature is 650—750°C when oxygen is used and as low as 450°C when ozone is used. TEOS depositions may be performed under atmospheric pressure or low pressure conditions. Plasma-enhanced CVD can also be used to deposit $SiO_2$ from $SiH_4$-$N_2O$, $SiH_4$-$O_2$ or $SiH_4$-$CO_2$ mixtures.[27]

TEOS, however, is a liquid at room temperature and pressure, so a bubbler would have to be used to vaporize it prior to introduction into the reaction chamber. In addition, even when ozone is used as the oxidant, the deposition rate is negligible below 0.01 torr.[30] TEOS is therefore unsuitable for use in our high vacuum PLA-SSE system because of the low $SiO_2$ deposition rate and the need for a bubbler.

### 3.2.2 Oxidation of silane or disilane

Silicon dioxide films can be deposited by the direct oxidation of silane at 300–500°C[27,28]

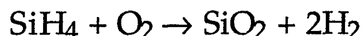

$$SiH_4 + O_2 \rightarrow SiO_2 + 2H_2$$

Atmospheric pressure or low pressure deposition systems are used, but atmospheric pressure systems suffer from poor uniformity and non-conformal step coverage. The growth rate in low pressure (0.1–1 torr) systems, however, is much lower than in atmospheric pressure systems (~10 nm/min compared to ~100 nm/min).[27]

Disilane can also be used as the silicon source for low-temperature $SiO_2$ deposition[31]

$$Si_2H_6 + {}^7/_2\, O_2 \rightarrow 2SiO_2 + 3H_2O \quad (12)$$

Mishima et al. report growth rate data for the reaction of 1% $Si_2H_6$ (diluted in He) with $O_2$ at atmospheric pressure (curve labelled "thermal CVD" in Figure 3.1) Fitting a straight line to the data below 300°C, the activation energy for this reaction is calculated to be 22 kcal $mol^{-1}$ $K^{-1}$, and the reaction probability for $Si_2H_6$ molecules striking the $SiO_2$ surface at 300 °C is $10^{-5}$. The downturn in growth rate above 300 °C is due to gas phase reaction of $Si_2H_6$ and $O_2$, and illustrates the pyrophoric nature of $Si_2H_6$ despite its relatively low concentration of 0.01 mole percent. The curve labelled "photo CVD" is for photo-activated deposition carried out in the presence of a low pressure Hg ultraviolet lamp.

### 3.2.3 Physical Vapor Deposition

Silica films can also be deposited by thermal evaporation of solid silicon dioxide.[32,33] Since the crucible, heater and support assembly are all heated to very high temperatures, however, they tend to release contaminants which are then incorporated into the deposited film.

Electron-beam evaporation is also used to deposit $SiO_2$.[34] With electron-beam evaporation, only the point of e-beam contact with the target is heated while the rest of the system remains cold, so contamination levels are much lower than in the case of thermally evaporated films. The power required is also less than that for thermal evaporation.

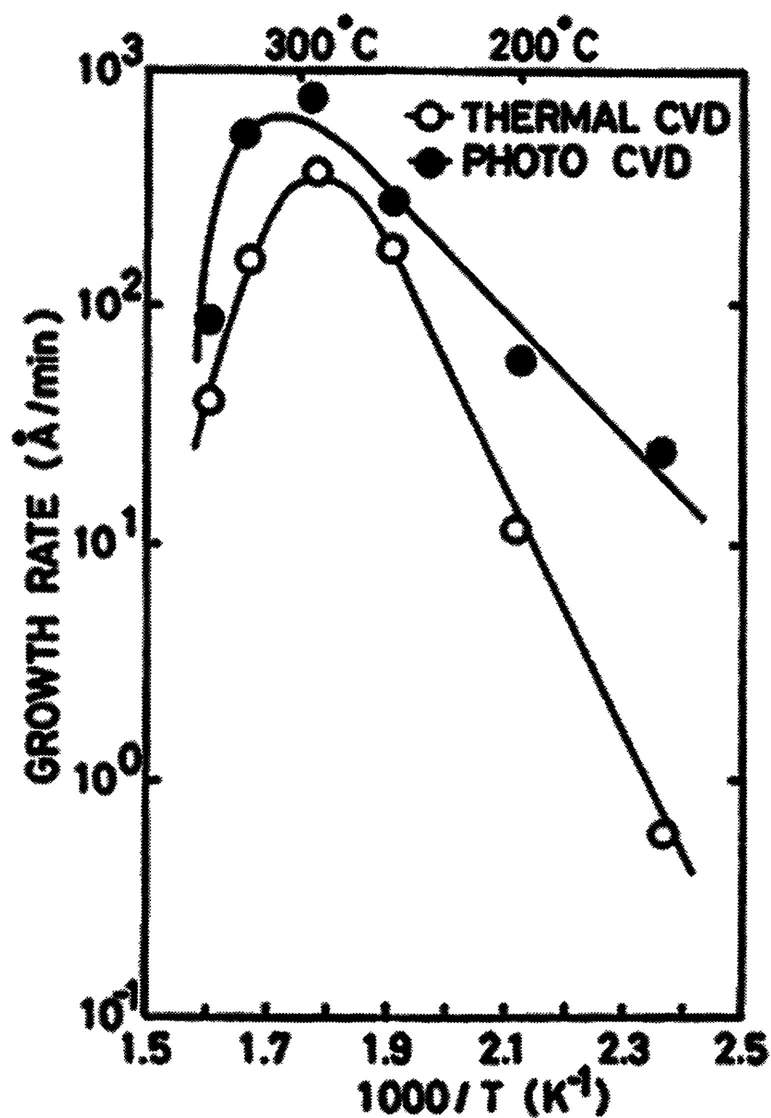


Figure 3.1 Arrhenius plot for the reaction $Si_2H_6 + O_2$ at atmospheric pressure. Silica is deposited by passing disilane(diluted to 1% in He), $O_2$ and $N_2$ at flow rates of 200, 600 and 1500 cc/min respectively over a heated Si wafer substrate. Points labelled "Photo CVD" are for photoactivated (low pressure Hg lamp) depositions. (From Mishima et al., 1984)

Radio Frequency (RF) sputtering of a fused silica target can also be used to deposit $SiO_2$ for use as a dielectric in multilayer interconnect structures.[1] Pawlewicz et al.[35] have also reported using DC magnetron sputtering to deposit $SiO_2$ by sputtering Si in the presence of oxygen. Sputter-deposited films, however, tend to be vulnerable to contamination and since a minimum pressure of 10 mtorr is required to maintain the glow discharge,[1] sputter deposition would not be possible in the PLA-SSE system.

Evaporations are typically performed under high vacuum($10^{-6}$ torr) to ensure film purity, so an evaporation process is compatible with our PLA-SSE system. As it would be difficult to add a thermal evaporator or e-beam evaporator to our system, we decided to use laser evaporation instead.

$SiO_2$ films have been deposited using a pulsed ArF excimer laser (193 nm wavelength) to evaporate Si, SiO or $SiO_2$(fused silica) targets.[36] When Si or SiO targets were laser ablated under vacuum of approximately $10^{-5}$ torr, the deposited films were substoichiometric. Films deposited at the same pressure using $SiO_2$ targets had an O/Si ratio of 2. When the evaporations were conducted under an oxygen pressure of 0.1 torr, the O/Si ratio increased to 2 regardless of target material. The refractive index of $SiO_2$ films deposited using an SiO target was 1.455, compared to 1.457 for high-temperature thermally-grown $SiO_2$ (wavelength of measurement was not specified). The excimer laser used by Fogarassy et al. delivered 300 mJ/pulse at 50 Hz, and was focussed onto a rotating target disk at normal incidence. Si wafer substrates were placed 3 cm away from the target.

Since $SiO_2$ is transparent at the green 532 nm wavelength of our Nd:YAG lasers, it was not possible to use $SiO_2$ targets even though $SiO_2$ would have been ideal as it produces stoichiometric film deposits even in vacuum, without requiring the presence of an oxidant such as $O_2$. We therefore decided to deposit $SiO_2$ host matrices by laser evaporation of Si targets in the presence of $O_2$. This process is described in greater detail in Chapter 5.

#### 3.2.4 Active vs. passive oxidation of silicon

In CVD and MBE systems, the native oxide layer present on Si wafers is often removed by baking the wafer in hydrogen or in vacuum at high temperatures of around 800–1200°C so that the $SiO_2$ is reduced to silicon monoxide, SiO, which volatilizes, leaving bare Si.[24] In the oxidation of Si by

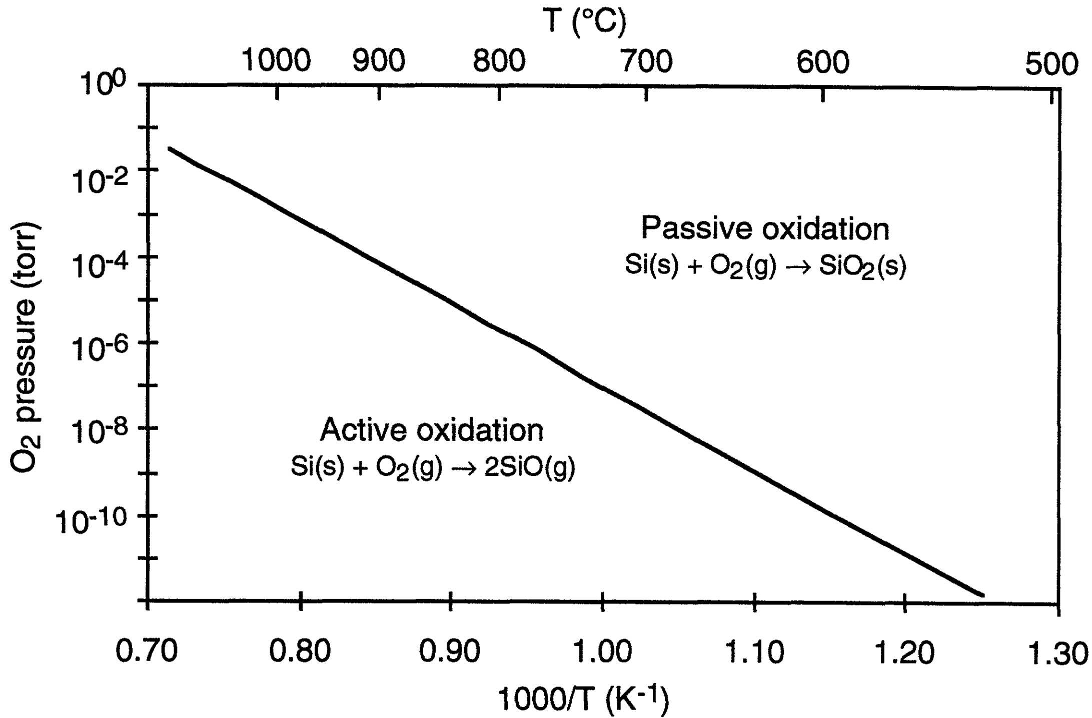


Figure 3.2 Critical presssure for transition between active and passive oxidation on Si(100). Below the curve, Si is etched by the formation of gaseous SiO, and above the curve, passive oxidation takes places with the deposition of solid $SiO_2$.

dry $O_2$ or $H_2O$, both $SiO_2$ and SiO may also be formed. At high temperatures and low $O_2$ pressures, the Si surface is etched by the evolution of gaseous SiO in a process known as "active" oxidation,[37]

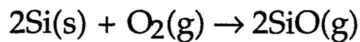

$2Si(s) + O_2(g) \rightarrow 2SiO(g)$

At higher $O_2$ pressures, "passive" oxidation takes place instead where a layer of solid $SiO_2$ is deposited on the surface,

$Si(s) + O_2(g) \rightarrow SiO_2(s)$

The $SiO_2$ film then impedes subsequent oxidation as $O_2$ has to dissolve in the $SiO_2$ layer and diffuse to the Si-$SiO_2$ interface to react with Si from the substrate. The transition from active to passive oxidation was modelled by Smith and Ghidini[38] as:

$$P_c\,(T_s) = P_o \exp\left(\frac{-\Delta E}{k_B T_s}\right) \qquad (12)$$

where $P_c$ is the minimum $O_2$ pressure at which an $SiO_2$ film forms on clean Si wafers at a temperature $T_S$. $P_o$ and $\Delta E$ were determined by experiment, and for Si(100), $P_o = 2 \times 10^{12}$ torr and $\Delta E = 3.83$ eV. Within the limits of experimental error, the parameters for Si(111) were the same as those for Si(100) wafers. Equation (12) is plotted in Figure 3.2 as an Arrhenius plot: below the solid line, Si(100) is etched by $O_2$ with production of SiO(g) while above the line, passive oxidation takes place with formation of an $SiO_2$ film.

In the reactive laser evaporation process I used to deposit silicon oxide films, Si was evaporated from a solid Si target by laser heating and deposited on a Si(100) substrate in the presence of ~ $10^{-4}$ torr of $O_2$ gas. The substrate is held at room temperature or moderately heated ($T_s$ = 500°C). Under these conditions, passive oxidation would be expected to prevail. However, film growth is not taking place through oxidation of the Si wafer substrate, but through reaction of Si evaporated from the target. This Si must have a temperature of at least the melting point of Si, 1412°C (liquid Si droplets are ejected from the target as well as gaseous Si). At these temperatures, active oxidation of Si producing silicon monoxide would be favoured, so a fraction of the evaporated Si may in fact be evolved as SiO(g) or trapped in pores within the deposited solid silicon oxide film.

The direct reaction of evaporated Si with $O_2$ gas is a simple means of depositing silicon oxide films. However, under high temperature and low $O_2$ partial pressure, this technique may result in "active" rather than "passive" oxidation of silicon, i.e., the production of a volatile silicon monoxide reaction product instead of a solid silica film.

## REFERENCES


1. S. Wolf and R. N. Tauber, *Silicon Procesing for the VLSI Era* (Lattice Press, 1986).
2. J. C. Bean, "Silicon molecular beam epitaxy: highlights of recent work," J. Electron. Mater. **19** (10), 1055 (1990).
3. H. Hirayama, T. Tatsumi, and N. Aizaki, "Gas source silicon molecular beam epitaxy using disilane," Appl. Phys. Lett. **52** (18), 1484 (1988).
4. H. Hirayama and T. Tatsumi, "High doping of phosphorous in Si using gas source molecular beam epitaxy," Appl. Phys. Lett. **55** (2), 131 (1989).
5. S. M. Gates, C. M. Greenlief, S. K. Kulkarni, and H. H. Sawin, "Surface reactions in Si chemical vapor deposition from silane," J. Vac. Sci. Technol. A **8** (3), 2965 (1990).
6. S. M. Gates and S. K. Kulkarni, "Kinetics of surface reactions in very low-pressure chemical vapor deposition of Si from $SiH_4$," Appl. Phys. Lett. **58** (25), 2963 (1991).
7. S. K. Kulkarni, S. M. Gates, B. A. Scott, and H. H. Sawin, "Modulated molecular beam scattering of disilane on silicon," Surf. Sci. **239**, 13 (1990).

8. S. K. Kulkarni, S. M. Gates, C. M. Greenlief, and H. H. Sawin, "Mechanisms of disilane decomposition on Si(111)-7x7," Surf. Sci. **239**, 26 (1990).
9. L.-Q. Xia, M. E. Jones, N. Malty, and J. R. Engstrom, "Dissociation and pyrolysis of $Si_2H_6$ on Si surfaces: The influence of surface structure and adlayer composition," J. Chem. Phys. **103** (4), 1691 (1995).
10. Y. M. Wu and R. M. Nix, "Adsorption of hydrogen and disilane on Si(100) and Si-Ge surfaces," Surf. Sci. **306**, 59 (1994).
11. D.-S. Lin, T. Miller, and T. C. Chiang, "Adsorption and thermal reactions of disilane and the growth of Si films on Ge(100)-(2x1)," Phys. Rev. B **47** (11), 6543 (1993).
12. H. Akazawa, "Kinetics of Si growth on Ge(100) in $Si_2H_6$ gas-source molecular beam epitaxy and low-pressure chemical vapor deposition," Surf. Sci. **323**, 269 (1995).
13. B. S. Meyerson, K. J. Uram, and F. K. LeGoues, "Cooperative growth phenomena in silicon/germanium low-temperature epitaxy," Appl. Phys. Lett. **53** (25), 2555 (1988).
14. M. Racanelli and D. W. Greve, "Temperature dependence of growth of $Ge_xSi_{1-x}$ by ultrahigh vacuum chemical vapor deposition," Appl. Phys. Lett. **56** (25), 2524 (1990).
15. D. J. Robbins, J. L. Glasper, A. G. Cullis, and W. Y. Leong, "A model for heterogeneous growth of $Si_{1-x}Ge_x$ films from hydrides," J. Appl. Phys. **69** (6), 3729 (1991).
16. A. Yamada, M. Tanda, F. Kato, M. Konagai, and K. Takahashi, "Gas source molecular beam epitaxy of Si and SiGe using $Si_2H_6$ and $GeH_4$," J. Appl. Phys. **69** (2), 1008 (1991).
17. D. J. Tweet, T. Tatsumi, H. Hirayama, K. Miyanga, and K. Terashima, "Factors determining the composition of strained germanium-silicon layers grown with disilane and germane," Appl. Phys. Lett. **65** (20), 2579 (1994).
18. B. M. H. Ning and J. E. Crowell, "Investigation on the growth rate enhancement by Ge during SiGe alloy deposition by chemical vapor deposition," Appl. Phys. Lett. **60** (23), 2914 (1992).
19. L. Surnev and M. Tikhov, "Comparative study of hydrogen adsorption on Ge(100) and Ge(111) surfaces," Surf. Sci. **138**, 40 (1984).
20. S.-M. Jang and R. Reif, "Temperature dependence of $Si_{1-x}Ge_x$ epitaxial growth using very low pressure chemical vapor deposition," Appl. Phys. Lett. **59** (24), 3162 (1991).
21. D. J. Gravesteijn, P. C. Zalm, G. F. A. Van de Walle, C. J. Vriezema, A. A. van Gorkum, and L. J. van Ijzendoorn, "Ge segregation during molecular beam epitaxial growth of $Si_{1-x}/Ge_x/Si$ layers," Thin Solid Films **183**, 191 (1989).
22. Z. H. Lu, J. M. Baribeau, and D. J. Lockwood, "Surface segregation during $Si/Ge_n/Si(100)$ interface formation," J. Appl. Phys. **76** (6), 3911 (1994).
23. K. Nakagawa and M. Miyao, "Reverse temperature dependence of Ge surface segregation during Si-molecular beam epitaxy," J. Appl. Phys. **69** (5), 3058 (1991).
24. M. Racanelli and D. W. Greve, "Ultrahigh-vacuum CVD epitaxy of silicon and $Ge_xSi_{1-x}$," JOM **43** (10), 32 (1991).
25. P. Balk, "Introduction," in *The $Si$-$SiO_2$ system*, edited by P. Balk (Elsevier, Amsterdam, 1988), p. 3.
26. S. Rojas, A. Modelli, W. S. Wu, A. Borghesi, and B. Pivac, "Properties of silicon dioxide films prepared by low-pressure chemical vapor deposition from tetraethylorthosilicate," J. Vac. Sci. Technol. B **8** (6), 1177 (1990).
27. S. K. Ghandhi, *VLSI Fabrication Principles Silicon and Gallium Arsenide* (John Wiley & Sons, New York, 1983).
28. A. C. Adams, "Dielectric and polysilicon film deposition," in *VLSI Technology*, edited by S. M. Sze (McGraw-Hill, New York, 1988), p. 250.
29. F. S. Becker, D. Pawlick, H. Anzinger, and A. Spitzer, "Low-pressure deposition of high-quality $SiO_2$ films by pyrolysis of tetraethylorthosilicate," Journal of Vacuum Science and Technology BJournal of Vacuum Science and Technology B **5**, 1555 (1987).
30. K. D. Stonnington, K. Y. Hsieh, L. L. H. King, K. J. Buchanan, and A. I. Kingon, "Synthesis and characterization of $SiO_2$ films deposited using tetraethylorthosilicate/ozone at low processing pressures ($10^{-1}$ to $10^{-3}$ torr)," J. Vac. Sci. Technol. A **10**, 970 (1992).

31. Y. Mishima, M. Hirose, and Y. Osaka, "Direct photochemical deposition of $SiO_2$ from the $Si_2H_6 + O_2$ system," J. Appl. Phys. **55** (4), 1234 (1984).
32. P. Archibald and E. Parent, "Source evaporant systems for thermal evaporation," Solid State Technol. **19** (7), 32 (1976).
33. M. Ohring, *The materials science of thin films* (Academic Press, Boston, 1992).
34. E. B. Graper, "Evaporation characteristics of materials from an electron beam gun II," J. Vac. Sci. Technol. A **5** (4), 2718 (1987).
35. W. T. Pawlewicz, P. M. Martin, R. W. Knoll, and I. B. Mann, "Multilayer optical coating fabrication by DC magnetron reactive sputtering," in *Optical Thin Films II:New Developments* (1986), Vol. 678, pp. 134.
36. E. Fogarassy, C. Fuchs, A. Slaoui, S. de Unamumo, and J. P. Stoquert, "Low-temperature synthesis of silicon oxide, oxynitride, and nitride films by pulsed excimer laser ablation," J. Appl. Phys. **76** (5), 2612 (1994).
37. C. Wagner, "Passivity during the oxidation of silicon at elevated temperature," J. Appl. Phys. **29** (9), 1295 (1958).
38. F. W. Smith and G. Ghidini, "Reaction of oxygen with Si(111) and (100): Critical conditions for the growth of $SiO_2$," J. Electrochem. Soc. **129** (6), 1300 (1982).

# Chapter 4
# Ge Nanocluster:Si Host Composites

Nanostructured composites consisting of Ge nanoclusters embedded in a Si host matrix were synthesized by combining the PLA-SSE process for synthesizing Ge nanoclusters with chemical vapor deposition for depositing Si. X-ray diffraction showed that the Si host was polycrystalline, and Rutherford Backscattering showed that the composites contained approximately one atomic percent Ge. Element maps collected by X-ray spectroscopy in a Scanning Transmission Electron Microscope showed that the composites consisted of Ge nanoparticles surrounded by a Si host. No visible or infrared ($\lambda \leq 1.8$ µm) photoluminescence was observed from the Ge:Si composites or from Ge nanoclusters collected without a host matrix.

## 4.1 Deposition system

The Pulsed Laser Ablation-Chemical Vapor Deposition (PLA-CVD) apparatus consists of two vacuum chambers connected by an 8" gate valve (Figure 4.1). The primary chamber contains the PLA-SSE cluster source and is of stainless steel construction with inside dimensions of approximately 28"L x 22"H x 22"D. The chamber is evacuated to a base pressure of ~ $5 \times 10^{-8}$ torr with a Varian VHS-10 diffusion pump. A water-cooled baffle above the diffusion pump minimises backstreaming of Dow Corning DC 704 diffusion pump fluid from the pump.

The secondary chamber is approximately 18"L x 12"H x 12"D (inside dimensions) and is pumped with a Varian VHS-8 diffusion pump filled with Santovac 5 diffusion pump fluid. A liquid nitrogen-filled cryotrap is installed above the gate valve and used as a cryopump during disilane CVD. The ultimate pressure achieved without using the liquid nitrogen cryo-trap is < $5 \times 10^{-8}$ torr.

The pumping speed of the primary chamber was estimated to be 2,000 l/s using the approximate method described by O'Hanlon.[1] This is close to the manufacturer's specifications for the diffusion pump with the baffle installed. The secondary chamber pumping speed, however, was estimated at 150 l/s, much lower than the 1,200 l/s specified for the diffusion pump with cryotrap

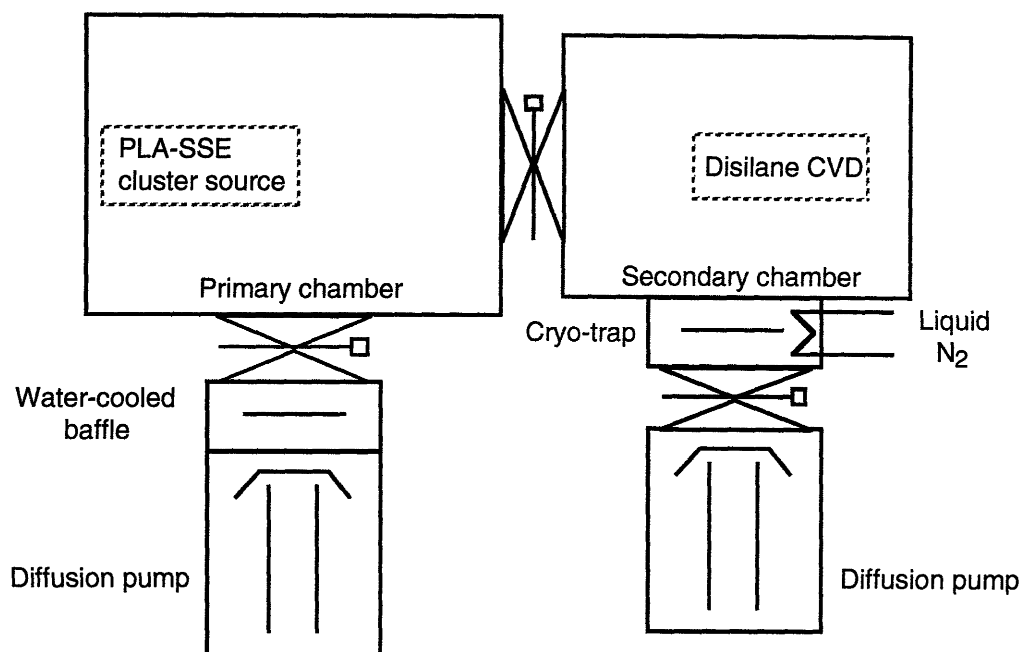


Figure 4.1 Pulsed Laser Ablation-Chemical Vapor Deposition (PLA-CVD) apparatus. The system consists of two diffusion-pumped vacuum chambers connected through an 8" gate valve with the PLA-SSE cluster source in the primary chamber and the disilane CVD system in the secondary chamber.

installed. The gate valve was originally installed above the cryotrap, but their positions were reversed when the system was modified for disilane CVD service (see Figure 4.1). A 12" long nipple then had to be installed between the cryotrap and the gate valve as a flange adapter. This extra section reduced the conductance of the pumping system and substantially reduced the pumping speed measured at the secondary chamber.

Both diffusion pumps are backed by rotary vane pumps which are also used to rough the chambers. Thermal conductivity and ionization gauges are installed in both chambers. A skimmer cone for extracting a molecular beam[2] of nanoclusters can also be installed in the system. However, it was not used during the course of this thesis work.

Nanoclusters are synthesized by PLA-SSE (see Section 2.1) in the primary chamber and collected in the secondary chamber where a silicon matrix is grown by chemical vapor deposition from disilane. The substrate heater con-

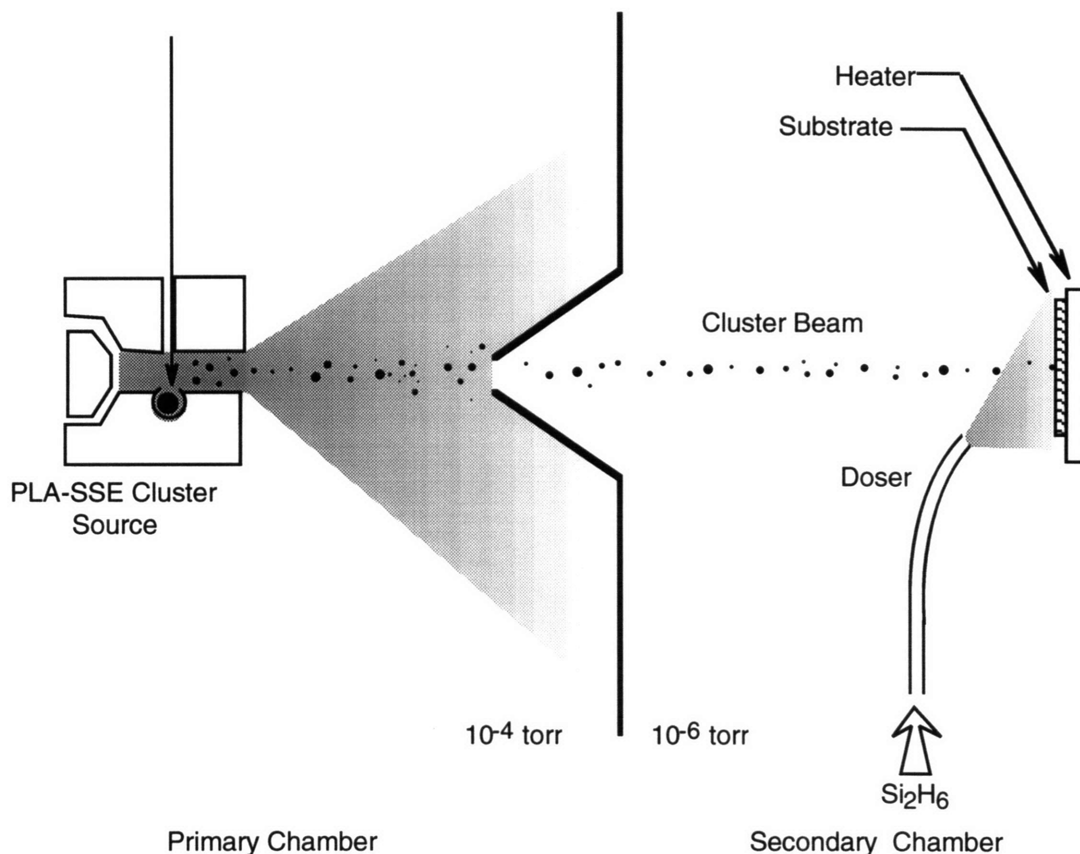


Figure 4.2 Schematic diagram of Pulsed Laser Ablation- Chemical Vapor Deposition apparatus. Nanoclusters are collected on a heated substrate in the secondary chamber while a silicon matrix is simultaneously deposited using disilane. The working pressure in the secondary chamber is ~$10^{-6}$ torr while the pressure in the primary chamber is ~$10^{-4}$ torr.

sists of a Boralectric heating element (Pyrolytic Boron Nitride with electrically conductive films of Pyrolytic Graphite, Advanced Ceramics Corporation) sandwiched between two 0.5 mm-thick Mo sheets. The assembly is mounted vertically along the center-line, 17" downstream of the PLA-SSE cluster source (Figure 4.2). The heater assembly and mounting post were detachable and were removed in between runs to accomodate other users of the PLA-SSE system.

Samples are clamped onto the heater using screw-on Mo clips. Two type K

thermocouples were spot-welded onto stainless steel washers and screwed onto the heater face. AC power for the Boralectric heating element is supplied by a variable transformer through Cu leads insulated with fibre-glass sleeving. During calibration checks, the temperature measured with a thermocouple cemented onto a Si wafer clamped onto the heater was typically 20–30 °C lower than that measured with the thermocouples in direct contact with the Mo face. It should be borne in mind that the high-temperature cement used is itself an insulator, so the actual temperature of the Si wafer will be intermediate between the two values. All deposition temperatures reported in this work are *heater* temperaures. The heater temperature was controlled by manual adjustment of the output voltage from the variable transformer. Typically, ~ 34 V would be applied at a heater temperature of 800°C with the current ~ 6 A.

A lecture bottle of 99.998% disilane (Voltaix, Inc.) was stored in the fume hood and the gas† piped to the secondary chamber through $^1/_4$"stainless steel tubes electropolished on their inner surfaces. VCR face seal fittings with stainless steel gaskets were used to connect tube sections, and the disilane admitted into the chamber through a Fisons MD-5 leak valve. Inside the chamber, a $^1/_8$" stainless steel tube directed at the center of the substrate was used as the doser. The tip of the doser was 3 cm away from the substrate.

Disilane is a pyrophoric gas that is spontaneously flammable in air, so it was crucial to ensure that $Si_2H_6$ was not exposed to air except when diluted in large quantities of inert gas. The liquid nitrogen-cooled cold trap on the secondary chamber was therefore used to trap disilane during deposition runs and prevent it from entering the diffusion pump or mechanical backing pump. Following a deposition run, the cryotrap would be isolated from the pumps, and the secondary chamber together with the interior of the cryotrap flushed with $N_2$. The cold trap is warmed up by displacing the cryogen with compressed air, releasing disilane and other condensed species into the secondary chamber where they are diluted with a large flow of $N_2$ and exhausted into the fume hood. During a deposition, the temperature of the cryotrap was monitored with a temperature alarm to ensure that sufficient cryogen was present to trap the disilane. Full details of the standard operating procedure and safety precautions are given in Appendix A.1

---

† The boiling point of disilane is -14°C and the vapor pressure is 33 psig at 70°F.

The Si substrates consisted of ~ 1 cm squares cleaved from p-type (100) Si wafers (Semiconductor Processing Corporation) of $^{20}/_{1000}$" thickness and degreased by boiling in acetone and then in methanol. The substrates were dipped in aqueous HF ( 1 part 48% HF diluted with 10 parts deionized water) and blow-dried with $N_2$, then mounted on the heater and the heater assembly mounted in the secondary chamber. The secondary chamber is then roughed and diffusion pumped to a pressure of $< 5 \times 10^{-7}$ torr. The heater is ramped up to the deposition temperature and the $Si_2H_6$ valve opened to commence Si deposition.

Before the Si substrate is mounted in the secondary chamber, the PLA-SSE cluster source is set up and tested by using a Fast Ionization Gauge (FIG, see Section 5.2.1.2) to verify that clusters are being produced.[3] The FIG is removed from the secondary chamber prior to $Si_2H_6$ CVD to avoid deposition of Si on the FIG filament or on the collector and grid wires.

To synthesize Ge cluster:Si host composites, the interchamber valve is opened so that PLA-SSE clusters generated in the primary chamber are deposited on the heated substrate and a Si matrix grown around them by $Si_2H_6$ CVD. Typical operating pressures are $10^{-4}$ torr in the primary chamber and $5 \times 10^{-6}$ torr in the secondary chamber.

Two limitations of the PLA-CVD system are the inability to monitor PLA-SSE cluster production during a CVD run and the lack of a load lock on the secondary chamber. The PLA-SSE cluster source occasionally clogs up due to the build-up of deposits inside the 1 mm-diameter growth channel. When CVD is not being performed, this can be detected as a reduction in the cluster FIG signal. However, the FIG cannot be installed during CVD runs for fear of depositing Si on the FIG filament and on the grid and collector wires. It is thus not possible to detect the cessation or reduction of cluster generation during a CVD run.

The absence of a load lock on the vacuum chamber requires the secondary chamber to be exposed to atmosphere, roughed and pumped down every time a sample is loaded into the system. More than three hours will therefore elapse between the time that the Si wafer is dipped in HF and the commencement of Si deposition. About 10–20 minutes is spent in air, another 10 minutes under roughing pump vacuum and the remainder under diffusion pump vacuum.

Several groups[4-6] have reported that hydrogen passivation of a Si surface

following an HF etch is sufficient to prevent oxide growth and contamination of the Si surface prior to deposition. Meyerson et al.[7] were unable to detect any $SiO_2$ on the surface of a Si wafer that was dipped in dilute HF then exposed to room air for 10 minutes. Synchrotron radiation photoemission spectroscopy showed that the Si surface was terminated by ~ 0.85 monolayer silicon hydride, ~ 0.1 monolayer flouride and ~ 0.05 monolayer oxide or hydroxide. From the temperature programmed desorption spectrum of hydrogen from Si(100), Meyerson et al. estimated that the activation energy for desorption is 59.4 ± 2 kcal/mol and the pre-exponential factor is $2 \times 10^{15}$. The desorption rate of hydrogen from Si in vacuum at low temperatures is therefore extremely low: less than 0.005 ML/min below 400°C.

Niwano et al.[6] monitored the Si-H stretch using infrared spectroscopy and found that the intensity of the Si-H peak remained at 95% and 87% of its original value after exposure of a HF-dipped Si(100) wafer to dry $O_2$ for 1 hour and 2 hours respectively. Oxidation was strongly accelerated by $H_2O$, however, with the Si-H peak diminishing to 54% and 38% of its original intensity after exposure to air (40% relative humidity) for 1 and 2 hours respectively.

In the PLA-CVD system, the sample is exposed to pressures of $10^{-6}$ – $10^{-4}$ torr for several hours as the chamber is pumped down. At $10^{-6}$ torr, the molecular flux at a surface is equivalent to one monolayer every 2 seconds. Notwithstanding the passivating properties of the hydride layer on the Si layer, it is quite likely that some contamination of the Si surface takes place before $Si_2H_6$ CVD commences, especially since $H_2O$ is a major component of the residual gases in the chamber.

In addition, the chamber cannot be baked-out prior to inserting the sample so when the heater is switched on, the chamber walls are radiatively heated and start to outgas. Water and hydrocarbons released from the walls are then incorporated into the growing Si film. Auger Electron Spectroscopy (AES) analysis of a Ge:Si composite film in fact showed the presence of 3–5% of C and O.

A common means of reducing contamination levels in a vacuum chamber is to bake out the chamber so that adsorbates on the chamber walls are outgassed prior to starting an experiment. In our apparatus, however, the lack of a load lock makes it impossible to load the sample after bake-out. If the sample is mounted in the chamber during bake-out, outgassed material from the walls would simply end up being deposited onto the sample before the Si

film is deposited.

## 4.2 Film growth kinetics

Detailed mechanistic models for the pyrolysis of $Si_2H_6$ have been proposed and are reviewed in Section 3.1 However, there is a paucity of reaction rate data for the elementary steps in models such as those put forward by Xia et al.[8], so for simplicity I will use an earlier model proposed by Buss et al.[9] In this model (see Section A.2 in the appendix), the Reactive Sticking Coefficient, RSC, is defined as the Si deposition rate divided by twice the incident $Si_2H_6$ flux, and the deposition taken to proceed as follows,

$$Si_2H_6 + *-*-* \rightarrow 3SiH_2* \quad (6)$$

$$2SiH_2* \rightarrow SiH_4 + *-* \quad (4)$$

$$SiH_2* \rightarrow * + H_2 \quad (5)$$

where * represents a surface site and no distinction is made between * and Si*. The reactions are numbered as in Buss et al.[9] for ease of comparison. This is a simplified reaction mechanism, and more detailed alternative mechanisms are discussed in Section 3.1 However, Buss et al. found that their simple model was able to predict the growth rate of Si from $Si_2H_6$ under typical Si deposition conditions

Buss et al.'s model was used to predict the silicon growth rate in the PLA-CVD system and compared to growth rate data for the Ge cluster:Si host composites (Figure 4.3). The disilane flux was set to $1.3 \times 10^{15}$ $cm^{-2}$ $s^{-1}$ and $2.6 \times 10^{14}$ $cm^{-2}$ $s^{-1}$ respectively for $P_{Si_2H_6}$ of $5 \times 10^{-6}$ and $1 \times 10^{-6}$ torr. A Si density of $5 \times 10^{22}$ atoms $cm^{-3}$ was then used to convert reactive sticking coefficients, RSC($Si_2H_6$), to film growth rates in units of µm/hr.

The Si substrates were partially masked and the step heights following deposition measured by profilometry to obtain the growth rate. The standard deviation of growth rate was estimated at 15% by measuring the step height at 7 points across the sample deposited at 740 °C. Arrows indicating $2\sigma$ error bars are shown for each data point.

The experimental points were collected with $Si_2H_6$ partial pressures of 3–9 $\times 10^{-6}$ torr, while the dashed line was calculated for a disilane flux equivalent to $5 \times 10^{-6}$ torr. The model thus provides a reasonable estimate of the silicon deposition rate. It should be borne in mind that the ionization gauge was not calibrated, so there is a fairly large uncertainty in pressure measurements. In

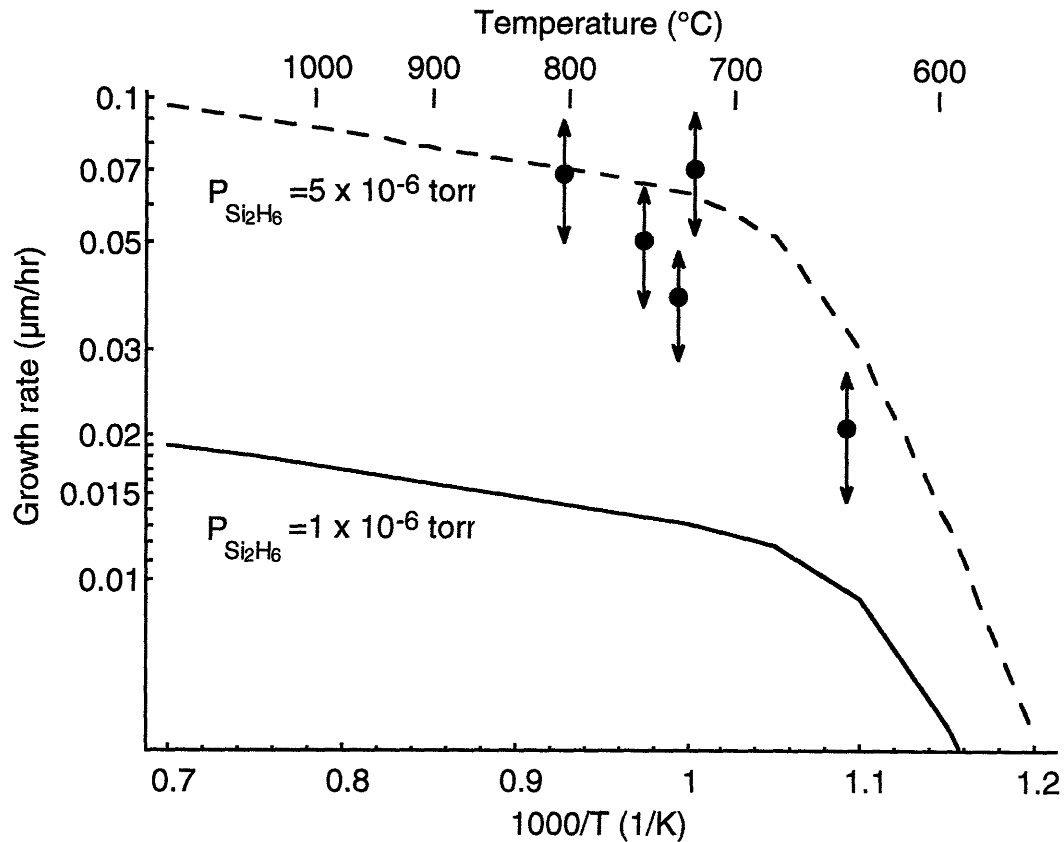


Figure 4.3 Comparison of measured growth rates of Ge cluster:Si host composites to predicted growth rates for deposition of pure Si. The Ge content of the Ge:Si composites is less than 1 atomic percent, and the composites grown at $Si_2H_6$ partial pressures of 3–6 x $10^{-6}$ torr. Model predictions were made for $Si_2H_6$ partial pressures of 1 x $10^{-6}$ torr and 5 x $10^{-6}$ torr. The standard deviation of step heights across a sample was 15%, and $2\sigma$ error bars are shown as arrows for each experimental data point.

addition, the wafer surface is expected to be cooler than the temperature indicated by thermocouples attached to the heater surface.

Ge has been shown to accelerate the eposition of Si from silane and disilane by enhancing the desorption of hydrogen from the surface (Section 3.1.2). However, the Ge content of Ge:Si composites deposited by PLA-CVD is less than 1 at. % (Section 4.3.1) Consistent with literature reports, this is too

low to have a significant effect on the composite deposition rate.

At high temperatures, silicon deposition becomes limited by adsorption of disilane rather than desorption of hydrogen. The activation energy for adsorption is 2 500 cal $mol^{-1}$ $K^{-1}$ compared to 54 000 cal $mol^{-1}$ $K^{-1}$ for the desorption step. The temperature dependence of silicon deposition thus diminishes at higher temperatures. The highest temperature used in PLA-CVD Ge:Si composite depositions was 800°C. Even at 1200°C, however, the predicted Si deposition rate is only 0.1 µm/hr with a disilane partial pressure of $5 \times 10^{-6}$ torr. The major factor controlling the Si deposition rate is the flux of $Si_2H_6$ to the substrate, but the pressure in the secondary chamber is limited to $< 10^{-5}$ torr during Ge:Si composite deposition. This limit is imposed to minimize backflow of $Si_2H_6$ into the primary chamber, which is at a pressure of $10^{-4}$ torr during PLA-SSE cluster production. The Si deposition rate thus cannot be substantially increased due to the limit on the secondary chamber pressure.

## 4.3 Macroanalysis

The Ge:Si composites were analyzed by Ruthford Backscattering Spectrometry and X-ray diffraction to determine the overall film composition and crystallinity, and the microstructure investigated by electron microscopy. Element distributions at the nanometer-scale were determined by X-ray spectroscopy using a Scanning Transmission Electron Microscope (STEM). Electron diffraction in a high resolution Transmission Electron Microscope (TEM) provided evidence of nanocrystalline structure in the Ge:Si composite.

### 4.3.1 Rutherford Backscattering Spectrometry

Analysis of a material by backscattering of an ion beam takes its name, Rutherford Backscattering Spectrometry (RBS), from Lord Ernest Rutherford who established the nuclear model of matter by showing that the backscattering of α-particles ($He^{2+}$) from a metal foil was explained by the mass of an atom being concentrated in a small volume[10]. The term "RBS" is applied today to instruments where the ion beam is generated by electrostatic particle accelerators rather than natural radioactive sources.

Collisions between projectile and target particles in RBS are assumed to be elastic so the energy of the backscattered particle can be calculated from

conservation of energy and momentum,[11-13]

$$K \equiv \frac{E_1}{E_0} = \left[ \frac{(M_2^2 - M_1^2 \sin^2\theta)^{1/2} + M_1 \cos\theta}{M_2 + M_1} \right]^2 \tag{4.1}$$

where K is defined as the kinematic scattering factor, $E_0$ and $E_1$ are the energy of the projectile of mass $M_1$ before and after collision with a target atom of mass $M_2$, and $\theta$ is the scattering angle (see Figure 4.4). Co-ordinates are taken to be in a laboratory frame of reference.

For backscattering angles close to 180°, Equation 4.1 reduces to

$$K = \left( \frac{M^2 - M^1}{M^2 + M^1} \right)^2 \tag{4.2}$$

The number of backscattered particles detected by a detector of solid angle $\Omega$, is expressed as

$$\left( \begin{array}{c} \text{number of} \\ \text{detected particles} \end{array} \right) = \sigma \Omega \left( \begin{array}{c} \text{total number of} \\ \text{incident projectiles} \end{array} \right) \left( \begin{array}{c} \text{number of target} \\ \text{atoms per unit area} \end{array} \right)$$

where $\sigma$ is the differential scattering cross-section, commonly abbreviated to the "scattering cross-section" and is given by

$$\sigma = \left( \frac{Z_1 Z_2 e^2}{4E_0} \right)^2 \frac{4}{\sin^4\theta} \frac{\left\{ \left[ 1 - \left( \frac{M_1}{M_2} \sin\theta \right)^2 \right]^{1/2} + \cos\theta \right\}^2}{\left[ 1 - \left( \frac{M_1}{M_2} \sin\theta \right)^2 \right]^{1/2}} \tag{4.3}$$

In the limit as $\theta \rightarrow 180°$,

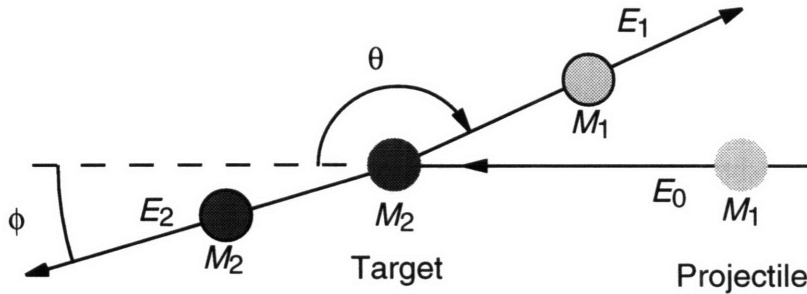


Figure 4.4 Schematic representation of an elastic collision between a projectile (of mass $M_1$, velocity $v_1$ and energy $E_0$) and a target mass $M_2$ initially at rest. Following collision, the projectile and target have velocities and energies $v_1$, $E_1$ and $v_2$, $E_2$ respectively.

| | Z | M | K | $E_1$ (keV) | $\sigma \times 10^{24}$ (cm$^2$ / steradian) |
|---|---|---|---|---|---|
| Nitrogen | 7 | 14.0 | 0.3086 | 2494 | 0.054 |
| Oxygen | 8 | 16.0 | 0.3597 | 7194 | 0.073 |
| Silicon | 7 | 28.1 | 0.5632 | 1126 | 0.248 |
| Germanium | 32 | 72.6 | 0.8020 | 1604 | 1.319 |
| Platinum | 78 | 195.1 | 0.9212 | 1842 | 7.875 |
| Gold | 79 | 197.0 | 0.9219 | 1844 | 8.080 |

Table 4.1 RBS parameters for selected elements using 2 MeV $He^{2+}$ projectiles with a backscattering angle of 180°. All values were calculated using average atomic masses based on the natural isotopic distributions of the respective elements.

$$\sigma = \left(\frac{Z_1 Z_2 e^2}{4E_0}\right)^2 \left(1 - \left(\frac{M_1}{M_2}\right)^2\right)^2 \tag{4.4}$$

From Equations 4.1–4.4, we see that for a given projectile, RBS has better resolution for lighter elements but is more sensitive to heavier elements. For example, the average kinematic scattering factors, K, and scattering cross-sections for some elements are shown in Table 4.1, for a 2 MeV $He^{2+}$ projectile and a scattering angle of 180°.

In a backscattering spectrum, N and O peaks are separated by 55 eV while Pt and Au are only separated by 0.4 eV even though the Z difference is 1 in both pairs. The backscattering yield for Au, however , is two orders of magnitude larger than for N, making RBS much more sensitive to Au than to N.

Another important phenomenon observed in RBS spectra is the energy loss of incoming and outgoing projectiles as they traverse the target. As the particles penetrate into a material, they interact with electrons in the material and slow down, losing kinetic energy. The energy loss per unit path length, $dE/dx$, depends on the identity of the particle, the density and composition of the target, and on the particle energy itself. The stopping cross-section, $\epsilon$, is defined as

$$\epsilon \equiv \frac{1}{N}\frac{dE}{dx}$$

where $N$ is the atomic density of the target material. Compilations of $^4$He stopping cross-sections are given by Chu, Mayer and Nicolet[11] and by Ziegler[14]. The target composition as a function of depth can thus be extracted

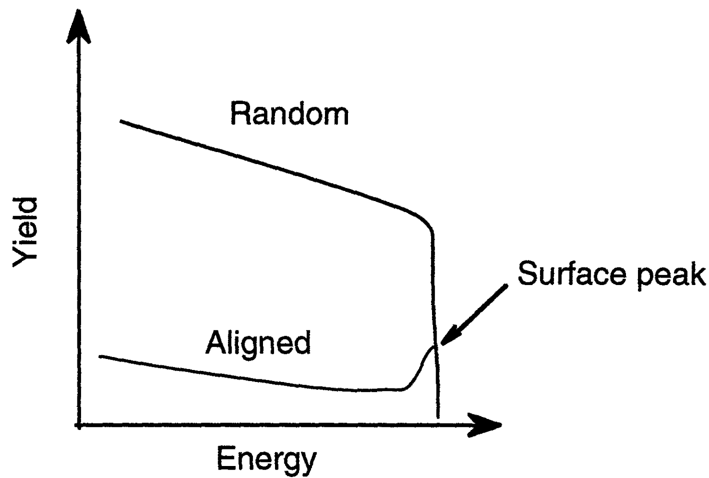


Figure 4.5 Schematic representation of channelling effects when a major axis or plane of a single crystal is aligned along the ion beam. The surface peak is due to scattering from the outermost layer of atoms.

by considering energy loss and scattering cross-sections in the interpretation of an RBS spectrum.

Finally, channelling refers to the reduction in backscattering yield observed when the ion beam is aligned along a major crystalline axis or plane of a single crystal target. The collective repulsive potential due to the string of atoms or plane of atoms can "steer" the ion beam along the strings or between the planes so that the scattering probability is substantially reduced. This is shown in Figure 4.5, which also shows a surface peak in the aligned spectrum. The surface peak is due to scattering from the outermost atoms, which are still visible to the ion beam even when the crystal is perfectly aligned.†

Ge:Si composites were analyzed using 2 MeV $He^+$ ions generated by the General Ionics model 4117 accelerator at the Harvard University Materials Research Laboratory. Random and aligned RBS spectra for Ge nanoclusters deposited on a (100) Si wafer are shown in Figure 4.6. The backscattering yield

---

† The surface peak also contains contributions from surface films, surface disorder, and underlying atoms (thermal vibration makes the underlying atoms visible to the ion beam even in an ideal crystal).

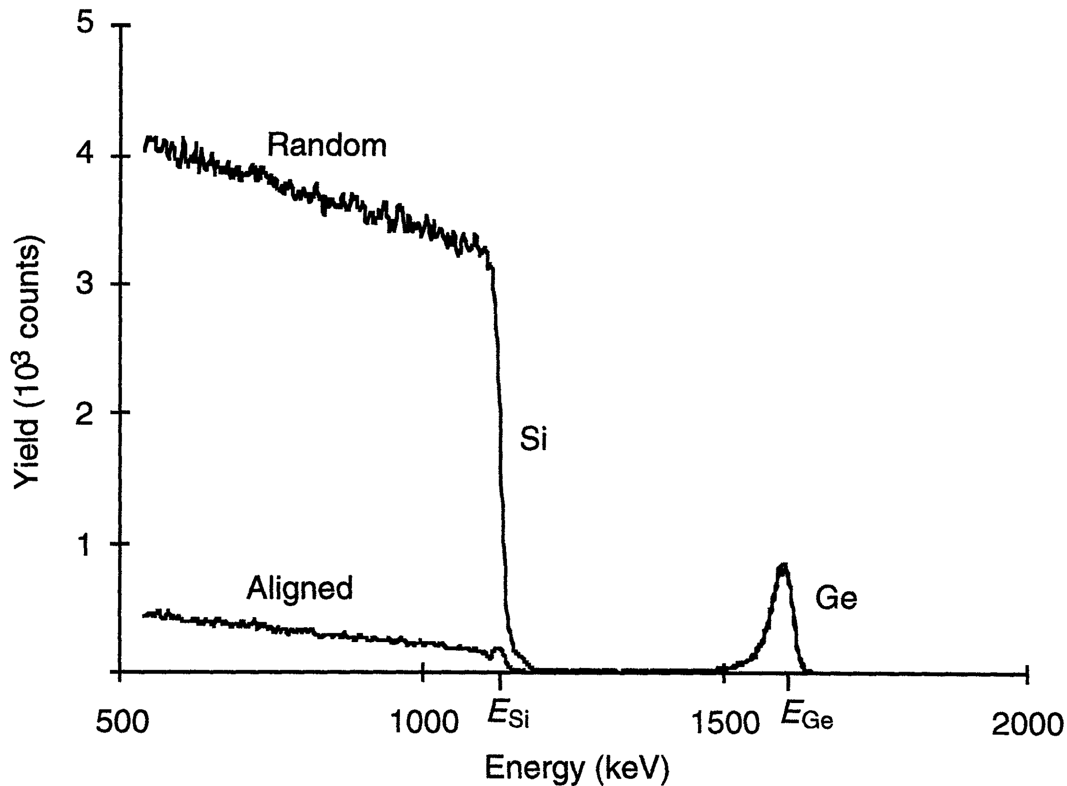


Figure 4.6 Random and aligned 2 MeV $He^+$ RBS spectra for Ge nanoclusters deposited on a Si(100) wafer without a codeposited Si host matrix. Theoretical peak locations for Si and Ge on the surface are indicated by $E_{Si}$ and $E_{Ge}$ respectively.

for Si just behind the surface peak in the aligned spectrum is 30 times smaller than the yield in the random spectrum. The Ge peak does not change, however, because the Ge nanoclusters are either amorphous, or if they are crystalline, the crystals are not aligned with the Si substrate. As mentioned previously, the Ge nanoclusters have a very wide particle distribution, so the deposited Ge film is non-uniform in thickness. This give rise to the assymetrical Ge peak, with a pronounced tail towards low energy.

Analysis of the spectrum with the RBS simulation program, RUMP,[15] yields a Ge areal density of 1.3 x $10^{16}$ $cm^{-2}$ (1.5 $\mu g/cm^2$). This implies a deposition rate of 76 $ng/cm^2$ hr. While the energy scale of the RBS detector was calibrated by use of a standard consisting of a thin Au film on Si, no correction was applied to the integrated charge measured by the detector.

Since the amount of Ge present is estimated from the area under the Ge peak, this estimate should be treated with caution.

The Ge deposition rate can also be estimated by scaling the Ge deposition rate measured in the primary chamber with a piezoelectric quartz crystal microbalance (150 $ng/cm^2$ hr at 24 cm from the PLA-SSE cluster source). Applying the inverse-square law, a deposition rate of 46 $ng/cm^2$ hr would be expected at the substrate-holder location, 43 cm from the PLA-SSE cluster source. This is within a factor of 2 of the estimate derived from RBS.

RBS spectra for two Ge:Si composites are shown in Figure 4.7, along with simulated spectra for Ge:Si films above a Si substrate. Curve (a) is for a Ge:Si composite deposited at 730°C for 3 hours (designated as sample 4-705) and curve (b) is for a film deposited at 700°C for 8 hours (sample 4-310). Backscattering energies for Si and Ge at the surface are shown by dotted lines.

Both spectra are channelled, so backscattering from the single crystal substrate is suppressed, leaving plateaus to the low energy sides of the Si peak locations. These plateaus indicate the presence of a polycrystalline or amorphous Si layer above the (100) Si wafer.

Note that the Ge peaks in curves (a) and (b) are slightly displaced to lower energies from the theoretical Ge surface peak location. This indicates that the Ge is actually located beneath the surface of the samples. The spectrum for sample 4-310, curve (b), is reasonably well matched by curve (c), the RUMP-simulated spectrum for a film consisting of an upper layer of 50 nm of Si, followed by 550 nm of $Ge_{0.008}Si_{0.992}$ on top of a Si substrate.† For comparison, curve (d) shows the simulated spectrum for 600 nm of $Ge_{0.008}Si_{0.992}$ on a Si substrate. Ge is present at the surface in this case, so the high-energy shoulder of the simulated Ge peak is at the theoretical Ge surface peak energy.

The PLA-SSE cluster source occasionally clogs up during a run, so in some cases, Ge cluster production may cease while Si CVD continues, leading to the deposition of a Si fim without any Ge in the later stages of a run. The displacement of the Ge peak was observed in all Ge:Si composites analyzed by RBS, however, so the formation of a Si cap may be inherent in the PLA-CVD process.

---

† The Si(100) substrate was in fact not included in the simulations, as RUMP does not compute channelling effects. This is equivalent to setting the yield from the substrate to zero and does not affect the simulated spectrum for layers above the substrate.

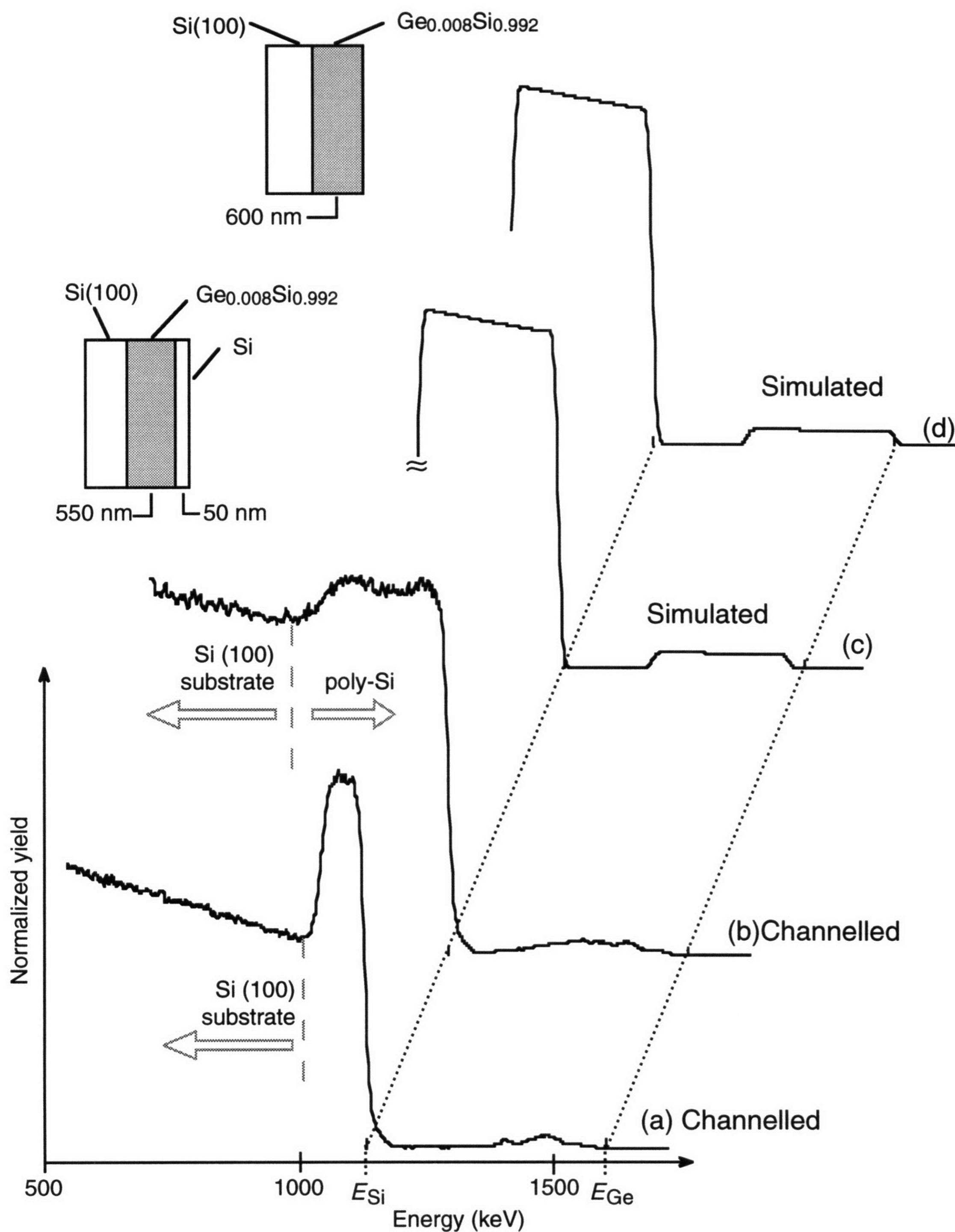


Figure 4.7 Experimental and simulated RBS spectra for Ge:Si composites. Channelled spectra for Ge:Si composites deposited (a) at 730°C for 3 hours, and (b) at 700°C for 8 hours. Simulated spectra for $Ge_{0.008}Si_{0.992}$ films (c) with a Si capping layer, (d) without a Si cap.

At the end of a deposition run, the secondary chamber is flushed with $N_2$ and the cryotrap warmed up to release the $Si_2H_6$ that condensed in the cryotrap. The cryotrap is not isolated from the secondary chamber at this time, however, and the sample, which is still in the chamber, is exposed to possibly large concentrations of $Si_2H_6$. The sample also may not have completely cooled down to room temperature yet, so some Si may be deposited on top of the Ge:Si composite during the flushing procedure at the end of a run.

### 4.4.2 X-ray diffraction

The X-ray diffraction spectrum of a Ge:Si composite grown at 700°C is shown in Figure 4.8. The peak at $2\theta = 33.0°$ is the 800 reflection from Si (100) planes in the substrate. In addition, three more Si peaks are observed, with positions and relative intensities consistent with reflection from the the Si (111), (220) and (311) planes (JCPDS card 27-1402.)[16] These arise from the codeposited Ge:Si composite and indicate that the CVD-grown Si host is polycrystalline rather than amorphous or epitaxial with the single crystal substrate.
No Ge peaks are observed in the XRD spectrum. This is primarily because of the very low concentration of Ge in the deposited film (< 1 atom %). Also, well-defined Ge peaks would only be observed from Ge particles larger than approximately 0.1 μm in diameter (Section 2.4.1). Below that size, peak broadening takes place and the already weak Ge signal cannot be distinguished from the background.

A small shift of 0.2° towards higher diffraction angles was observed for the (311) peak and is either an experimental artifact or a result of strain in the deposited composite. This is not indicative of alloying between Ge and Si as the lattice constant of Si-Ge alloys is larger than that of Si so the diffraction angle would be expected to decrease rather than increase if alloying had taken place.

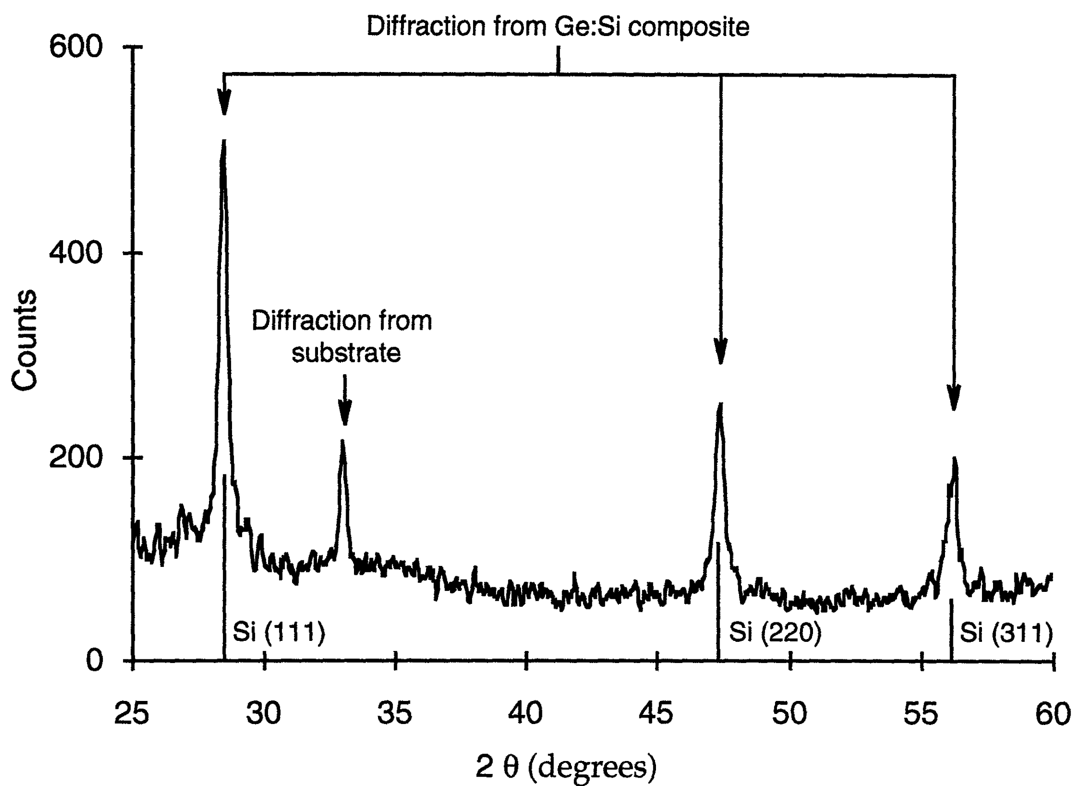


Figure 4.8 X-ray diffraction spectrum of Ge:Si composite deposited at 700°C. Bars indicate the position andrelative intensity of diffraction peaks from diamond cubic Si (JCPDS card 27-1402). Additionally there is an 800 reflection from the Si (100) substrate at 33.0°

## 4.4 Microanalysis

### 4.4.1 Electron Microscopy

Thin samples for examination in a Scanning Transmission Electron Microscope (STEM) and Transmission Electron Microscope (TEM) were prepared by direct deposition of Ge:Si composites on amorphous carbon-coated Ni TEM grids.The deposition temperature was limited to 500°C to prevent destruction of the grids, and the deposition time limited to 1–2 hours to ensure that the films were thin enough to be transparent in the electron microscope.

Element maps were collected by Energy-dispersive X-ray Spectroscopy (EDS) in the MIT CMSE 250 kV VG HB 603 STEM, i.e., by monitoring the characteristic X-ray emission as the electron beam was rastered across the sample. The annular dark field image is shown in Figure 4.9 (a) while the Ge $K\alpha$ and Si $K\alpha$ X-ray maps are shown in Figure 4.9 (b) and (c) respectively. The element maps indicate that Ge is localized in 2–4 nm particles, whereas Si is distributed more uniformly over the sample. In comparing the Si and Ge element maps, the Si concentration is seen to be enhanced by the presence of Ge. This enhancement may be explained by the Ge-catalyzed deposition of Si, which results in Si being preferentially deposited on Ge clusters. At the microscale, we thus see evidence of Ge-enhanced Si growth, even though at the macroscale, the concentration of Ge is too low to have an appreciable effect on the overall film growth rate (Section 4.2).

Figure 4.10 shows a high resolution TEM image of the same sample, taken on a 200 kV Akashi EM 002B instrument. Lattice fringes with a spacing of 3.3 Å are visible, in reasonable agreement with the Ge (111) spacing of 3.27 Å (JCPDS Card 4-545).[16] Taken together, Figures 4.9 and 4.10 suggest that Ge nanocrystals surrounded by a Si shell are present in the Ge:Si composite.

Thermodynamic calculations by Balasubramaniam[17] have shown that for Ge nanocrystallites within a Si shell, dislocations are not introduced, despite the difference in Si and Ge bulk lattice parameters, until the Ge crystallite exceeds 20 nm in diameter, regardless of Si shell thickness.

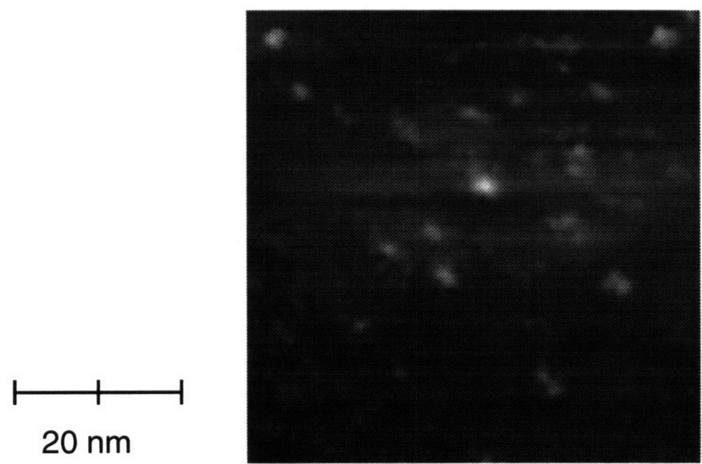


(a) Annular dark field image

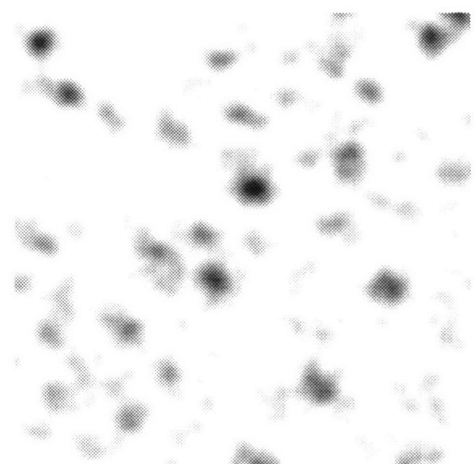

(b) Ge element map

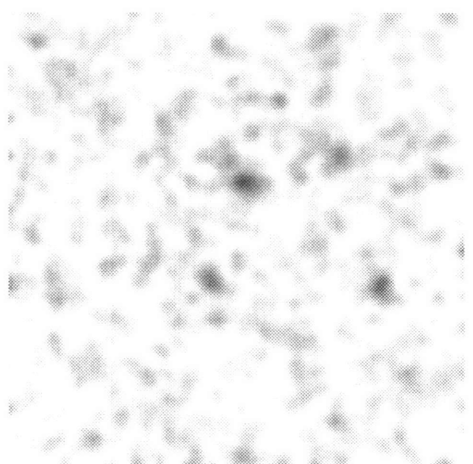

(c) Si element map

Figure 4.9 STEM images of Ge:Si composite deposited at 500°C on C-coated TEM grid: (a) Annular dark field image; (b) Ge element map; (c) Si element map. The Ge and Si element maps were collected by EDS and represent the same region shown in part (a). Regions of higher Ge or Si density appear darker in parts (b) and (c) respectively.

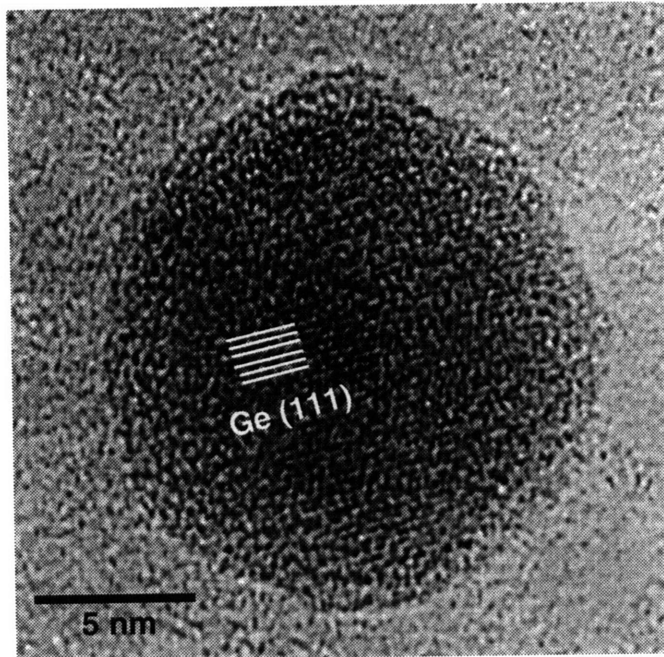


Figure 4.10 High Resolution Transmission Electron Microscope image of Ge:Si composite grown at 500°C on a C-coated TEM grid. Ge (111) lattice fringes are visible with a spacing of 3.3 Å.

In a TEM image such as Figure 4.10, then, it is not possible to precisely locate the boundary between Ge and Si, if the Si shell grows epitaxially around the Ge crystallite without introducing any dislocations at the interface.

An alternative interpretation of the STEM and TEM data is that the nanoparticles seen in fact consist of $Si_xGe_{1-x}$ alloys, possibly with some radial concentration gradient. The lattice constant of $Si_xGe_{1-x}$ alloys is intermediate between that of Ge and Si, varying roughly linearly with Ge content.[18] No calibration checks were performed on the TEM at the time that the images were taken, so I cannot determine the error bounds for the lattice spacing determined from the diffraction fringes shown in Figure 4.9 It is possible that the nanocrystal shown is in fact a $Si_xGe_{1-x}$ alloy nanocrystal. The STEM element maps of Figure 4.9 are also unable to distinguish discrete Ge particles within a Si shell from interdiffused $Si_xGe_{1-x}$ particles.

Sharpness of the Ge-Si interface is even more of an issue for composites deposited at higher temperatures because of the increase in diffusivity with temperature. The Ge nanocrystals codeposited into Ge:Si composites deposited at 700–800°C, such as those used for RBS analysis and PL measurements, may interdiffuse to the extent that they become Ge-rich zones in a $Si_xGe_{1-x}$ alloy, or even a homogeneous alloy, rather than Ge quantum dots within a Si host.

## 4.5 Photoluminescence

In the case of Si, both surface passivation and quantum confinement have been shown to be necessary conditions for photoluminescence from Si nanocrystals (see Sections 1.2.3 and 2.4) PL spectroscopy could therefore be used as an indirect probe of the Ge-Si interface in Ge:Si composites, as PL would only be observed if the interface is substantially free of dangling bonds and defects.

No visible emission was observed from any Ge:Si composites excited by a handheld ultraviolet Hg lamp or by a tripled Nd:YAG (355 nm) laser. This is consistent with the absence of visible photoluminescence from PLA-SSE Ge nanoclusters deposited without a Si matrix but in contrast to published reports of visible blue photoluminescence from Ge quantum dots.[19-22] and Takagahara's[23] prediction of quantum confinement effects in Ge nanoclusters. This lack of photoluminescence may be due to poor surface passivation of the Ge nanoclusters embedded in the Si host matrix. Defects at the Si-Ge interface may thus be providing non-radiative pathways for excition recombination and suppressing light emission. Alternatively, the magnitude of the quantum confinement effect may be smaller in Ge than in Si either because the average size of PLA-SSE synthesized Ge nanoclusters is larger than that of Si, or because Takagahara's model overpredicts the magnitude of the quantum confinement effects.

Near infra-red PL spectra were measured by exciting the samples with a mechanically chopped 488 nm $Ar^+$ continuous wave laser and collecting the emission with a 0.75 m monochromator and a liquid $N_2$-cooled Ge photodetector. The sample was cooled to ~4 K in a cryostat cooled with liquid helium.

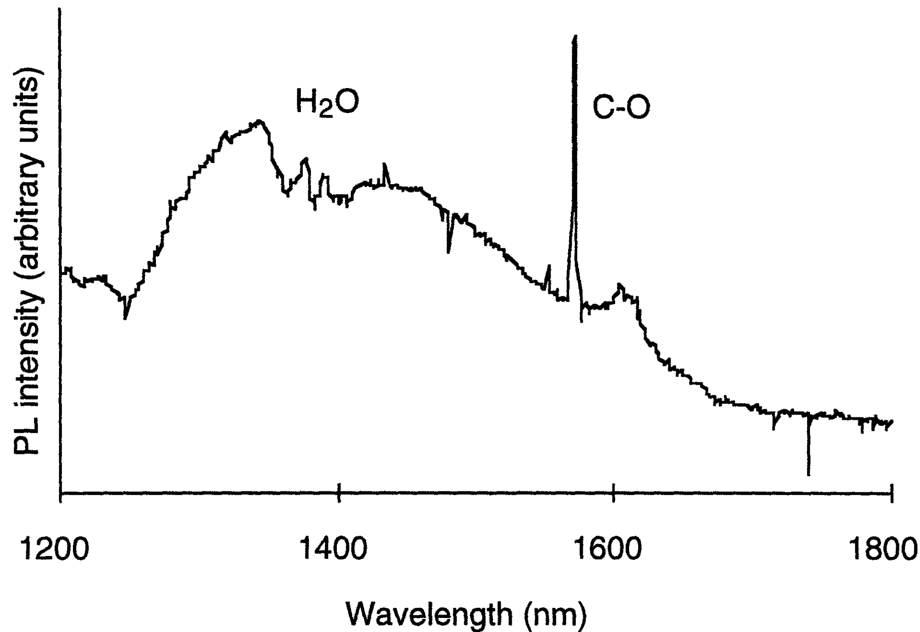


Figure 4.11 Near infrared photoluminescence spectrum for Ge:Si composite analyzed by RBS prior to PL spectroscopy. The PL behaviour shown is due to radiation-induced centers created by irradiation of the sample with $He^+$ ions during RBS analysis. Ge:Si composites which were not analyzed by RBS do not exhibit any photoluminescence.

No infra-red PL was observed from as-deposited Ge:Si composites, either. Broad PL peaks such as that shown in Figure 4.11 were only observed in samples that had been analyzed by RBS prior to PL measurement. The peak at 1.57 µm is due to C-O pairs, and the features around 1.37 µm are due to $H_2O$ impurities in the film. These luminescence centers are radiation-induced, and were created by irradiating the sample with 2 MeV $He^+$ ions during RBS analysis. Samples which were not irradiated, i.e., not analyzed by RBS, did not show this PL behavior.

It may be argued that the infrared PL is in fact from Ge nanoclusters, but that Ge nanoclusters in PLA-SSE Ge:Si composites are larger than those synthesized by annealing Si-Ge oxides to precipitate Ge nanocrystals.[19,20,24,25] The wavelength of emisssion from Ge:Si composites would then be longer

than that from Ge nanocrystals in Si-Ge oxides. The reported luminescence spectra for annealed Si-Ge oxides are very similar to those of defects in $SiO_2$ glass,however, so the luminescence observed is more likely due to $SiO_2$ than to Ge quantum dots. PL has also not been reported from Ge nanocrystals synthesized by an inorganic solution-phase technique.[26,27]

It is therefore unlikely that the PL behavior seen in Figure 4.11 is due to quantum confinement in PLA-SSE Ge nanoclusters embedded in the Si host. Whereas PL due to quantum confinement is seen for Si nanoclusters, no PL is seen for Ge nanoclusters. Bulk Ge has a higher interface trap density than Si, and the same may be true at nanometer scale. Excitons in Ge nanocrystals would therefore recombine at surface sites without emitting a photon, and radiative recombinations would be suppressed. Theoretical predictions[23] of quantum confinement effects in Ge may also be overstated, and the PL behaviour of nanocrystalline Ge may in fact be identical to that of bulk Ge.

The Ge:Si composites used for PL spectroscopy were all deposited above 700 °C. At these temperatures, interdiffusion of Ge and Si is more likely to take place than in the composites analyzed by STEM and TEM, which were deposited at lower temperature. The high temperature Ge:Si composites may therefore consist of $Si_xGe_{1-x}$ alloys with some Ge-rich zones, or even completely homogeneous alloys.

In the electron microscope data of the previous section, Si deposition was seen to be enhanced by the presence of Ge because of enhanced hydride desorption from Ge compared to Si (see Section 3.1.2 for a discussion of the mechanism of Si deposition from $Si_2H_6$) Hydride desorption is only limiting at low temperatures, however, so Ge-enhancement would only be observed at low temperatures. At higher temperatures, where growth is adsorption-limited, Ge in fact has a deleterious effect on the growth rate because of the lower sticking probability of $Si_2H_6$ on Ge compared to Si.[28-30] Enhanced Si deposition resulting in the growth of a passivating Si shell around the Ge nanoclusters may therefore not occur in Ge:Si composites used for PL measurements (deposited above 700°C).

On balance, therefore, the infrared PL observed is due to radiation-induced centers created during RBS analysis, not to Ge quantum confinement. Photoluminescence has been used as a sensitive means of detecting impurities in Si.[31] In this case, the post-RBS photoluminescence spectrum shows the presence of water, carbon and oxygen. This was confirmed by

Auger analysis, where 3–5 % each of C and O were detected in a Ge:Si composite, even after surface contaminants were removed by sputtering.

## 4.6 Summary

Ge cluster:Si host composites have been synthesized by combining PLA-SSE for production of Ge nanoclusters with chemical vapor deposition of Si from $Si_2H_6$. Electron microscopy and X-ray mapping show that the composites consist of discrete Ge particles embedded in a Si host, while RBS indicates that the overall Ge content of the deposited films is approximately one atomic percent. X-ray diffraction shows that the deposited Si matrix is polycrystalline. No visible or infra-red photoluminescence is observed from Ge:Si composites as deposited. Ion-irradiated composites exhibit PL due to C and O impurities, and Auger spectroscopy shows that these elements are present at the level of 3–5 % each.

## REFERENCES


1. J. F. O'Hanlon, *A User's Guide to Vacuum Technology* (John Wiley & Sons, New York, 1989).
2. G. Scoles, "Atomic and molecular beam methods," (Oxford University Press, New York, 1988), Vol. 1.
3. L. A. Chiu, A. A. Seraphin, and K. D. Kolenbrander, "Gas phase synthesis and processing of silicon nanocrystallites: Characterization by photoluminescence emission spectroscopy," J. Electron. Mater. **23** (3), 347 (1994).
4. T. Takahagi, I. Nagai, A. Ishitani, H. Kuroda, and Y. Nagasawa, "The formation of hydrogen-passivated silicon single-crystal surfaces using ultraviolet cleaning and HF etching," J. Appl. Phys. **64** (7), 3516 (1988).
5. B. S. Meyerson, F. J. Himpsel, and K. J. Uram, "Bistable conditions for low-temperature silicon epitaxy," Appl. Phys. Lett. **57** (10), 1034 (1990).
6. M. Niwano, J. Kageyama, K. Kurita, K. Kinashi, I. Takashashi, and N. Miyamoto, "Infrared spectroscopy study of initial stages of oxidation of hydrogen-terminated Si surfaces stored in air," J. Appl. Phys. **76** (4), 2157 (1994).
7. B. S. Meyerson, E. Ganin, D. A. Smith, and T. N. Nguyen, "Low temperature silicon epitaxy by hot wall ultrahigh vacuum/low pressure chemical vapor deposition techniques: surface optimization," J. Electrochem. Soc. **133** (6), 1232 (1986).
8. L.-Q. Xia, M. E. Jones, N. Malty, and J. R. Engstrom, "Dissociation and pyrolysis of $Si_2H_6$ on Si surfaces: The influence of surface structure and adlayer composition," J. Chem. Phys. **103** (4), 1691 (1995).
9. R. J. Buss, P. Ho, W. G. Breiland, and M. E. Coltrin, "Reactive sticking coefficients for silane and disilane on polycrystalline silicon," J. Appl. Phys. **63** (8), 2808 (1988).
10. E. Rutherford, "The scattering of $\alpha$ and $\beta$ particles by matter and the structrure of the atom," in *The collected papers of Lord Rutherford of Nelson*, edited by J. Chadwick (Interscience Publishers, Inc., New York, 1963), Vol. 2, pp. 238.
11. W.-K. Chu, J. W. Meyer, and M. A. Nicolet, *Backscattering Spectrometry* (Academic Press, New York, 1978).

12. L. C. Feldman and J. W. Mayer, *Fundamentals of surface and thin film analysis* (Elsevier Science Publishing Co., Inc., New York, 1986).
13. T. G. Finstad and W. K. Chu, "Rutherford Backscattering Spectrometry on Thin Solid Films," in *Analytical Techniques for Thin Films*, edited by K. N. Tu and R. Rosenberg (Academic Press, San Diego, 1988), p. 392.
14. J. F. Ziegler, *Helium: Stopping powers and ranges in all elemental matter* (Pergamon Press, New York, 1978).
15. L. R. Doolittle, "Algorithms for the rapid simulation of Rutherford Backscattering Spectra," Nucl. Instrum. Meth. Phys. Res. B **9**, 344 (1985).
16. Joint Committee on Powder Diffraction Standards, *Powder diffraction file* (JCPDS International Centre for Diffraction Data, Swarthmore, Pa., ).
17. S. Balasubramaniam, G. Ceder, and K. D. Kolenbrander, "Three-dimensional epitaxy: Thermodynamic stability range of coherent Germanium nanocrystallites in silicon," (unpublished) (1995).
18. E. A. Fitzgerald, "GeSi/Si nanostructures," Annu. Rev. Mater. Sci. **25**, 417 (1995).
19. Y. Maeda, N. Tsukamoto, Y. Yazawa, Y. Kanemitsu, and Y. Masumoto, "Visible photoluminescence of Ge microcrystals embedded in $SiO_2$ glassy matrices," **59**, 3168 (1991).
20. Y. Kanemitsu, H. Uto, Y. Masumoto, and Y. Maeda, "On the origin of visible photoluminescence in nanometer-size Ge crystallites," Appl. Phys. Lett. **61**, 2187 (1992).
21. J. Jiang, K. Chen, X. Huang, D. Feng, and D. Sun, "A novel Ge nanostructure exhibiting visible photoluminescence," Chin. Phys. Lett. **10** (10), 630 (1993).
22. D. C. Paine, C. Caragianis, T. Y. Kim, Y. Shigesato, and T. Ishara, "Visible photluminescence from nanocrystalline Ge formed by H2 reduction of $Si_{0.6}Ge_{0.4}O_2$," Appl. Phys. Lett. **62** (22), 2842 (1993).
23. T. Takagahara and K. Takeda, "Theory of the quantum confinement effect on excitons in quantum dots of indirect-gap materials," Phys. Rev. B **46** (23), 15578 (1992).
24. Y. Maeda, "Visible photoluminescence fron nanocrystallite Ge embedded in a glassy $SiO_2$ matrix: Evidence in support of the quantum-confinement mechanism," Phys. Rev. B **51** (3), 1658 (1995).
25. K. V. Shcheglov, C. M. Yang, K. J. Vahala, and H. A. Atwater, "Electroluminescence and photoluminescence of Ge-implanted $Si/SiO_2/Si$ structures," Appl. Phys. Lett. **66** (6), 745 (1995).
26. J. R. Heath and F. K. LeGoues, "A liquid solution synthesis of single crystal germanium quantum wires," Chem. Phys. Lett. **208** (3,4), 263 (1993).
27. J. R. Heath, J. J. Shiang, and A. P. Alivisatos, "Germanium quantum dots: optical properties and synthesis," J. Chem. Phys. **101** (2), 1607 (1994).
28. D. J. Robbins, J. L. Glasper, A. G. Cullis, and W. Y. Leong, "A model for heterogeneous growth of $Si_{1-x}Ge_x$ films from hydrides," J. Appl. Phys. **69** (6), 3729 (1991).
29. D. J. Tweet, T. Tatsumi, H. Hirayama, K. Miyanga, and K. Terashima, "Factors determining the composition of strained germanium-silicon layers grown with disilane and germane," Appl. Phys. Lett. **65** (20), 2579 (1994).
30. B. M. H. Ning and J. E. Crowell, "Investigation on the growth rate enhancement by Ge during SiGe alloy deposition by chemical vapor deposition," Appl. Phys. Lett. **60** (23), 2914 (1992).
31. G. Davies, "The optical properties of luminescence centres in silicon," Phys. Rep. **176** (3-4), 83 (1989).

# Chapter 5
# Si Nanocluster:Silicon Oxide Host Composites

$Si:SiO_x$ cluster:host composites were deposited by depositing PLA-SSE Si nanoclusters into $SiO_x$ films produced by laser evaporating Si in the presence of $O_2$. The direct oxidation of $Si_2H_6$ by $O_2$ was investigated as an option for depositing silicon oxide films, but rejected because of the very low growth rates achieved. $SiO_x$ films deposited by laser evaporation were analyzed by RBS and found to be oxygen-deficient relative to $SiO_2$. X-ray Photoelectron Spectroscopy and X-ray Diffraction demonstrated that $SiO_x$ films deposited without PLA-SSE Si nanoclusters also contained large Si particles. These particles were identified as artifacts of laser evaporation by their morphology as revealed by Scanning Electron Microscopy. $SiO_x$ films codeposited with PLA-SSE clusters were indistiguishable from those deposited without clusters, under all the analysis techniques applied. $Si:SiO_x$ composites did not exhibit photoluminescence even though Si nanoclusters deposited without a matrix photoluminescence in the visible regime. This is attributed to poor surface passivation of the Si nanoclusters in $Si:SiO_x$ composites.

## 5.1 Silica deposition by oxidation of disilane

The disilane CVD system was modified to deposit $SiO_2$ using the direct reaction of $Si_2H_6$ and $O_2$. A $^1/_{16}$" stainless steel tube was added to the secondary chamber for use as an oxygen doser and directed towards the substrate heater in a fashion similar to the disilane doser described in Section 4.1 Oxygen (99.995 %) and disilane were simultaneously admitted into the codeposition chamber while a Si wafer substrate was heated to 800°C. The disilane partial pressure during deposition was $10^{-5}$ torr and the oxygen pressure $5 \times 10^{-4}$ torr.

Kinetic parameters for the reaction of $Si_2H_6$ with $O_2$ at atmospheric pressure were extracted from growth rate data reported by Mishima et al.[1]: the reaction probability of $Si_2H_6$ was $10^{-5}$ at 300 °C with an activation energy of 22 kcal $^{-1}K^{-1}$ (Section 3.2.2) Assuming that the reaction mechanism and rate constants remain unchanged despite extrapolation to higher temperature and lower pressure, the reaction probability at 800 °C is $10^{-3}$, corresponding to a

$SiO_2$ growth rate of 110 Å/hr. This agrees well with the $SiO_2$ deposition rate of 150 Å/hr measured in my system.

Note that there is a sharp downturn in the silica deposition rate shown in Figure 3.1 above 300°C. This is because under the atmospheric pressure conditions used by Mishima et al., the reactants are heated by convection and react with each other in the gas-phase before they can reach the surface. Under the vacuum conditions of the secondary chamber, however, no gas-phase reactions occur even when the substrate is heated to higher temperatures, both because of the low probability of gas-phase collisions and the absence of convective preheating.

The $SiO_2$ deposition rate was constrained by the low pressure in the secondary chamber. As in the case of Si deposition, the chamber pressure could not be raised because of the operating limits of the PLA-SSE process. The primary chamber operating pressure has to be lower than ~ $10^{-4}$ torr to prevent flooding of the diffusion pump and the secondary chamber has to be at an even lower pressure to prevent backflow of $Si_2H_6$ into the primary chamber. The deposition of $SiO_2$ by direct oxidation of $Si_2H_6$ in the secondary chamber was therefore deemed infeasible because of the very low $SiO_2$ deposition rate.

## 5.2 Reactive Laser Evaporation

As an alternative to the $Si_2H_6$ oxidation process, a reactive laser evaporation process was adopted, where Si was evaporated by laser oxidation and reacted with $O_2$ in the primary chamber. This also allows us to make use of the higher nanocluster flux in the primary chamber because of the reduced distance between the substrate and the PLA-SSE cluster source.

The ablation laser beam was split as shown in Figure 5.1 with the transmitted beam continuing to the PLA-SSE cluster source and the reflected beam directed towards another rotating Si rod in the primary chamber. The ratio of reflected to transmitted beam energies was approximately 1:3. Similar to the cluster rod, the second matrix rod was mounted on a screw driven by a DC motor. Unlike the cluster rod in the PLA-SSE source, there was no confinement of the ablated material in a channel or any He expansion.

A $^1/_{16}$" stainless steel doser was directed towards the substrate and $O_2$ leaked in though a leak valve. Si is thus evaporated from the second Si rod

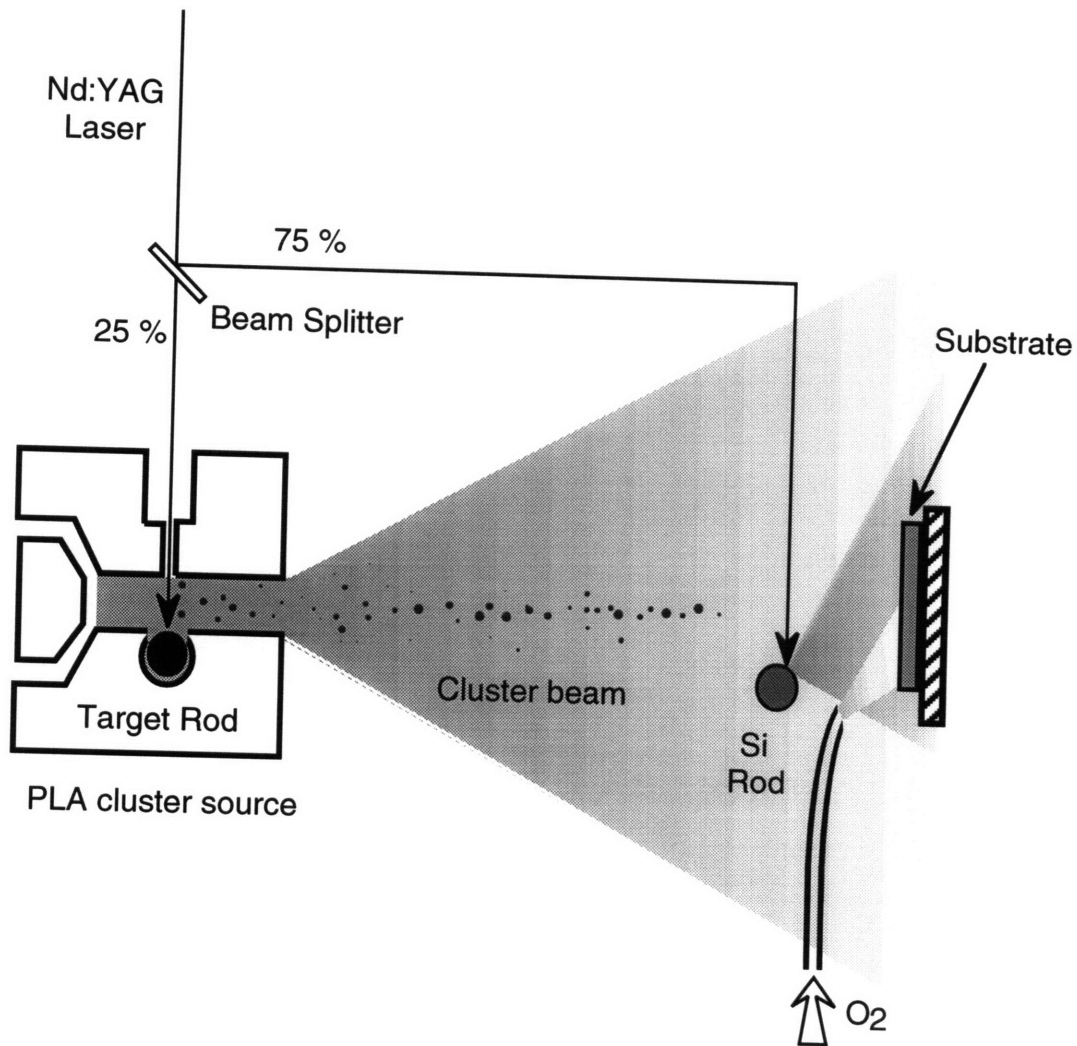


Figure 5.1 Double laser ablation and oxidation. The Nd:YAG laser beam is split into two beams with one beam (25% of the original beam energy) used for PLA-SSE cluster production and another (75 %) used to laser evaporate a second Si rod placed close to the substrate. Oxygen gas is introduced through a doser and oxidizes the ablated Si to form a silicon oxide film.

and reacted with $O_2$ to deposit a silicon oxide film on the substrate. Si:$SiO_x$ composites are then synthesized by simultaneously depositing PLA-SSE Si clusters and a silicon oxide film generated by reactive laser evaporation.

### 5.2.1 Minimum oxygen flux for complete oxidation

Laser evaporated Si species (atoms, ions, clusters etc.) from the matrix rod are continually arriving at the substrate surface so the kinetics of oxide formation have to be considered in addition to the thermodynamic aspects of active and passive oxidation discussed in Section 3.2.4 The Si flux to the substrate was measured with a quartz crystal monitor, and the oxygen pressure at the substrate measured with a Fast Ionization Gauge (FIG) and a thermocouple gauge. The minimum oxygen flux required to completely oxidize Si arriving at the substrate was estimated from literature values for the sticking probability of molecular oxygen on Si and compared to the measured oxygen pressure.

#### 5.2.1.1 Si flux

The Si flux to the substrate as a function of laser power was measured by placing a quartz crystal monitor (QCM) sensor at the substrate location and laser evaporating the Si matrix rod (3.8 cm away from the substrate/sensor location) without introducing oxygen. The QCM measures the mass of the piezoelectric quartz crystal and the Si flux calculated from the rate of mass increase. The Si flux as a function of ablation laser power is plotted in Figure 5.2 where the laser power is measured *prior* to splitting the beam (see Figure 5.1). The power arriving at the Si matrix rod is approximately 75% that measured before splitting the beam. The transmitted beam was blocked with a beam block and PLA-SSE clusters not produced so these experiments measure only the deposition rate of Si evaporated from the Si matrix rod. The Si flux was approximately linear with laser power and at a laser power of 30 mJ/pulse was approximately 30 $\mu g/cm^2$ hr (equivalent to $2 \times 10^{14}$ $cm^{-2}$ $s^{-1}$)

Data taken on two different days are represented by filled and open circles. While the deposition rate was linear with power within each day's run, there was a large difference in deposition rate between days. The Si matrix rod is removed from the chamber between runs to accomodate other users of the PLA-SSE system, and the location of the rod relative to the substrate may

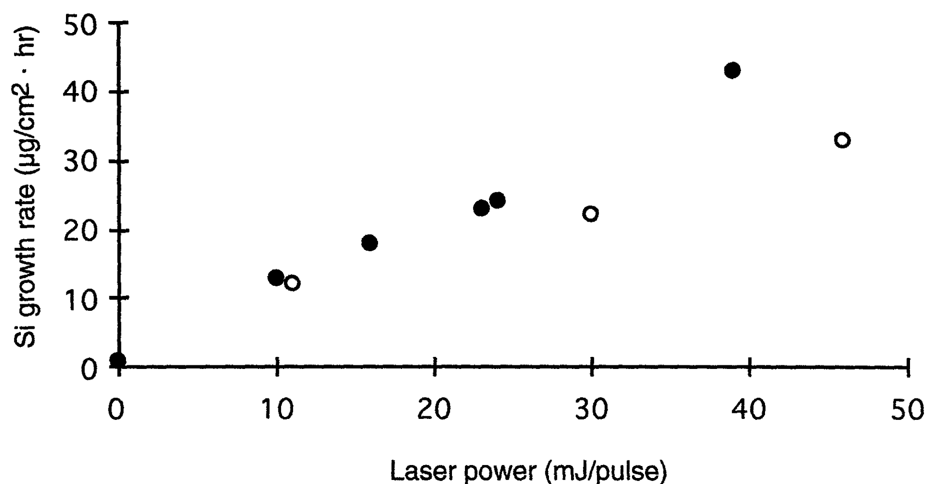


Figure 5.2 Si deposition rate as a function of laser power. The Si matrix rod was 3.8 cm away from the quartz crystal monitor sensor head. Laser power is measured before splitting the beam, and approximately 75 % of the measured beam energy is used to ablate the Si matrix rod. Filled and open circles represent data taken on two different days.

change slghtly from run to run. The point of ablation also changes slightly, and because of the strongly angular-dependent distribution of laser ablated Si, minor changes in geometry may result in large changes in deposition rate.

5.2.1.2 Oxygen flux at the substrate

$O_2$ was supplied through a $^1/_{16}$" stainless steel doser directed at the centre of the substrate and with the tip of the doser 3 cm away from the substrate. $O_2$ flow was regulated with a precision needle valve located outside the vacuum chamber feedthrough. Since the substrate was very close to the doser, the local oxygen pressure at the substrate was expected to be higher than the primary chamber background pressure measured by a Bayard-Alpert ionization gauge located at the bottom of the chamber.

The local oxygen pressure at the substrate was measured by placing a Fast Ionization Gauge (FIG)[2] or a thermal conductivity (TC) gauge at the substrate location and varying the oxygen leak rate. The Fast Ionization Gauge (FIG)

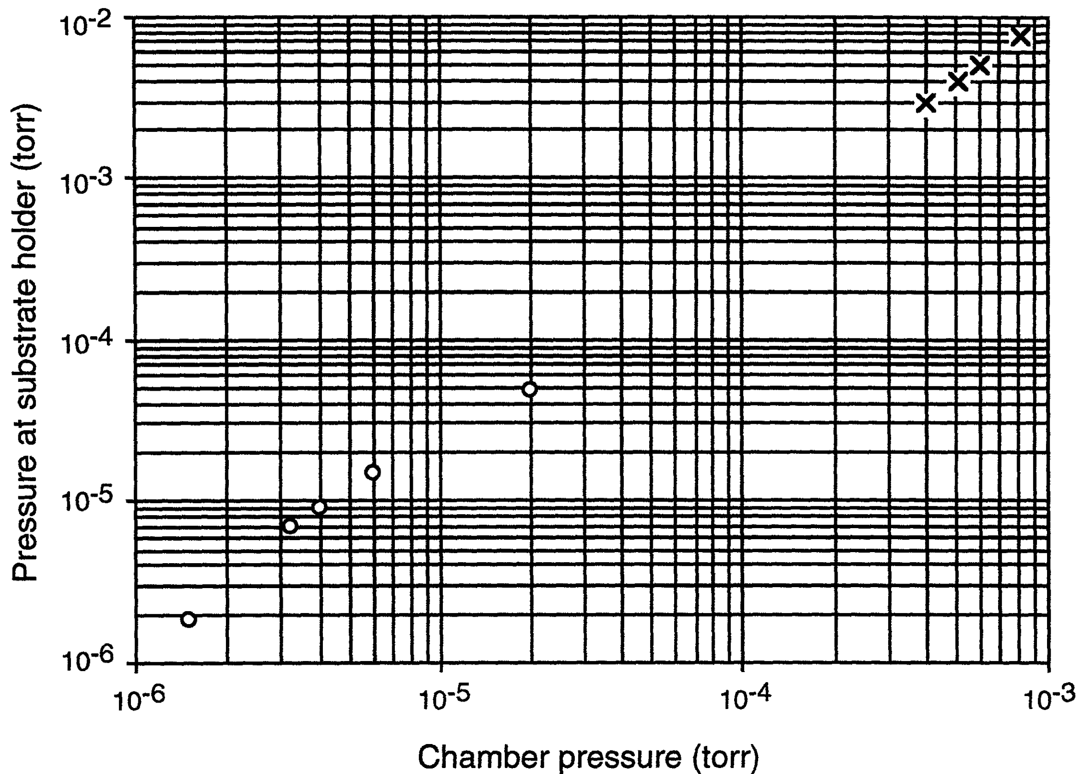


Figure 5.3 Correlation between local oxygen pressure at substrate holder and overall chamber pressure. Local oxygen pressure at the substrate holder is measured with a Fast Ionization Gauge ( o ) or a thermocouple gauge (×) while the chamber pressure is measured with an ionization gauge.

consists of a 4-cm long collector wire surrounded by a grid. The FIG averages out the recorded pressure over the length of the collector wire, and therefore underestimates the gas density at the maximum emission from the doser. To prevent the hot filament from burning out, a thermocouple gauge tube was used instead of the FIG to measure pressures above $10^{-3}$ torr.

The local oxygen pressure at the substrate is then correlated to the primary chamber pressure measured by an ionization gauge at the bottom of the chamber (Figure 5.3). The local oxygen pressure was consistently higher than the primary chamber background pressure. The highest recorded local pressure was $8 \times 10^{-3}$ torr with a chamber background pressure of $8 \times 10^{-4}$ torr. At more typical operating conditions of $1 \times 10^{-4}$ torr, the local oxygen pressure

was $5 \times 10^{-4}$ torr.

The local oxygen pressure can be increased by reducing the doser-substrate distance. With the doser right at the mouth of the TC gauge, the measured local pressure was $9 \times 10^{-2}$ torr with a chamber pressure of $2 \times 10^{-4}$ torr, compared to the $1 \times 10^{-3}$ torr that would be expected with the doser 3 cm away from the substrate holder. As the substrate gets closer to the doser, however, uniformity decreases, i.e., a higher $O_2$ pressure is observed but over a smaller area.

The reaction probability for molecular oxygen adsorption onto clean (100) Si at room temperature was measured by D'Evelyn et al.[3,4] and Hollinger and Himpsel[5] to be on the order of $10^{-3}$ to $10^{-2}$. From the QCM results of Section 5.2.1.1, about $10^{14}$ cm$^{-2}$ s$^{-1}$ Si atoms arrive at the substrate when an ablation laser power of 30 mJ/pulse is used. A lower limit on the flux of $O_2$ required to react with Si arriving at the substrate can be obtained from the initial reaction probability of $O_2$ on Si. Even if a subsequent surface reaction step is limiting, the $SiO_2$ production rate can be no higher than the initial sticking probability. Since a continuous supply of Si is arriving from the laser evaporated matrix rod, the deposited silicon oxide will be silicon-rich if the conversion of Si to $SiO_2$ is slower than the arrival rate of Si.

Assuming that the reaction probability for $O_2$ reacting with evaporated Si is close to that found by D'Evelyn et al. and Hollinger and Himpsel, a minimum oxygen flux of $10^{16}$–$10^{17}$ cm$^{-2}$ s$^{-1}$ would be required to react with the laser evaporated Si. Under typical operating conditions with an $O_2$ pressure of $10^{-4}$ torr, the $O_2$ flux at the substrate is $10^{17}$ cm$^{-2}$ s$^{-1}$. The $O_2$ flux is thus barely sufficient to keep up with the influx of evaporated Si.

This is a low estimate of the oxygen reqirement, however, because it assumes that the initial adsorption is the rate-limiting step. If a subsequent reaction step is limiting, Si will be arriving at the substrate faster than it can be oxidized to $SiO_2$. The deposited silicon oxide films would then be oxygen-deficient. The question of active and passive oxidation must also be considered (see Section 3.2.4). If SiO is formed by $Si + \frac{1}{2}O_2 \rightarrow SiO$, the SiO may volatilize before it reacts completely to $SiO_2$. This consumes $O_2$ that may otherwise be converted to $SiO_2$ and increases the $O_2$ requirement. The relative rates of active and passive oxidation are strongly temperature dependent with active oxidation (volatilization to SiO) favored at high temperature and passive oxidation (formation of solid $SiO_2$) favored at lower

temperatures. Since the ablated Si is initially very hot then cools down on impact with the substrate, the relative production of SiO and $SiO_2$ is determined by the rate of cooling of the deposited Si. Any SiO which is formed volatilizes and increases the flux of $O_2$ that would be required to ensure that stoichiometric $SiO_2$ is deposited.

For comparison, in the laser evaporation process of Fogarassy et al.,[6] the Si flux is $10^{15}$ $cm^{-2}$ $s^{-1}$. Following the analysis above, a minimum oxygen pressure of $10^{-3}$ torr would be required to completely oxidize the deposited Si. Indeed they report that stoichiometic $SiO_2$ is deposited at oxygen pressures of 0.1 torr but a substoichiometric ($O/Si \leq 1$) oxide is deposited at oxygen pressures ~ $10^{-5}$ torr.

## 5.3 Overall film stoichiomery

The stoichiometry of the silicon oxide films was measured by fitting RBS spectra collected at the Harvard Materials Research Laboratory to simulated spectra generated by the RBS simulation program, RUMP[7]. A representative unchanneled RBS spectrum from a silicon oxide film grown on Si (100) is shown in Figure 5.4 The Si matrix rod was placed 3.8 cm away from the substrate and the oxygen pressure during deposition was 5 x $10^{-4}$ torr. The PLA-SSE cluster source was not used during this experiment, so there was no additional He background pressure. The laser power was 33 mJ/pulse before splitting the beam, giving approximately 25 mJ/pulse to the matrix rod. The O/Si ratio was found to be 1.6 with a film thickness of 0.5 μm.

### 5.3.1 Factorial experiments for optimizing film stoichiometry

Preliminary experiments with the laser-evaporated silicon oxidation system indicated that the oxygen content of the deposited film increased when the the distance between the matrix rod and the substrate was reduced or when the laser power was increased. In addition, it was reasonable to believe that varying the substrate temperature would influence the degree of oxidation of the deposited film. A $2^3$ factorial experiment[8,9] was therefore performed with laser fluence, rod-substrate distance and substrate temperature as variables. The O/Si ratio varied from 1.4 to 1.8. Contrary to the preliminary findings, analysis of the full experimental results indicates that there are no main effects or interactions– none of the variables significantly

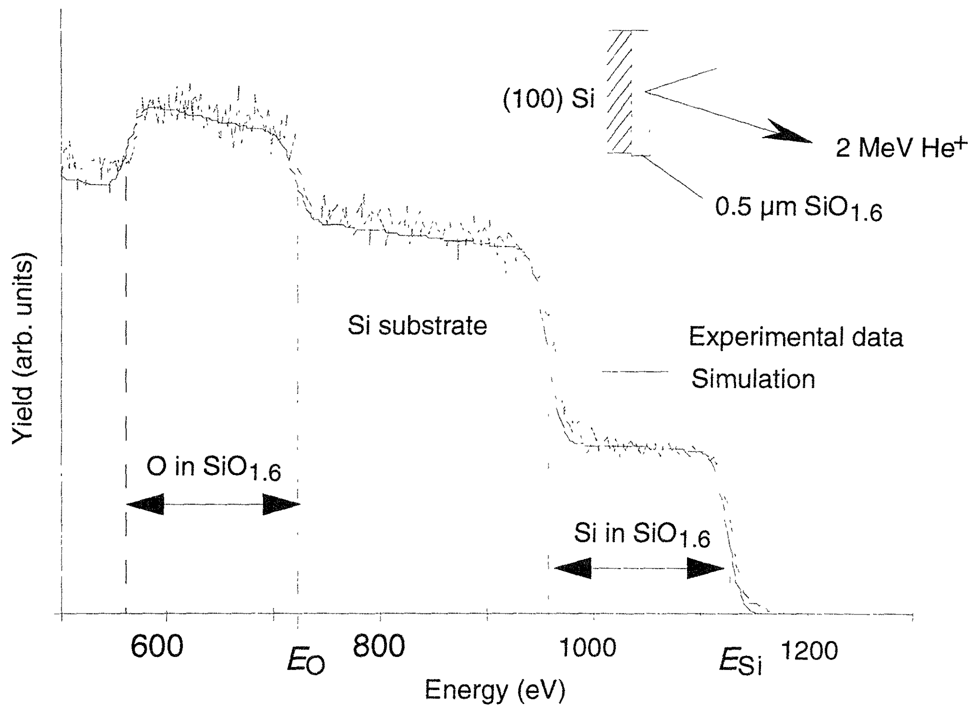


Figure 5.4 RBS spectrum of silicon oxide film deposited on (100) Si wafer. Simulated data is for a film with an O/Si ratio of 1.6 and a thickness of 0.5 µm. The film was deposited with an oxygen pressure of $5 \times 10^{-4}$ torr, a laser fluence of 33 mJ/pulse and a rod-substrate distance of 3.8 cm. $E_{Si}$ and $E_O$ represent the energy of ions backscattered from Si and O, respectively, on the surface.

affect the film stoichiometry (Figure 5.5) The standard error in the O/Si ratio as determined from three sets of two replicates was 0.22, giving a 95 % confidence interval of 0.44, which is broader than the observed range of O/Si ratios.

The large variability in the O/Si ratios arises from several sources: run-to-run variations, spatial variations in composition within a sample, errors in the RBS measurement and errors in fitting the data to a simulated spectrum.

Multiple RBS measurements were performed along a distance of approximately 1 cm on one sample and indicated that while the film thickness varied substantially, the relative heights of the O and Si peaks remained indistinguishable. The analysis area for each individual measurement was approximately 2 mm in diameter. Variation in composition within a sample is therefore relatively small, even though

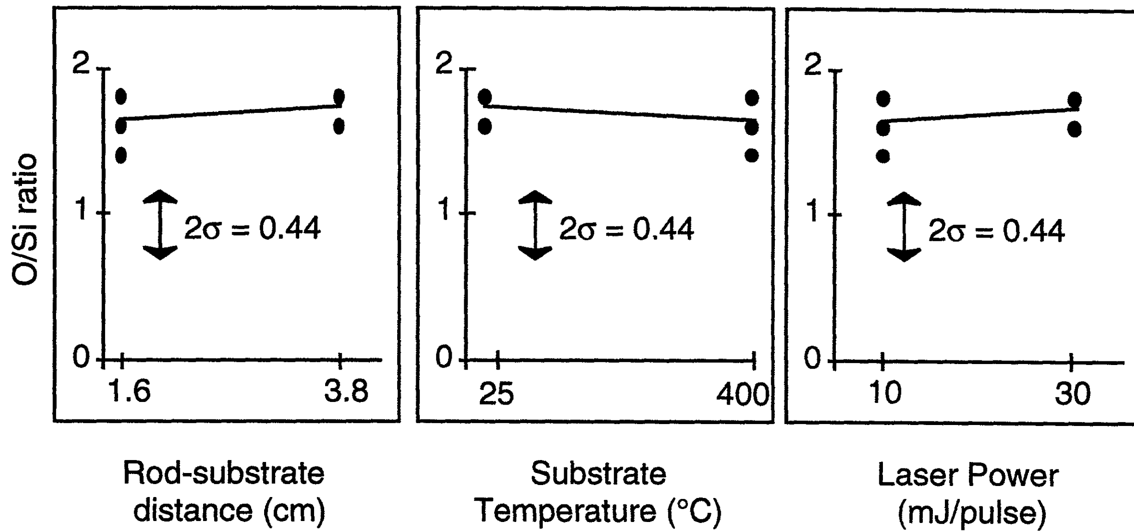


Figure 5.5 Results of a series of experiments to determine the effect of rod-substrate distance, substrate temperature, and laser power on the composition of $SiO_x$ films deposited by laser vaporization and oxidation. None of the main effects or interactions were found to be significant. The 95% confidence interval was 0.44.

| Variable | Low | High |
|---|---|---|
| Rod-substrate distance (cm) | 1.6 | 3.8 |
| Substrate temperature(°C) | 25 | 400 |
| Laser power(mJ/pulse) | 10 | 30 |

Table 5.1 Deposition conditions used in factorial experiment for optimizing O/Si ratio.

thickness variations were large. The variation in thickness is attributed to the angular distribution of material evaporated from the Si matrix rod, as laser ablation processes typically have a strongly forward-peaked distribution of ablated material.[10,11] The variation in film thickness can be reduced by increasing the rod-substrate distance, but this will also lower the overall film deposition rate.

Errors in the energy calibration of the particle detector used for RBS do not affect the determination of O/Si because the identities of the peaks are already known and only the ratio of the two peak heights has to be determined.

However, low atomic number elements such as Si and O have relativly small scattering cross-sections and the low yield of backscattered ions makes RBS less precise for these elements.[12] In addition, O has a lower atomic number than Si, so $E_O < E_{Si}$ (see Table 4.1), i.e., the energy of particles backscattered from O atoms at the surface is lower than that of ions backscattered from Si atoms. This is convoluted with particle energy loss due to penetration into the sample, so that in our sample geometry of $SiO_x$ above the Si substrate, backscattering intensity from O in the $SiO_x$ film is added to the signal from Si in the substrate. Analysis of the resulting spectrum then requres separating out the contributions from the two elements.

This is in contrast to the situation for Ge:Si composites where a heavy element, Ge, is present above a light substrate, Si. Even though the deposited film consists of a mixture of Ge and poly-Si, the Ge peak is well-defined and distinct from the poly-Si peak. Even in unchannelled spectra, there is no interference between Ge in the film and Si in the substrate (Figures 4.6–4.7).

Some error is also introduced because visual estimation was used to fit the simulated spectra to RBS data. Simulations were performed for $SiO_x$ films of various thickness and composition, and the simulated spectra matched to experimental spectra displayed on the computer screen. Fitted spectra therefore may not have been optimal in a least-square sense.

On balance, the variation in observed $SiO_x$ stoichiometry is only minimally due to errors in RBS measurement and analysis. The film stoichiometry indeed varies substantially from run-to-run. Among the contributors to run-to-run variation are fluctuations in the laser power during a run, wobbling of the rotating Si matrix rod, and changes in the Si matrix rod following laser ablation (e.g., recrystallization and impurity redistribution as a consequence of laser heating, resulting in changes in production rate, energy and distribution of evaporated species).

Laser evaporation of Si with $O_2$ in high vacuum is thus seen to not produce stoichiometric $SiO_2$ films. A contributing factor to this may be the low $O_2$ pressure attainable in the primary chamber. Based on calculations of the Si and O flux to the substrate, there is no excess $O_2$ to ensure complete oxidation of Si arriving at the substrate. Si is arriving faster than it can be oxidized, and the resulting film is Si-rich. Some means to enhance the oxidation rate and improve the stoichiometry of the films may be to use an activated oxygen beam, such as an atomic O source[13,14] or an ozone source

instead of molecular oxygen as the oxidant.[15,16]

Fogarassy et al.[6] found that stoichiometric $SiO_2$ films could be deposited by excimer laser (193 nm) ablation of fused silica targets in vacuum, without requiring additional $O_2$. Silica is transparent at the 532 nm wavelength used for PLA-SSE, however, so direct evaporation of $SiO_2$ targets was unfeasible in the current apparatus. Direct ablation of $SiO_2$ targets would only be feasible if a high power UV laser were available.†

Even though the deposited $SiO_x$ films were sub-stoichiometric at the rather coarse (~ 1 mm) scale of RBS analysis, they may consist of localized regions of stoichiometric $SiO_2$ and Si. Since the Si nanoclusters are of nanometer-scale, nanoregions of good quality $SiO_2$ may still exist and be able to passivate the Si nanoclusters so that photoluminescence is enabled.

Further analyses were therefore performed to elucidate the microstructure of the deposited $SiO_x$ films and to examine the photoluminescence behaviour of Si cluster:$SiO_x$ host composites.

## 5.4 Microstructure

### 5.4.1 Chemical bonding

#### 5.4.1.1 X-ray Photoelectron Spectroscopy (XPS)

Rutherford Backscattering provides information on the overall stoichiometry and crystallinity of a sample but does not provide any information on the chemical state of the sample. In the case of our $SiO_x$ films, there are two alternative hypotheses that could explain the sub-stoichometric nature of the films: The film could consist of Si particles embedded within a $SiO_2$ matrix, or it could consist of a homogeneous $SiO_x$ matrix. RBS is able to provide the value of $x$ but is unable to distinguish between these two hypotheses.

X-ray photoelectron spectroscopy (XPS), however, would be able to distinguish between these two hypotheses because it is able to distinguish between the different oxidation states of Si. A sample consisting of Si particles embedded in an $SiO_2$ matrix would have two distinct core-level peaks: one arising from $Si^0$ in Si particles and one from $Si^{4+}$ in $SiO_2$. A homogeneous

† The Nd:YAG laser can be tripled to 355 nm, but $SiO_2$ is still transparent at that wavelength

$SiO_x$ matrix, however, would only have a single peak intermediate between the Si and $SiO_2$ peaks.

In XPS, also known as Electron Spectroscopy for Chemical Analysis (ESCA), an X-ray beam irradiates the sample resulting in emission of electrons due to the photoelectric effect. The electrons are analyzed in an electron spectrometer, and the kinetic energies, $E_K$, of the ejected electrons are given in principle by

$$E_K = h\nu - E_B \tag{1}$$

where $h\nu$ is the energy of the X-ray photons and $E_B$ is the binding energy of the atomic orbital from which the electron originates. The elements present in a sample can thus be identified from the presence of characteristic photoelectron peaks in an XPS spectrum. In addition, the detailed core-level positions depend on the chemical state of the investigated atoms. Changes in the local charge and potential of an atom cause shifts in the core-level binding energies, and these "chemical shifts" provide information on the chemical environment of atoms in the sample.

A limitation as well as a strength of XPS is that it is a surface technique that only probes the top 50Å or less of a sample, in comparison to RBS which has a probe depth of almost 1 µm. XPS is thus very sensitive to surface contamination. When combined with an ion gun, however, XPS becomes capable of generating depth profiles. Successive layers of atoms in the sample are sputtered off, and XPS spectra of the freshly exposed surfaces are collected. The variation in XPS signal with sputtering time then allows us to determine the concentration of a species as a function of depth, subject to certain non-idealities such as differential sputtering rates and ion-induced chemical reactions.

XPS systems at the MIT Centre for Materials Science and Engineering (Perkin-Elmer 5100) and the Harvard Materials Research Laboratory (Surface Science SSX-100) were used in this work. The PE 5100 uses a Mg and Al dual anode X-ray source while the SSX-100 system uses a monochromatized Al X-ray source.

When high energy electrons strike the target in an X-ray source, a broad continuous spectrum of X-rays known as bremsstrahlung radiation is emitted as the electrons rapidly decelerate and give up their kinetic energy as photons. In addition, the incoming electrons may knock electrons out of the inner shells of atoms in the target. These vacancies are then filled by outer-shell

electrons which give off X-rays of a characteristic energy in the process. In Al, $L$ electrons falling into vacancies in the $K$ level emit X-rays with a wavelength of 8.340 Å, i.e., hν = 1486.5 eV.† The X-ray spectrum of Al thus consists of a strong Kα line plus some weaker peaks and the broad bremsstrahlung background.

In a monochromatized system, the Kα line is selected and focussed onto the sample by diffraction from a quartz crystal.[17,18] The bremsstrahlung radiation, and the non-Kα lines are eliminated. XPS spectra collected using monochromatic X-rays therefore have narrower peak widths, higher signal-to-background ratios and are free from satellite photelectron peaks that would otherwise arise from minor peaks ( $K\alpha_3$, $K\alpha_4$, $K_\beta$ and so on) that are present in the X-ray spectrum.[19] The spectra are much less intense, however, because of the diminished flux of X-rays to the specimen ( ~ 1% that for an achromatic source).

One complication in XPS is the build-up of static charge on the surface of non-conducting specimens as the specimen loses electrons by photoemission. Conductive samples in good electrical contact with the spectrometer do not have this problem as the emitted electrons are replaced by electrons flowing through the sample. For insulators and electrically isolated conductors, however, the rate of photoelectron loss is greater than the rate of replacement and a charged surface results.

In spectrometers with an achromatic X-ray source, bremsstrahlung X-rays striking the X-ray gun window and the internal surfaces of the analysis chamber generate a background of low-energy electrons that partially neutralize the positive charge on the sample surface. Equation (1) for the kinetic energy of electrons reaching the detector is then modified to take into account retardation due to the positively charged sample surface:

$$E_K = h\nu - E_B - C \qquad (2)$$

where $C$ is the steady-state static charge coorection.[20] In a "well-behaved" sample irradiated with X-rays from an achromatic source, the steady-state charge is reached within a few seconds and remains fairly stable over the

---

† The Kα line is actually a doublet consisting of $K\alpha_1$ emissionat 1486.7 eV from K → $L_{III}$ transitions and $K\alpha_2$ emission at 1486.3 eV from K → $L_{II}$ transititions. The doublet is not resolved however, and is treated as a single line at 1486.5 eV.

course of an experiment.

When an insulator is illuminated with a monochromatized X-ray source, however, a steady-state charge may not be achieved because of the absence of background electrons generated by bremsstrahlung radiation. The photoelectron spectrum may then drift with time as the static charge changes over the course of the experiment. The static charge may also vary from region to region within the sample. XPS peaks will therefore be broadened because photoelectrons emitted from sites with different static charges would arrive at the detector with different kinetics energies even if they originally had the same binding energy.

These charging problems can be ameliorated by flooding the sample with low-energy electrons from an electron gun to replace photoemitted electrons. Despite making use of the electron flood gun I experienced severe charging problems when analyzing $SiO_x$ samples in the Harvard SSX-100 instrument, which has a monochromatized X-ray source. XPS spectra of $SiO_x$ films grown on $SiO_2$ or $Al_2O_3$ substrates would often drift over time and display excessive peak broadening even when the electron flood gun was used to attempt to control the static charge. Good results were obtained, however, for $SiO_x$ samples grown on p-type Si (a conductive substrate).

In the SSX-100 system, a fine nickel grid is placed just above the sample surface to reduce charging effects. With the grid in place, it was not possible to sputter the sample either to clean the surface or to generate a depth profile. Sample loading in the SSX-100 instrument is much quicker and more convenient than in the PE 5100, however, so the SSX-100 was used to survey large sets of samples in a single session while the PE 5100 was used for depth profiling and for samples deposited on $SiO_2$ or Al $O_3$.

The PE 5100 has a non-monochromatized dual anode (Mg and Al) source but the Mg K$\alpha$ line ($h\nu$ = 1254 eV; FWHM = 0.7 eV) was used because it has a narrower line width than the Al K$\alpha$ line (FWHM = 0. 85 eV).[18] The take-off angle was 45° and the electron energy analyzer was a concentric hemispherical analyzer with a single channel detector.

The power of XPS rests substantially on its ability to distinguish non-equivalent atoms by their chemical shift, i.e., the change in binding energy of core-level peaks due to differences in the oxidation state or chemical environment of an atom. For example, Figure 5.6 shows the XPS spectrum for a Si wafer with its native oxide. The photoelectron escape depth is on the

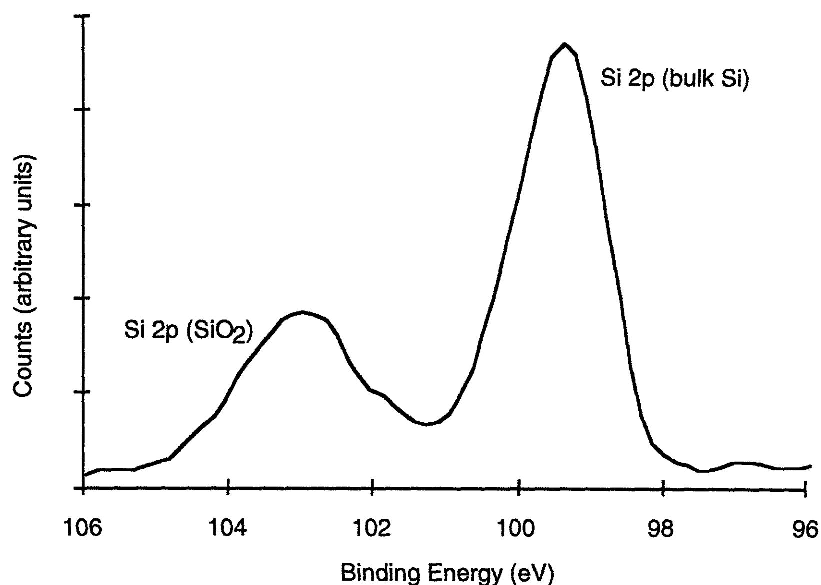


Figure 5.6 XPS spectrum of Si wafer with native oxide. Two Si 2p peaks are seen, arising from Si atoms in the oxide layer and in the bulk Si. Spectrum was collected on SSX-100 instrument with monochromatized Al Kα X-rays. Static charge effects were corrected for by setting the adventitious carbon peak (not shown) to 284.6 eV on the binding energy scale.

order of 30–40 Å while the native oxide layer is less than 20 Å thick, so two Si 2p peaks are observed, one from the underlying Si substrate and one from Si in the $SiO_2$ layer. The $SiO_2$ peak has a binding energy approximately 4 eV larger than that of bulk Si which is in agreement with the data of Wagner et al.[21] and illustrates the increase in binding energy that is associated with an increase in oxidation state.

This spectrum was taken on the SSX-100 instrument using monochromatized Al Kα X-rays with a take-off angle of 35° measured from the sample surface and a spot size of 300 μm. The electron flood gun was used and the static charge corrected for by referencing the adventitious carbon peak (not shown) to 284.6 eV.[20] This correction method assumes that organic contaminants on the sample are primarily from pump oil or similar compounds and sets the C 1s peak to the binding energy of paraffinic carbon.

Note that both peaks are assymmetrical, with the $Si^{4+}$($SiO_2$) peak skewed to lower binding energies and the $Si^0$ (Si) peak skewed to higher binding

energies. This indicates that some Si is present in intermediate oxidation states, i.e., $Si^{1+}$ ($Si_2O$), $Si^{2+}$ (SiO), $Si^{3+}$ ($Si_2O_3$) near the interface. Himpsel et al.[22] and Braun and Kuhlenbeck[23] deconvolve the overall Si $2p$ spectrum into its components and find that the $Si^{1+}$, $Si^{2+}$, $Si^{3+}$ and $Si^{4+}$ peaks are displaced by approximately 1.0, 1.8, 2.6 and 3.8 eV respectively (averages of the values reported by the two groups) from the bulk Si ($Si^0$) peak position.

5.4.1.2 Silicon monoxide structure

Prior to analyzing the $SiO_x$ XPS spectrum, let us consider the structure of silicon monoxide films. Silicon monoxide powder is prepared by heating $SiO_2$ in the presence of a reducing agent such as Si or C and quenching the vapor produced (see also Section 3.2.4 on the production of gaseous SiO by oxidation of Si). Silicon monoxide films are deposited by vacuum evaporation of SiO powder and are used as protective coatings or anti-reflective layers in optical applications and as the dielectric material in certain microelectronic devices.[24] While SiO was shown in the 1920s to exist as a monomeric molecule in the gas phase, there was considerable debate as to whether SiO in the solid phase consists of a single SiO species, or whether SiO films are composed of a mixture of various species including Si, $SiO_2$, SiO, and $Si_2O_3$.[25-31] The properties of evaporated SiO films vary substantially, depending on deposition parameters including evaporation rate, source temperature, substrate temperature and pressure in the evaporation system. This variability is clearly a major factor in the multiplicity of models proposed for the structure of SiO films.

Raider and Flitsch[31] have found that the Si $2p$ photoelectron line of SiO films prepared under high deposition rates and low vacuum pressures generally consists of a single, albeit broad, Si $2p$ line at a binding energy of 101.5 eV, approximately halfway between the binding energies of Si and $SiO_2$ (taken to be 99.3 and 103.7 eV by the authors[32]– other workers report slightly different values[19,33]). Distinct Si and $SiO_2$ impurity peaks appear in some samples, and samples prepared under lower deposition rates and higher evaporator background pressures consistently showed asymmetric peak broadening and additional Si $2p$ lines, indicating the presence of Si, $SiO_2$, oxygen-rich and silicon-rich impurities. Raider and Flitsch thus concur with Philipp's[28] conclusion that a unique SiO species does not exist in the solid state. Rather, SiO films consist of distorted tetrahedra of the type Si-($Si_xO_y$),

where $x + y = 4$, with the most probable composition being $x = y = 2$. The Si and O atoms are blended on an atomic scale. The absence of distinct Si *2p* lines at 99.3 and 103.7 eV, and the presence of a single broad line at 101.5 eV indicate that properly evaporated SiO films are not composed of a mixture of Si and $SiO_2$. *Properly prepared* SiO films only contain Si, SiO, $Si_2O_3$ and $SiO_2$ etc. as components of a normal distribution of silicon oxide species centered around $SiO_{1.0}$

5.4.1.3 Structure of laser evaporated $SiO_x$ films

By analogy with the analysis for SiO films, two alternative structures for the laser evaporated $SiO_x$ films may be hypothesized: a continuous distribution of silicon oxides with average composition O/Si $= x$, or a mixture of Si and $SiO_2$ with average composition O/Si $= x$. In the case of the former, a single Si *2p* photoelectron peak would be expected with binding energy intermediate between that of Si and $SiO_2$, and in the latter case, two distinct Si and $SiO_2$ peaks would be observed.

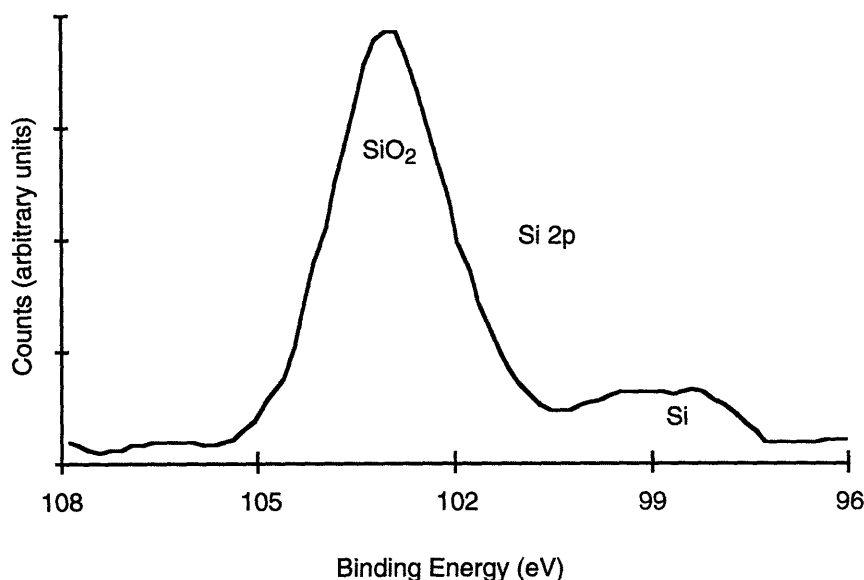


Figure 5.7 XPS spectrum of SiOx film after smoothing and background subtraction. $SiO_x$ film was deposited at room temperature with a laser fluence of 34 mJ/pulse and an oxygen pressure of $1 \times 10^{-4}$ torr onto an $Al_2O_3$ substrate. Data were collected on the PE 5100 instrument.

Figure 5.7 shows the Si *2p* peak in the XPS spectrum of an $SiO_x$ film deposited on $Al_2O_3$. This sample was deposited on an $Al_2O_3$ substrate to avoid any possibility of substrate interference in the Si 2p peak. Since the electron escape depth is on the order of nanometers, while the $SiO_x$ film is several hundred nanometers thick, no substrate interference would ordinarily be expected. Because of poor film adhesion, however, there is a possibility that parts of the substrate would be exposed and give rise to spurious XPS peaks when Si or $SiO_2$ substrates are used. This spectrum was collected on the PE 5100 instrument using Mg K$\alpha$ excitation. The analysis area was 1 mm in diameter. The data were smoothed and corrected for static charge effects as described above.

A broad shoulder towards low binding energy is observed in the Si *2p* peak in addition to a strong $SiO_2$ peak.† The shoulder is 4.5 eV wide, indicating that unoxidized Si is present in the film, as well as some Si in intermediate oxidation states. This sample was not sputter-cleaned prior to collecting the XPS spectrum, so it might be argued that the strong $SiO_2$ peak is a surface artifact, and that the interior of the film consists of less-oxidized silicon species.

The variation in the XPS signal with depth was recorded by collecting XPS spectra as surface layers were removed by sputtering the film with an $Ar^+$ ion gun. Figure 5.8 shows the Si *2p* signal as a function of sputtering time (i.e., depth) for an $SiO_x$ film deposited on Si. Two distinct Si *2p* peaks remain even after sputtering for 5 minutes with an etch rate of approximately 20 Å/min. The presence of both Si and $SiO_2$ in the $SiO_x$ film is therefore not a surface artifact, but is true of the bulk of the film as well.

The ratio of $Si^{4+}$ to $Si^0$ was estimated by taking the ratio of the heights of

---

† Both the $SiO_2$ and Si peaks have corrected binding energies smaller than handbook values (102.9 vs. 103.7 eV and 98.4 eV vs. 99.3 eV, respectively). This is most likely due to an excessive static charge correction (the correction based on adventitious carbon is only approximate). The 4.5 eV gap between the Si and $SiO_2$ peaks is also larger than expected, and cannot be explained by a simple shift in the XPS spectrum due to static charging. The larger gap could be explained by non-uniform charging, where different regions have different charges, resulting in a spreading out of the XPS peaks. These charging effects make it difficult to unambiguously assign the 102.9 eV peak to $SiO_2$. We might in fact have a distribution of silicon oxides around, say $x$=1.9, analogous to the distribution around $x$=1.0 in silicon monoxide.

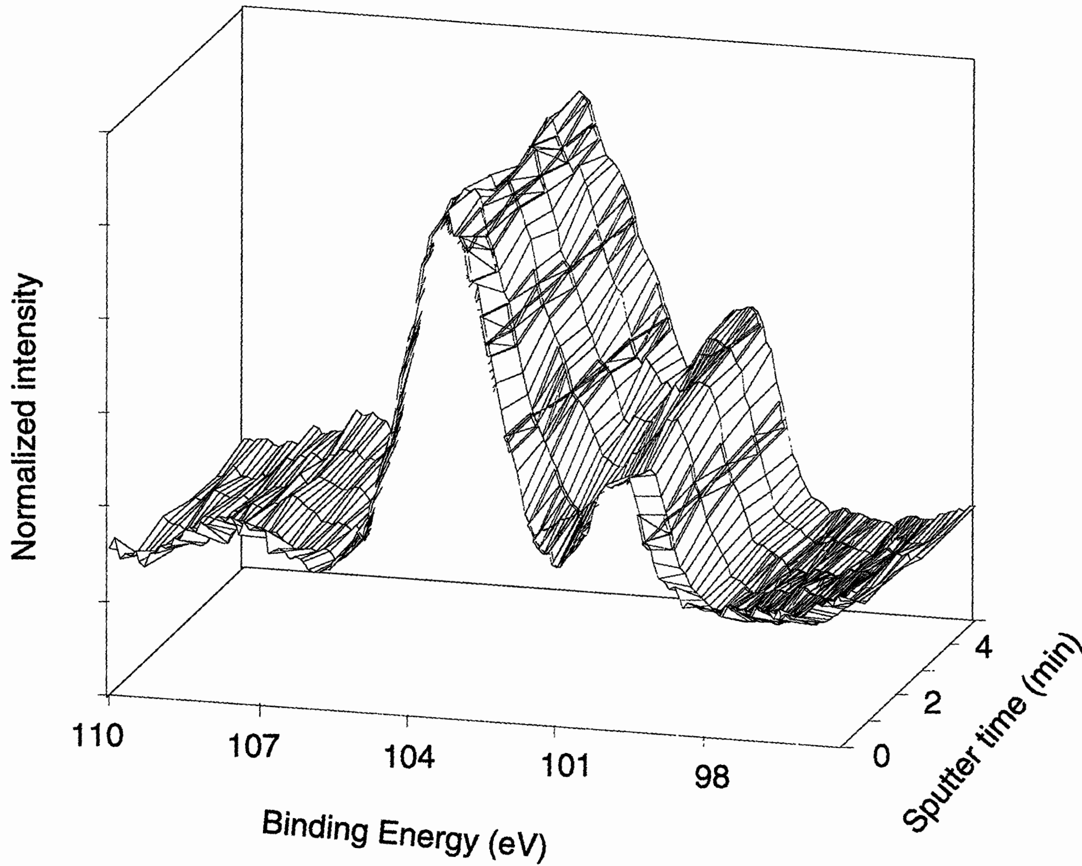


Figure 5.8 Si 2p photoelectron spectrum as a function of duration of sputtering with $Ar^+$ ions. The etch rate was approximately 20Å/min.

the peaks divided by their relative photoionization cross-sections,[22]

$$\frac{n_{Si^{4+}}}{n_{Si^0}} = \frac{p_{Si^{4+}}}{p_{Si^0}\, \sigma_{Si^{4+}}} \tag{3}$$

where $n_{Si^{4+}}$ and $n_{Si^0}$ are the density of $Si^{4+}$ and $Si^0$ in the $SiO_x$ film, $p_{Si^{4+}}$ and $p_{Si^0}$ are the heights of the $Si^{4+}$ and $Si^0$ Si $2p$ peaks respectively, and $\sigma_{Si^{4+}} = 2.2$ is the photoionization cross-section of $Si^{4+}$ relative to $Si^0$. Because the Si $2p$ peak contains intermediate oxidation state components as well as the $Si^{4+}$ and $Si^0$ peaks, deconvolution of the peak into its components would be somewhat arbitrary. The heights rather than the areas of the $Si^{4+}$ and $Si^0$ peaks were therefore used for simplicity.

As shown in Figure 5.9, there is a small increase in the $Si^{4+}/Si^0$ ratio

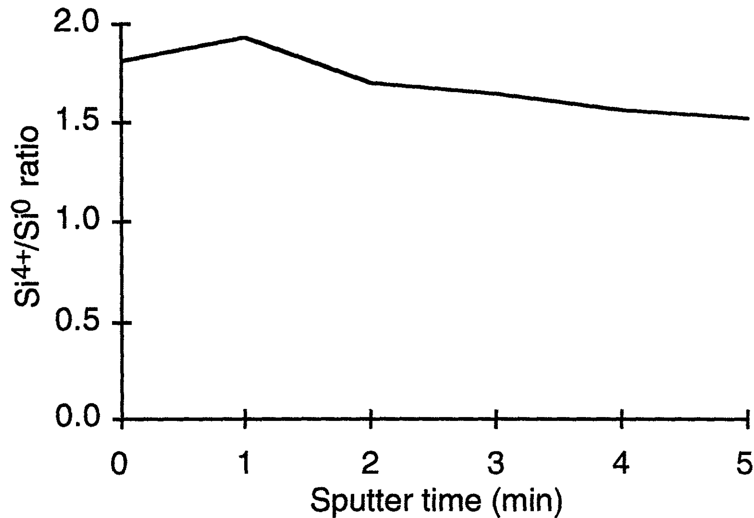


Figure 5.9 Ratio of $Si^{4+}$ to $Si^0$ in $SiO_x$ film as a function of sputter time. The $Si^{4+}/Si^0$ ratio was assumed to be equal to the the ratio of the heights of the $Si^{4+}$ and $Si^0$core-level photoelectron peaks divided by the photoionization cross-section of $Si^{4+}$ relative to $Si^0$

following the initial sputter cycle, after whch the ratio gradually declines to 1.6, equivalent to an overall stoichiometry of $SiO_{1.2}$ The $Si^{4+}/Si^0$ ratio for the previous sample shown in Figure 5.7 was 5.9, equivalent to an overall stoichiometry of $SiO_{1.7}$ On the whole, the $Si^{4+}/Si^0$ ratio varied tremendously even for films deposited under nominally identical conditions on similar substrates. This bears out the large variation in stoichiometry observed in RBS measurements, and indicates that the reactive laser evaporation process is extremely variable.

5.4.1.4 Structure of $SiO_x$ films with PLA-SSE Si clusters

One of the hypotheses originally put forward for the structure of the $SiO_x$ films was that the films consisted of a continuous distribution of silicon oxide species with an average stoichiometry $O/Si = x$. In such a structure, codepositing PLA-SSE Si clusters might encourage segregation of the film, both because of the presence of the Si clusters themseleves, and because the clusters would act as nucleation sites for the growth of larger Si particles. The Si:$SiO_x$ composite films would then be expected to have two distinct Si $2p$ photoelectron peaks rather than one.

The hypothesis of atomic-scale blending of Si and O atoms in $SiO_x$ was rejected, however, and the $SiO_x$ films found to contain Si particles even when deposited without PLA-SSE Si clusters. No consistent difference was found between the XPS spectra of $SiO_x$ films deposited with or without PLA-SSE Si clusters. The $Si^{4+}/Si^0$ ratio for $SiO_x$ films with codeposited clusters was also found to be extremely variable.

### 5.4.2 Crystallinity

The laser evaporated $SiO_x$ films have been shown by XPS to consist of a mixture of Si and $SiO_2$. An additional question that may be asked is whether the Si is present as crystalline or amorphous particles. This can be determined using the method of X-ray diffraction.

#### 5.4.2.1 X-ray Diffraction

X-ray diffraction (XRD) is based on the principle of Bragg diffraction of X-rays from a sample. X-rays are scattered in all directions by atoms in the sample, but if the sample is crystalline, the periodic arrangement of atoms gives rise to constructive interference for certain diffraction angles given by Bragg's law, [34]

$$n\lambda = 2d \sin\theta$$

where n = 1, 2, 3, ..., $\lambda$ is the X-ray wavelength, $d$ the lattice spacing and the diffraction angle, $2\theta$, is the angle between the diffracted and transmitted beams.

$SiO_x$ films with and without codeposited Si nanoclusters were deposited on fused silica substrates and analyzed in the MIT CMSE Rigaku RU 300 diffractometer using Cu K$\alpha$ ($\lambda$ = 1.5418 Å) radiation. The XRD spectra are shown in Figure 5.10 along with bars indicating the position and relative intensities of the X-ray diffraction peaks for diamond cubic silicon (JCPDS card 27-1402)[35]. Peaks are observed at 28.4°, 47.3° and 56.1° corresponding to Si (111), Si (220) and Si (311) planes, indicating that crystalline Si particles are present in the $SiO_x$ film.

Unlike in XPS*, XRD is able to probe beyond the top few monolayers, and

* The X-rays penetrate several microns into the sample in XPS also, but the photoelectrons are unable to escape unless they were generated within a few nanometers of the surface.

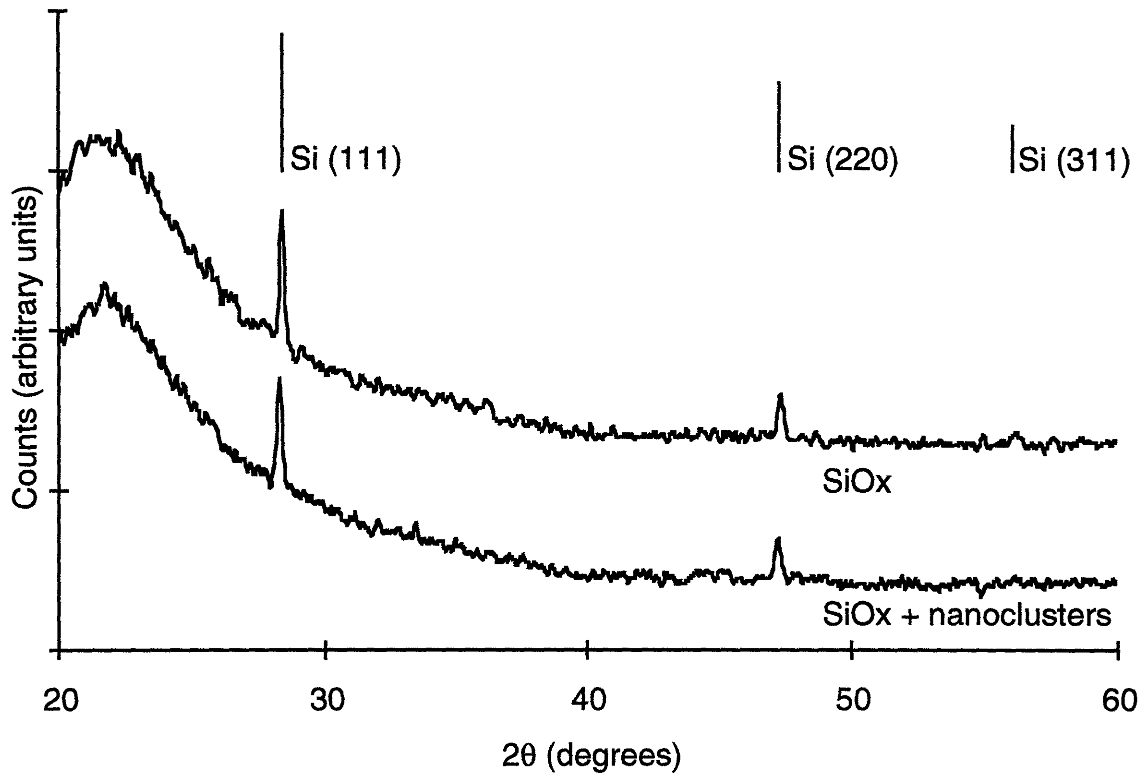


Figure 5.10 X-ray diffraction spectra of $SiO_x$ films deposited on fused silica substrates with and without codeposited PLA-SSE Si nanoclusters. Bars indicate the position andrelative intensity of diffraction peaks from diamond cubic Si (JCPDS card 27-1402). The broad background peak arises from the amorphous fused silica substrate.

some diffraction from the substrate is observed in Figure 5.10 The analysis depth varies with diffraction angle and is given by

$$G_x = (1 - e^{-2\mu x / \sin\theta})$$

where $G_x$ is the fraction of the diffracted intensity from a surface layer of depth $x$, and $\mu$ the mass absorption coefficient. Setting $G_x$ to 0.95, the analysis depth for Si ranges from 34 µm to 85 µm for diffraction angles from 20° to 60°. The deposited $SiO_x$ film thickness is < 1 µm, so a broad background peak, characteristic of amorphous materials, is also observed due to diffraction from the fused silica substrate.

It was originally hypothesized that Si particles in films deposited without PLA-SSE nanoclusters might be amorphous while particles in films deposited

with nanoclusters would be crystalline because the crystalline nanoclusters would act as seed crystals. However, this proved not to be the case, with no appreciable difference in the XRD spectra for films deposited with or without nanoclusters.

#### 5.4.2.2 Scherrer formula line broadening

X-ray diffraction also provides a measure of particle size through the width of the diffraction peaks. In small crystals, fewer crystal planes are present so only partial destructive interference is achieved for diffracting angles close to the Bragg angle. The diffraction peak is therefore broadened, with the full width at half maximum (FWHM) in radians of a diffraction peak at $2\theta$ from a crystal of size $t$ given by the Scherrer formula,[34]

$$\text{FWHM} = \frac{0.9\,\lambda}{t\,\cos\theta}$$

The diffraction spectra for Si particles of 3, 5 and 10 nm diameter and for bulk Si were simulated using the program JADE[36] and shown in Figure 5.11 The simulated patterns were generated by assuming Gaussian peak shapes with a database of peak broadening due to instrumental factors for the Rigaku instrument, and applying the Scherrer formula for line broadening due to finite particle size. The amorphous substrate background in the upper curve ($SiO_x$ without nanoclusters) of Figure 5.10 was removed by subtracting the spectrum of a fused silica blank and the processed data then plotted as curve (a) in Figure 5.11 for comparison with the simulated XRD spectra.

The widths of the Si peaks in curve (a) are essentially the same as those of the simulated peaks for bulk Si, showing that Scherrer formular broadening is negligible in the X-ray diffraction spectrum of the $SiO_x$ film. Si particles $\geq 1000$ Å in diameter must therefore be present in the laser evaporated $SiO_x$ film. Smaller particles are certainly present as well, but their contribution to the XRD spectra is overwhelmed by that of the large particles.

### 5.4.3 Ex-situ oxidation

Post-oxidation was investigated as a means of completely oxidizing the $SiO_x$ films and of indirectly measuring particle size. Given a starting particle size distribution, the average particle size will decrease with increasing oxidation until all the Si particles present are converted to $SiO_2$. Tracking the

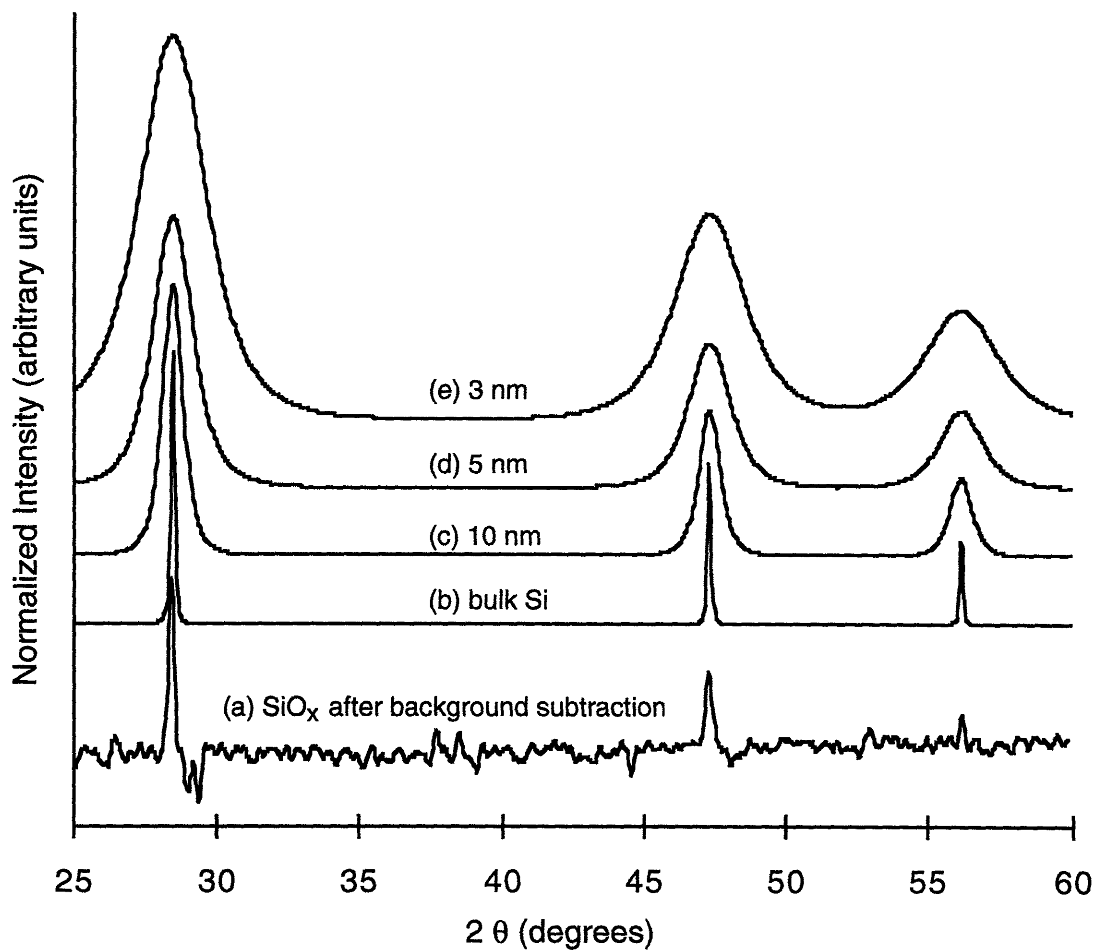


Figure 5.11 Comparison of $SiO_x$ XRD spectrum to simulated diffraction patterns for Si particles of various sizes. Bottom curve, (a), is that of $SiO_x$ following subtraction of the background signal from the fused silica substrate. Remaining curves are simulated spectra for (b) bulk Si and (c) 10 nm, (d) 5 nm and (e) 3 nm diameter Si particles.

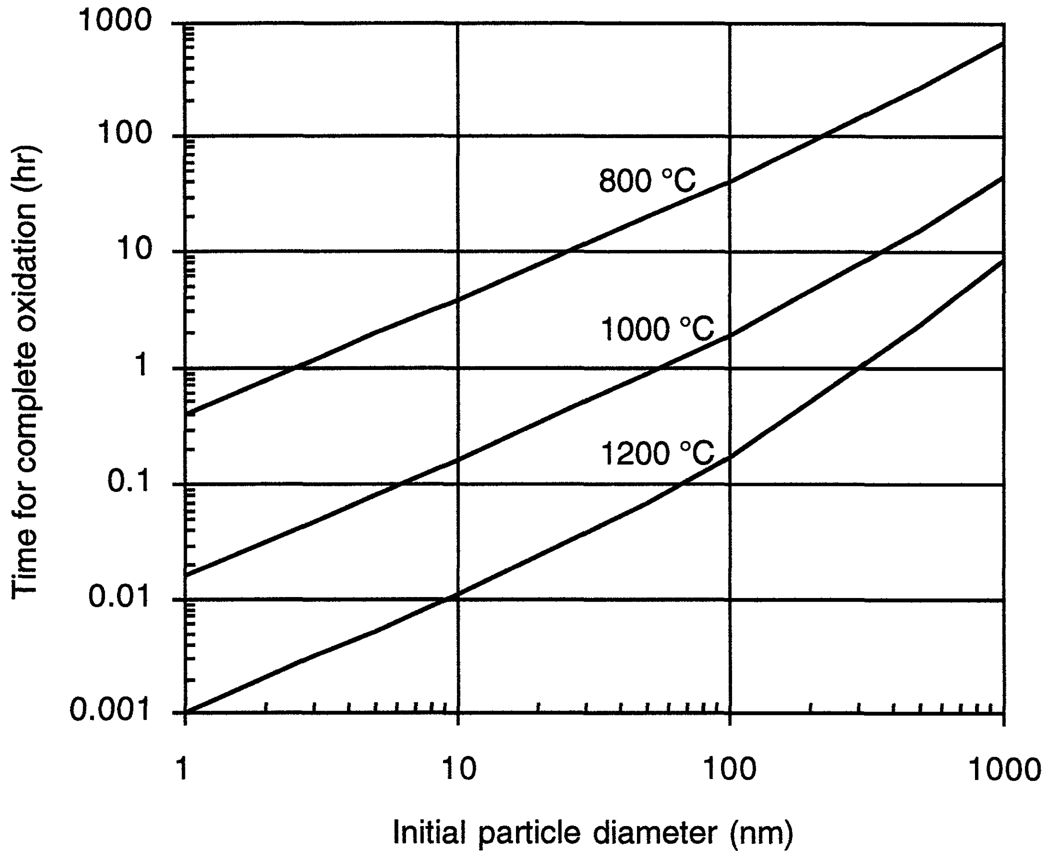


Figure 5.12 Time for complete oxidation of a spherical Si particle as a functior of its initial diameter and temperature. Oxidation is carried out in dry $O_2$ at atmospheric pressure.

intensity and width of the Si diffraction peaks as a function of oxidation time and temperature would then provide a measure of the average particle size.

Assuming that the Si particles consist of a spherical Si core surrounded by an oxide shell, $\tau$, the time required to completely oxidize a particle of initial radius $r_o$ is given by,

$$\tau = \frac{\mu}{B}\left(\frac{\mu^{2/3} - \mu}{\mu - 1} r_o^2 + A\, r_o\right) \quad (17)$$

where $\mu$ is the ratio of molar densities of Si and $SiO_2$, and A and B incorporate mass transfer and diffusion coefficients, and are defined as in the Deal-Grove model for oxidation of a Si wafer.[37] Equation (17) was derived by combining the Deal-Grove model for oxidation of Si with the Shrinking Core

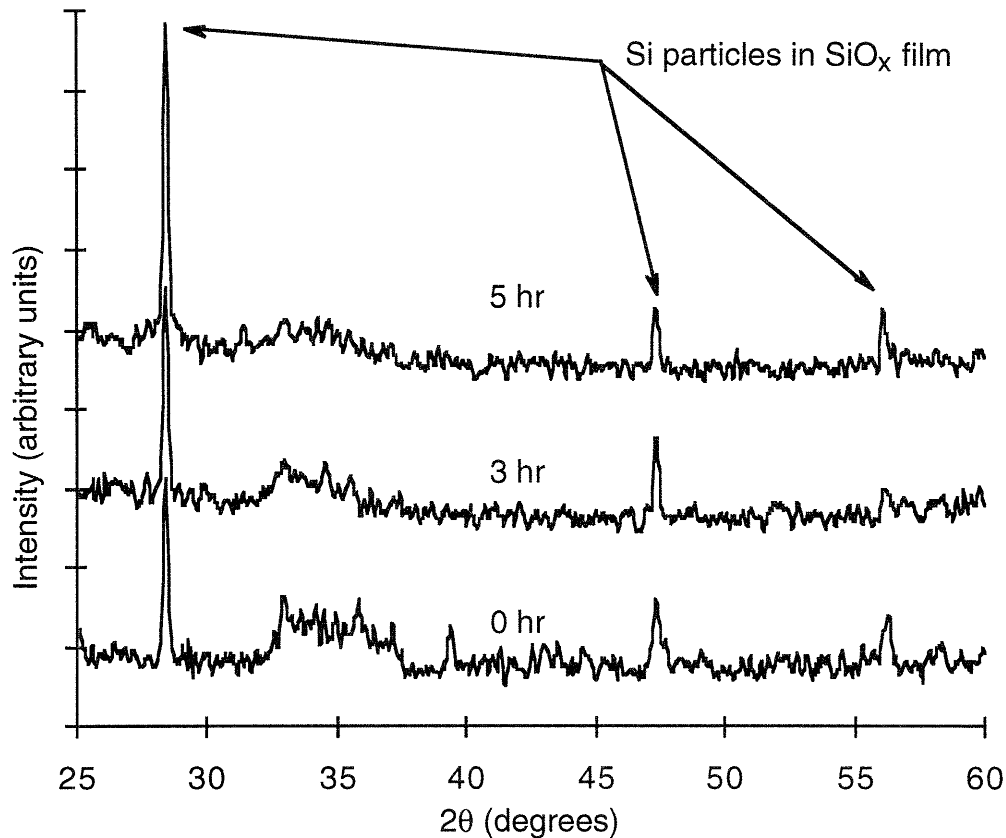


Figure 5.13 X-ray diffraction spectra for $SiO_x$ deposited with Si nanoclusters on a Si wafer following 0, 2 and 5 hours of oxidation at 1000°C. XRD signal from the Si (100) single crystal substrate was suppressed by slightly misorienting the wafer with respect to the diffractometer plane, but some traces of the Si 800 reflection remain around $2\theta = 33°$. Diffraction peaks from Si particles in the deposited $SiO_x$ film remain even after 5 hours of oxidation.

Model[38] for the reaction of a solid pellet with fluid reactants (details of the derivation are given in Section A.3) The Deal-Grove model was modified to take into account the different concentration profile in spherical Si particles compared to planar Si wafers, and the Shrinking Core Model modified to take into account the increase in particle size as Si is converted to $SiO_2$.

Given a Si particle of initial diameter, $2r_o$, Equation (17) allows us to

predict how long it would take to completely oxidize the particle under different oxidation conditions. This is plotted in Figure 5.12 for oxidation in pure dry $O_2$ at atmospheric pressure, at 800 °C, 1000°C and 1200°C. For the Si particles in our $SiO_x$ films, then, the X-ray diffraction peaks would be expected to disappear as the particles are converted from Si to $SiO_2$. The average* particle size can then be inferred from the minimum time required to completely oxidize the particles.
$SiO_x$ films were oxidized at atmospheric pressure in a tube furnace at 800°C and 1000°C with an oxygen flow of 10 scfh (Re ≥ 3000). Figure 5.13 shows the XRD spectra before oxidation and after 3 and 5 hours of oxidation at 1000°C for an $SiO_x$ film (with codeposited Si nanoclusters) deposited on to a Si wafer. X-ray diffraction from the (100) Si wafer substrate was suppressed by slightly misorienting the substrate relative to the diffractometer plane so that the Bragg condition would not be met for diffraction from the single crystal substrate. Some counts are still seen around $2\theta = 33.0°$, however, from reflection at Si 800 planes in the substrate.

Si (111), (220) and (311) peaks are seen in the spectra, indicating the presence of crystalline Si particles in the $SiO_x$ film. There was no appreciable change in the XRD spectrum with oxidation time, implying that some of the Si particles initally present must have been larger than 0.5 µm in diameter

Similar results were obtained for $SiO_x$ deposited without Si nanoclusters onto Si and $SiO_2$ substrates. The persistence of X-ray diffraction from Si particles even after prolonged oxidation thus shows that the Si particles present are fairly large, with a reasonable fraction of the Si particles initially present being larger than 0.5 µm in size.

5.4.3.1 Si particle size

Direct evidence for this is seen in SEM micrographs of the $SiO_x$ films where many particles as large as 10 µm in diameter are observed. These particles are characteristic of laser deposition processes and are due to liquid droplets ejected from the target [10].

---

* The term "average" is used in a broad sense here since the X-ray diffraction spectrum is actually the convolution of the particle size distribution, Scherrer formmula line broadening and other factors.

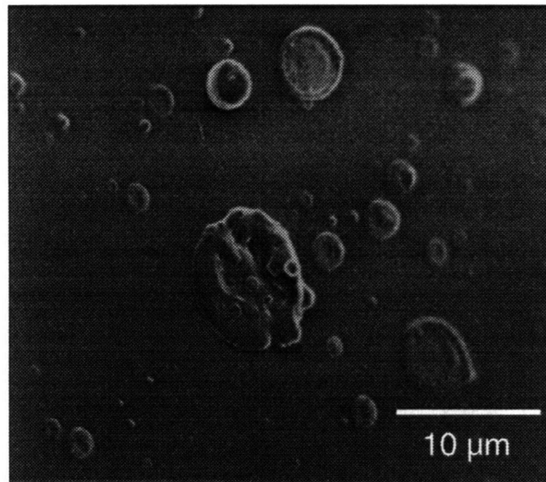


Figure 5.14 SEM micrograph of $SiO_x$ film deposited on a Si wafer. The micron-scale particles are characteristic of laser deposition and are due to liquid droplets hitting the substrate surface.

In addition to the large liquid Si droplets, laser vaporization of the Si matrix rod generates light charged and neutral $Si_n$ (n=1, 2, 3, ...) species. These light species are more likely to react with the $O_2$ gas and are deposited as a more-or-less uniform $SiO_y$ ($y \approx 2$) field. The large Si droplets do not completely oxidize, and their presence reduces the overall O/Si ratio of the as-deposited double laser ablated $SiO_x$ film. The presence of large Si particles also explains the lack of line-broadening in the X-ray diffraction spectra as well as the furnace oxidation results. A 1µm-diameter particle requires almost 50 hours of oxidation at 1000°C for complete conversion, so given the presence of large Si particles, crystalline Si cores would be expected to remain and give rise to XRD peaks even after oxidation for 5 hours, as shown in Figure 5.13.

The rapid cooling of the liquid Si droplets as they hit the cold substrate would also result in residual stress in the particles. This gives rise to the small shift in XRD peak locations relative to a stress-free standard.

The double laser ablated $SiO_x$ films consist of conductive Si particles interspersed in an insulating $SiO_2$ film. This heterogeneity results in a non-uniform charge distribution following photoionization and contributes to the

static charge problems encountered during XPS analysis.

## 5.5 Photoluminescence

Si nanoclusters deposited without a matrix do not photoluminesce immediately after deposition. PL is observed only when a passivating oxide or hydride layer is present on the nanoclusters (Section 2.4.1). These passivating layers can be formed by treating the nanoclusters with HF or $HNO_3$, or by allowing a native oxide to form on the Si nanoclusters following storage in room air for several days. The codeposited double laser ablation $SiO_x$ film was expected to perform the same passivating role so that Si:$SiO_x$ composites would photoluminesce immediately after deposition, without requiring further treatment.

No photoluminescence was observed from Si cluster:$SiO_x$ host composites, however, either as-deposited or after atmospheric oxidation. This suggests that the Si clusters are not adequately passivated, so that non-radiative recombination at surface defects dominates and suppreses the radiative processes that give rise to luminescence. We therefore decided to try annealing the composites in $O_2$ and $N_2$ in an attempt to improve the Si-$SiO_2$ interface quality.

### 5.5.1 Ex-situ oxidation

The Si dot:$SiO_x$ matrix composites were annealed in oxygen or nitrogen at 400°C, 800°C and 1000°C for lengths of time ranging from 0.5 hours to 5 hours in an effort to reduce the density of defects at the cluster interface and improve the passivation. It should be noted that several authors[39,40] have observed photoluminescence following heat treatment of Si-rich glasses. In these cases, the photoluminescence is attributed to Si nanoclusters which precipitate from the oxide. For the double laser ablation Si:$SiO_x$ composites, however, no photoluminescence was observed following annealing under a wide range of conditions.

As deposited, the interface between the codeposited $SiO_x$ and the Si nanoclusters is sufficiently defective to quench the photoluminescence that would otherwise be observed due to quantum confinement. The $SiO_x$ also prevents a passivating layer from forming by oxidation under ambient conditions.

The lack of photoluminescence following heat treatment of the Si:$SiO_x$ composites may be explained purely by the poor interface originally present between the nanoclusters and the $SiO_x$. In the case of anneals carried out in the presence of oxygen, kinetic and size distribution effects may also come into play. Given a wide particle size distribution produced by the PLA-SSE cluster source, quantum confinement effects are only observed from clusters within a certain size range, say 1–4 nm[41]. Particles in this size range and slightly larger may be completely consumed in high temperature oxidation process so that no quantum confined structures remain to photoluminesce. At the other extreme, for low temperature anneals, the oxidation reaction may be so slow that no significant changes take place in the Si:$SiO_x$ composite.

## 5.6 Importance of surface passivation

Given the ease with which Si nanoclusters deposited without a matrix demonstrate photoluminescence, it was surprising that Si nanoclusters codeposited in $SiO_x$ matrices did not show photoluminescence either as-deposited or following heat treatment. This is attributed to a highly defective interface between the Si nanoclusters and the double laser ablated $SiO_x$.

In work with II-VI quantum dot:host composites, Danek [42] showed that the photoluminescence efficiency of CdSe quantum dots codeposited in a ZnSe matrix was substantially increased by the presence of a passivating shell around the CdSe quantum dots (Section 1.3 ). For Si nanocrystals collected without a matrix, surface passivation is also seen to be essential in enabling photoluminescence. This is explained in terms of a competition between radiative and non-radiative pathways for exciton recombination. In nanocrystals with a high density of surface states, electrons and holes recombine at the surface sites without emitting any photons and photoluminescence is quenched. It is only when surface recombination sites are eliminated, as in a well-passivated Si-$SiO_2$ interface, that radiative recombination becomes favorable and photoluminescence is observed.

## 5.7 Process improvements

The double laser ablation process based on reacting $O_2$ with laser evaporated Si failed to produce stoichiometric $SiO_2$ because of the formation of Si particles and an insufficient supply of $O_2$. Workers in the field of pulsed

laser deposition[43] have found that the liquid droplets responsible for the large particles seen in Figure 5.14 are associated with high laser powers. The density of these particles could therefore be reduced by using lower laser fluences, with the trade-off of lower deposition rates. Velocity filters can also be used to mechanically chop out the ejected particles before they reach the substrate.[11]

Particle formation is much less of a problem when using thermal or e-beam evaporators, and these could be used as an alternative deposition technique. $SiO_2$ sources could also be used instead of Si if a thermal or e-beam evaporator is used. This would improve the stoichiometry of the deposited film as stoichiometric $SiO_2$ films can be deposited under lower $O_2$ pressure or without having to supply $O_2$ at all.[44-46]

The other limiting factor in the reactive laser evaporation process is the oxygen pressure in the primary chamber during deposition. The calculations of Section 5.2.1 suggest that a higher O/Si ratio could be achieved by increasing the oxygen flux to the substrate. However, the oxygen pressure cannot be raised further due to the need to maintain a vacuum for the supersonic expansion. An alternative would be to use a more reactive form of oxygen such as ozone or an atomic oxygen beam generated by a microwave plasma source. This would presumably increase the reaction probablity between O and Si while maintaing a low pressure in the chamber.

## 5.8 Summary

Si cluster:Silicon oxide host composites were fabricated by combining PLA-SSE with reactive laser evaporation. These composites did not photolumines-ce because of the poorly passivated interface between Si nanoclusters and the oxide host. The silicon oxide host was silicon-rich because of the presence of large Si particles ejected from the target and low oxygen pressure in the deposition chamber. The overall stoichiometry of the $SiO_x$ films was determined by RBS, and $x$ found to vary from 1.4 to 1.8 SEM micrographs showed the presence of large (~ 1μm) particles with shapes suggesting that they were formed by the impingement of liquid Si droplets onto the substrate. This was supported by XPS data showing that "bulk" Si as well as $SiO_2$ was present in $SiO_x$ films even when Si nanoclusters were not codeposited with the $SiO_x$. X-ray diffraction showed that the Si particles were crystalline.

No photoluminescence was observed from the Si:$SiO_x$ composites despite

the presence of Si nanoclusters which are known to photoluminesce when coated with $SiO_2$. This shows that $SiO_x$ deposited by reactive laser evaporation does not passivate the interface with Si, and demonstrates the importance of surface effects in nanoscale quantum dots.

## REFERENCES


1. Y. Mishima, M. Hirose, and Y. Osaka, "Direct photochemical deposition of $SiO_2$ from the $Si_2H_6 + O_2$ system," J. Appl. Phys. **55** (4), 1234 (1984).
2. W. R. Gentry and C. F. Giese, "Ten-microsecond pulsed molecular beam source and a fast ionization detector," Rev. Sci. Instrum. **49** (5), 595 (1978).
3. J. R. Engstrom and T. Engel, "Atomic versus molecular reactivity at the gas-solid interface: The adsorption and reaction of atomic oxygen on the Si(100) surface," Phys. Rev. B **41** (2), 1038 (1990).
4. M. P. D'Evelyn, M. M. Nelson, and T. Engel, "Kinetics of the adsorption of $O_2$ and of the desorption of SiO on Si(100): A molecular beam, XPS and ISS study," Surf. Sci. **186**, 75 (1987).
5. G. Hollinger and F. J. Himpsel, "Oxygen chemisorption and oxide formation on Si(111) and Si(100) surfaces," J. Vac. Sci. Technol. A **1** (2), 640 (1983).
6. E. Fogarassy, C. Fuchs, A. Slaoui, S. de Unamumo, and J. P. Stoquert, "Low-temperature synthesis of silicon oxide, oxynitride, and nitride films by pulsed excimer laser ablation," J. Appl. Phys. **76** (5), 2612 (1994).
7. L. R. Doolittle, "Algorithms for the rapid simulation of Rutherford Backscattering Spectra," Nucl. Instrum. Meth. Phys. Res. B **9**, 344 (1985).
8. G. E. P. Box, W. G. Hunter, and J. S. Hunter, *Statistics for experimenters* (John Wiley & Sons, New York, 1978).
9. D. C. Montgomery, *Design and analysis of experiments*, 3rd ed. (John Wiley & Sons, New York, 1991).
10. J. T. Cheung and H. Sankur, "Growth of Thin films by laser-induced evaporation," CRC Crit. Rev. Solid State Mater. Sci. **15**, 63 (1988).
11. D. B. Chrisey and G. K. Hubler, "Pulsed laser deposition of thin films," (John Wiley & Sons, New York, 1994).
12. W.-K. Chu, J. W. Meyer, and M. A. Nicolet, *Backscattering Spectrometry* (Academic Press, New York, 1978).
13. S. J. Sibener, R. J. Buss, C. Y. Ng, and Y. T. Lee, "Development of a supersonic $O(^3P_J)$, $O(^1D_2)$ atomic oxygen nozzle beam source," Rev. Sci. Instrum. **51** (2), 167 (1980).
14. J. R. Engstrom, D. J. Bonser, M. M. Nelson, and T. Engel, "The reaction of atomic oxygen with Si(100) and Si(111): I. Oxide decomposition, active oxidation and the transition to passive oxidation," Surf. Sci. **256**, 317 (1991).
15. M. Niwano, M. Suemitsu, Y. Ishibashi, Y. Takeda, N. Miyamato, and K. Honma, "Ultraviolet ozone oxidation of Si surface studied by photoemission and surface infrared spectroscopy," J. Vac. Sci. Technol. A **10** (5), 3171 (1992).
16. T. Maruyama and S. Ohtani, "Silicon dioxide thin films prepared by chemical vapor deposition from tetrakis(diethylamino)silane and ozone," Appl. Phys. Lett. **64** (21), 2800 (1994).
17. W. M. Riggs and M. J. Parker, "Surface analysis by x-ray photoelectron spectroscoy," in *Methods of surface analysis*, edited by A. W. Czanderna (Elsevier, Amsterdam, 1975), Vol. 1, p. 126.
18. J. C. Rivière, "Instrumentation," in *Practical Surface Analysis*, edited by D. Briggs and M. P. Seah (John Wiley & Sons, Chichester, 1983), p. 17.

19. C. Wagner, "Passivity during the oxidation of silicon at elevated temperature," J. Appl. Phys. **29** (9), 1295 (1958).
20. P. Swift, D. Shuttleworth, and M. P. Seah, "Static charge referencing techniques," in *Pracical Surface Analysis*, edited by D. Briggs and M. P. Seah (John Wiley and Sons, Chichester, 1983), p. 437.
21. C. D. Wagner, W. M. Riggs, L. E. Davis, J. F. Moulder, and G. E. Muilenberg, *Handbook of X-ray photoelectron spectroscopy* (Perkin Elmer Corporation, Eden Prairie, Minnesota, 1979).
22. F. J. Himpsel, F. R. McFeely, A. Taleb-Ibrahami, J. A. Yarmoff, and G. Hollinger, "Microscopic structure of the $SiO_2$/Si interface," Phys. Rev. B **38** (9), 6084 (1988).
23. W. Braun and H. Kuhlenbeck, "Chemical structure of ultrathin thermally grown oxides on a SI(100) wafer using core level photoemission," Surf. Sci. **180**, 279 (1987).
24. H. R. Philipp, "Silicon monoxide (SiO) (Noncrystalline)," in *Handbook of Optical Constants of Solids* (Academic Press, 1985), p. 765.
25. L. Brewer and F. T. Greene, "Differential thermal analysis of the Si-$SiO_2$ system," J. Phys. Chem. Solids **2**, 286 (1957).
26. G. W. Brady, "A study of amorphous SiO," J. Phys. Chem. **63**, 1120 (1959).
27. Y. Nishimura, T. Inagaki, and H. Sasaki, "Some physical properties of evaporated silicon oxide film," Fujitsu Sci. Tech. J. , 87 (1966).
28. H. R. Philipp, "Optical properties of non-crystalline Si, SiO, $SiO_x$ and $SiO_2$," J. Phys. Chem. Solids **32**, 1935 (1971).
29. J. A. Yasaitis and R. Kaplow, "Structure of amorphous silicon monoxide," J. Appl. Phys. **43** (3), 995 (1972).
30. S. C. H. Lin and M. Joshi, "Structure of silicon monoxide," J. Electrochem. Soc. **116** (12), 1740 (1969).
31. S. I. Raider and R. Flitsch, "Silicon monoxide thin films," J. Electrochem. Soc. **123** (11), 1754 (1976).
32. R. Flitsch and S. I. Raider, J. Vac. Sci. Technol. **12**, 305 (1975).
33. D. Briggs and M. P. Seah, "Practical Surface Analysis," (John Wiley & Sons, Chichester, 1983).
34. B. D. Cullity, "Elements of X-ray diffraction," (Addison-Wesley Publishing Company, Inc., Reading, Massachusetts, 1978).
35. Joint Committee on Powder Diffraction Standards, *Powder diffraction file* (JCPDS International Centre for Diffraction Data, Swarthmore, Pa., ).
36. Materials Data Inc., JADE (Materials Data, Inc., Livermore, CA, 1994).
37. S. Wolf and R. N. Tauber, *Silicon Procesing for the VLSI Era* (Lattice Press, 1986).
38. O. Levenspiel, *Chemical Reaction Engineering*, 2nd ed. (John Wiley & Sons, New York, 1972).
39. K. Kohno, Y. Osaka, F. Toyomura, and H. Katayama, "Photoluminescence of Si microscrystals embedded in $SiO_2$ glass films," Jpn. J. Appl. Phys. **33 (Part 1)** (12A), 6616 (1994).
40. H. A. Atwater, K. V. Shcheglov, S. S. Wong, K. J. Vahala, R. C. Flagan, M. L. Brongersma, and A. Polman, "Ion Beam Synthesis of Luminescent Si and Ge Nanocrystals in a Silicon Dioxide Matrix," in *Materials Research Society Symposia Proceedings* (Materials Research Society, Boston, MA, 1993), Vol. 316, pp. 409.
41. S. Schuppler, S. L. Friedman, M. A. Marcus, D. L. Adler, Y. H. Xie, F. M. Ross, T. D. Harris, W. L. Brown, Y. J. Chabal, L. E. Brus, and P. H. Citrin, "Dimensions of luminescent oxidized and porous silicon," Phys. Rev. Lett. **72** (16), 2648 (1994).
42. M. Danek, "Chemical approaches to organometallic chemical vapor deposition of wide band-gap II-VI layers and nanocrystal composites," PhD. thesis, Massachusetts Institute of Technology, 1995.
43. D. H. Lowndes, "Growth of epitaxial thin films by pulsed laser ablation," in *Eighth International Summer School on Crystal Growth* (1993).
44. P. Archibald and E. Parent, "Source evaporant systems for thermal evaporation," Solid

State Technol. **19** (7), 32 (1976).

45. E. B. Graper, "Evaporation characteristics of materials from an electron beam gun II," J. Vac. Sci. Technol. A **5** (4), 2718 (1987).

46. E. Ritter, "Deposition of oxide films by reactive evaporation," J. Vac. Sci. Technol. **3**, 225 (1966).

# Chapter 6
# Er Nanocluster:Si Host Composites

Pulsed Laser Ablation-Supersonic Expansion (PLA-SSE) produces bare clusters *in vacuo* and can be combined with a variety of thin film deposition techniques to synthesize a wide range of nanocluster:host composites. Luminescence at 1.54 µm has previously been observed from Er-doped materials, and this phenomenon has potential optoelectronic and photonic applications.

Er:Si composites were therefore synthesized by codepositing PLA-SSE Er clusters into Si host matrices deposited by laser evaporation. The PLA-SSE Er:Si composites exhibit 1.54 µm luminescence with a higher PL yield than ion-implanted Er-doped Si. The PLA-SSE Er:Si composites also show significantly less quenching of PL intensity than Er-implanted Si, as temperature is increased from 4 K to 300 K. Large concentrations of C and O impurities are detected in the PLA-SSE Er:Si composites. In other Er-doped materials, C and O have been shown to enhance Er-related luminescence, so the strong 1.54 µm luminescence observed in PLA-SSE Er:Si composites may in fact be due to the high C and O levels present, rather than quantum confinement effects.

## 6.1 Flexibility of PLA-SSE process

Pulsed Laser Ablation-Supersonic Expansion can be used to generate clusters from almost any solid material including metals (e.g., Mo, Pb, Sn), non-metals (e.g., C) and elemental and compound semiconductors (e.g., Si, Ge, GaAs, InP)[1] PLA-SSE nanoclusters are generated in vacuo, and initally have bare surfaces without any capping layers present. This allows PLA-SSE to be combined with almost any vacuum deposition technique to generate a wide range of nanocluster:host composites.

In this thesis work, the same apparatus was used to synthesize Ge:Si, Si:$SiO_x$, Ag:Si[†] and Er:Si composites, with only minor modifications required for each cluster:host combination. This demonstrates the flexibility of the

---

[†] Ag:Si composites were used in testing the PLA-CVD system early in the development of the process.

PLA-SSE process whereby a variety of nanoclusters were generated and codeposited into host matrices grown by several techniques including chemical vapor deposition, laser evaporation and reactive laser evaporation.

While the vacuum requirements of the PLA-SSE process retarded the growth rate of Si by CVD from $Si_2H_6$, and resulted in a sub-stoichiometric deposit for reactive laser evaporation of $SiO_x$, the low gas density does not adversely affect purely physical vapor deposition (PVD) techniques such as laser evaporation without reaction. For PVD processes such as thermal, e-beam or laser evaporation, high vacuum is in fact required to ensure the purity of the deposited film.[2,3]

## 6.2 Er-related luminescence

Er is a rare earth metal with atomic number 68 and electronic configuration $[Xe]4f^{12}6s^2$. Its trivalent ion has the electronic configuration $[Xe]4f^{11}$, where the partially-filled $4f$ shell is electronically shielded by filled $5s^25p^6$ shells. In the free $Er^{3+}$ ion, all the $4f$ states have equal parity and electric dipole transitions between them are forbidden by parity selection rules.[4,5] Radiative and absorptive transitions are therefore not observed in the free ion. When $Er^{3+}$ is subjected to an external electric field originating from a crystalline or glass host, however, the $4f$ states are perturbed and lose their degeneracy. Intra-$4f$ shell transitions then become weakly allowed. In particular, a radiative transition from the first excited state, $^4I_{13/2}$, to the ground state, $^4I_{15/2}$, gives rise to emission at 1.54 μm when Er is incorporated into a wide variety of hosts including silica, germania and halide glasses,[5] and crystalline or amorphous Si.[6-9] The energy of this transition is relatively independent of host material and temperature because the $4f$ shell is shielded by $5s^2$ and $5p^6$ orbitals. Furthermore, this wavelength coincides with the minimum loss wavelength of silica-based optical fiber, so Er-related luminescence is of great technological interest. For example, an Er-Si LED would be an ideal candidate for integration of Si-based microelectronics with silica-based optical waveguides for optoelectronic applications.

Research on the luminescence properties of Er-doped Si has up till now mainly been conducted using Si wafers ion-implanted with Er.[6-9] Er-implanted Czochralski (Cz) Si shows a higher 1.54 μm band PL intensity than Float Zone (FZ) Si (Cz Si has higher O levels than FZ Si) and the PL intensity has

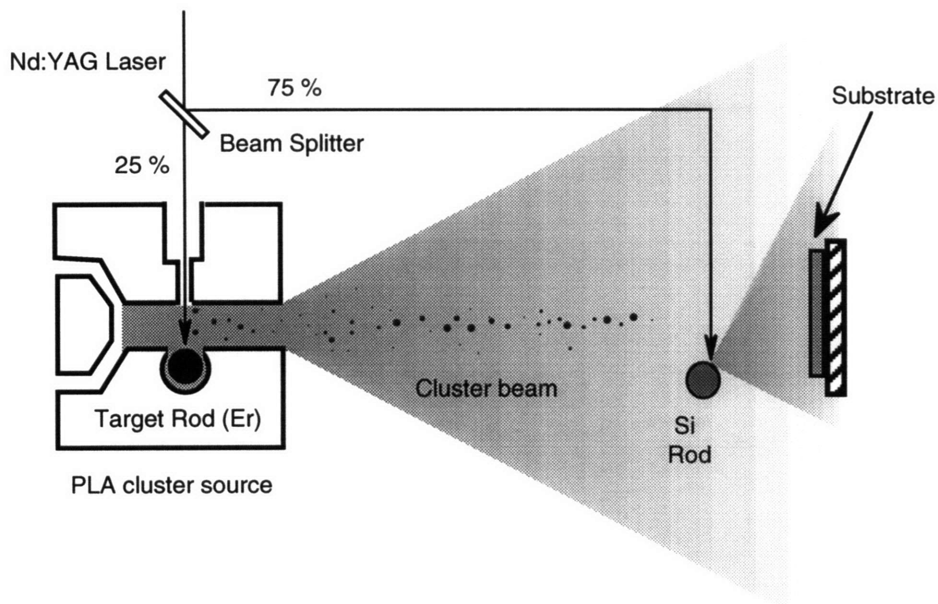


Figure 6.1 Double laser ablation process for codepositing Er nanoclusters in a Si host matrix. The Nd:YAG laser beam is split into two beams with one beam (25% of the original beam energy) used in the PLA-SSE cluster source and another (75 %) used to laser evaporate a second Si rod placed close to the substrate.

also been shown to be enhanced by co-implanting O with the Er.[6,8] These results indicate that Er-O complexes are implicated in the luminescence from Er-doped Si. Co-implantation of C, N or F also enhance the luminescence from Er-implanted Si,[6] presumably because of symmetry-breaking effects.

## 6.3 Double laser ablation process

Er:Si composites were synthesized by codepositing PLA-SSE Er nanoclusters with laser-evaporated Si. The frequency-doubled Nd:YAG laser beam was split as shown in Figure 6.1, with ~ 25% of the beam continuing to the PLA-SSE cluster source and ~75% used to laser evaporate a second Si rod placed ~ 10 cm away from the substrate. The second Si rod is rotated by connection to a motor-driven screw, but there is no gas flow over the point of ablation, and no confinement of the ablated material, as there is in the PLA-SSE source.

This is essentially the same set-up as that used for $SiO_x$ deposition, except that in the $SiO_x$ deposition system, $O_2$ is introduced through a doser to oxidize the laser-evaporated Si arriving at the substrate (Section 5.2) In the Er:Si system, O has been shown to enhance luminescence from $Er^{3+}$ centers, and is often introduced by ion-implantation.[6] Although this later turned out to be unnecessary, we originally planned to introduce oxygen into PLA-SSE Er:Si composites by using He-$O_2$ mixtures as the carrier gas in the PLA-SSE cluster source.

## 6.4 Photoluminescence

Photoluminescence spectra of Er nanoclusters and Er:Si composites were measured by exciting the samples with $Ar^+$ laser radiation and collecting the emission with a 0.75 m Spex monochromator and a liquid-$N_2$-cooled Ge photodetector. The samples were held in a bath cryostat and their temperatures could be set between room temperature and liquid He temperature (4 K). The continuous-wave 488 nm laser beam was mechanically chopped with a chopper wheel and the photodetector output fed to a lock-in amplifier to enhance the signal-to-noise ratio.

Er nanoclusters deposited without a host matrix did not photoluminesce either at room temperature or at 4 K. When Er nanoclusters are codeposited in a Si host matrix, however, the as-deposited Er:Si composite exhibits weak photoluminescence at 1.54 µm, characteristic of $Er^{3+}$. The 1.54 µm peak is strongly enhanced by a 0.5 hour anneal in Ar at 500°C (Figure 6.2; These spectra are for composites deposited on (100) Cz Si wafers.) The as-deposited composites also show PL peaks at 1.28 µm and 1.57 µm designated as "G" and "C" lines respectively.[10] The "G" line is assigned to a complex of two C atoms and one Si atom, while the "C" line is assigned to a complex of one C atom and one O atom.

The "C" and "G" lines are also observed following irradiation of C-doped Czochralski Si by electrons or ions. Above room temperature, interstitial C atoms become mobile and are captured by existing C substitutional atoms or by O atoms, creating luminescent centers.[10] The "C" line at 1.57 µm is not present in Er:Si composites deposited on glass microscope cover slides, which suggests that the "C" line seen in Figure 6.2 is due to C-O pairs created in the Si substrate by the impact of hot Si species during laser evaporation of the Si

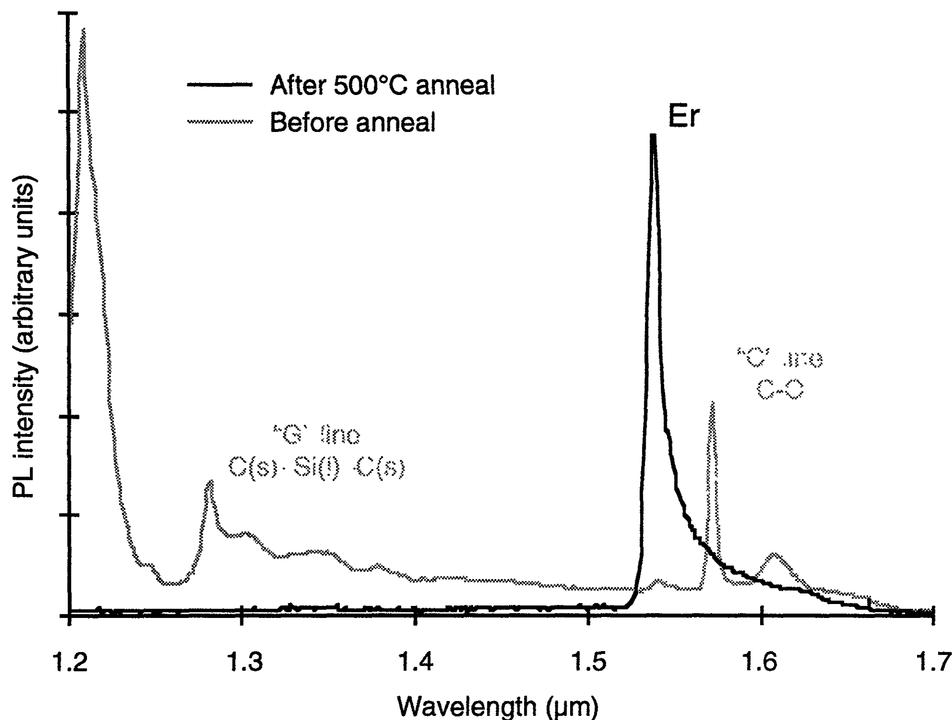


Figure 6.2 Photoluminescence spectra of Er:Si composite before and after a 30 minute anneal in Ar at 500°C. Luminescence from C and O impurity centers is eliminated, while Er-related luminescence is enhanced by annealing.

matrix. In irradiated C-doped crystalline Si, C-O centers are destroyed by annealing at temperatures above 350 °C, and this is observed in our annealing experiments as well.

The "G" line at 1.28 μm is present in Er:Si composites deposited either on Si (100) wafers or glass cover slips, which shows that it is associated with the deposited Si matrix rather than the Si substrate. This luminescence center consists of two substitutional carbon atoms and one interstitial silicon atom, and its presence in the deposited Er:Si composite suggests that the laser evaporated Si matrix is crystalline. This is confirmed by the presence of Si diffraction lines in glancing angle X-ray diffraction spectra of Er:Si composites.

The dependence of the 1.54 μm band PL intensity on annealing temperature is shown in Figure 6.3 The anneals were performed for 30

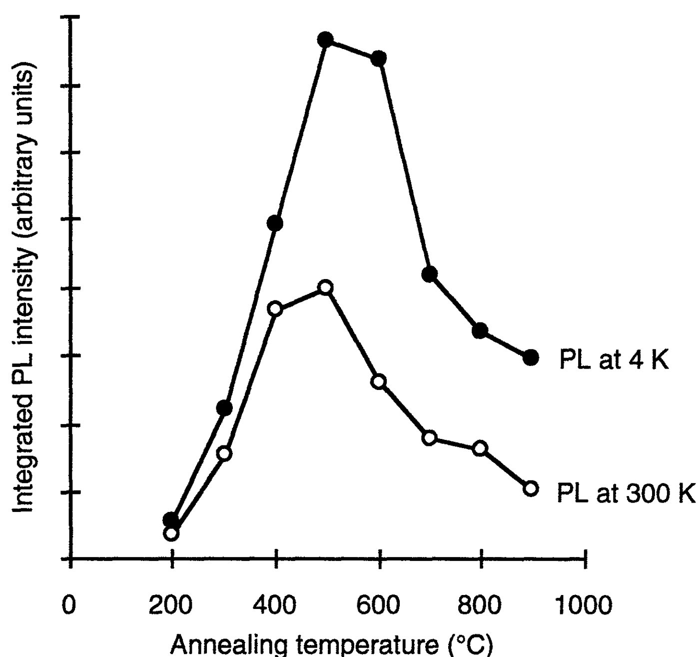


Figure 6.3 Integrated PL intensity as a function of annealing temperature. All anneals are carried out in Ar for 30 minutes. PL spectra were collected at 300 K and 4K.

minutes under Ar in a tube furnace with the Er:Si composites placed between two Si wafers to prevent outdiffusion and contamination. The maximum PL intensity is achieved at an annealing temperature of 500°C, and is two orders of magnitude greater than the PL intensity of an unannealed sample.

Photoluminescence from Er-implanted Si is strongly temperature dependent, and the PL intensity at 300 K is three orders of magnitude weaker than at 4 K.[6] In contrast, for PLA-SSE Er:Si composites, the PL intensity at 300 K only falls to 50% of the intensity at 4 K (Compare the 300 K and 4 K lines in Figure 6.3 for samples annealed above 500°C).

The PL intensity of PLA-SSE Er:Si composites is also much stronger than that of Er-implanted Cz Si. Photoluminescence from PLA-SSE Er:Si composites at room temperature is more intense than that from Er-implanted Cz Si at 4 K. It should be noted that the PL intensity from Er-implanted amorphous Si and SIPOS are reported to be higher than from crystalline Si,[9,11] but we have not yet directly compared the luminescence intensity of

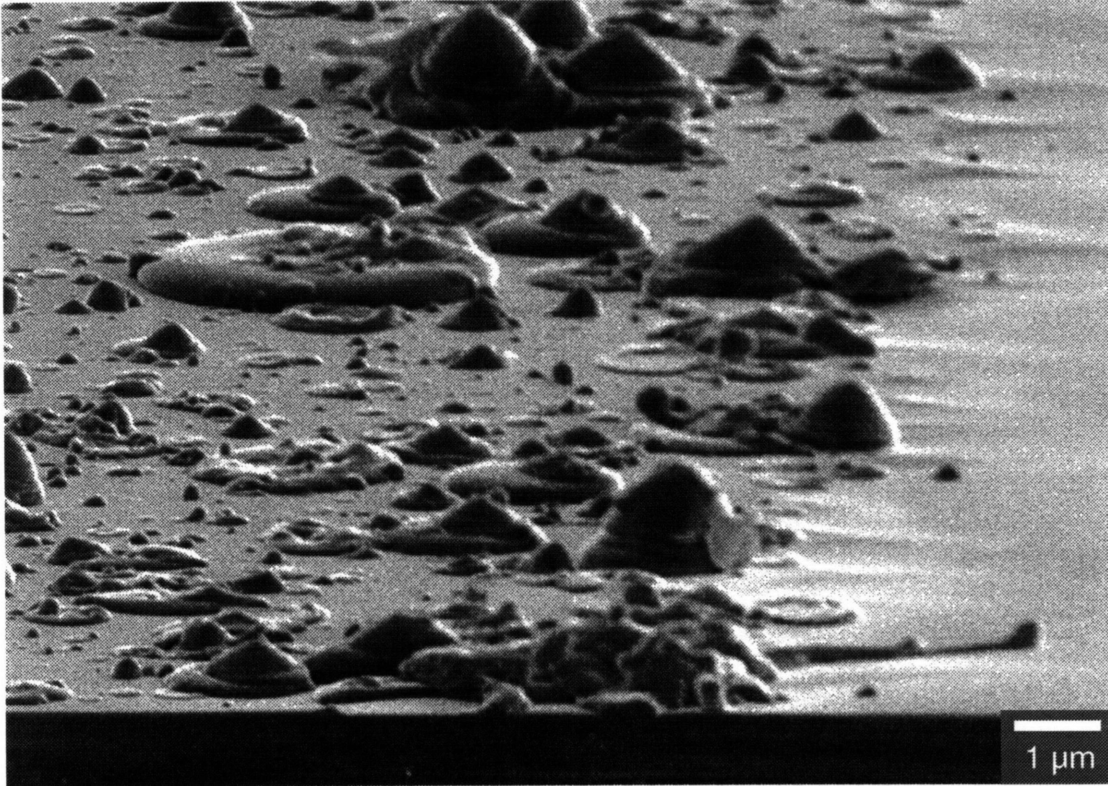


Figure 6.4 SEM micrograph of Er:Si composite deposited on a Si wafer at room temperature for 3 hours. Sample is viewed from the edge at an angle of 15°, and the open area to the right is a portion of the substrate which was masked during deposition. The striated cones are formed by the rapid solidification of liquid Si droplets, and the discs formed by Si droplets which cool off more slowly. The smaller spheres are most likely Er particles.

these materials to that of PLA-SSE Er:Si composites. PLA-SSE is thus a very promising technique for synthesizing luminescent Er-Si materials. Further details of the photoluminescence study are given in Thilderkvist et al.[12]

## 6.5 Electron microscopy

An SEM micrograph of an Er:Si composite deposited at room temperature for 13 hours is shown in Figure 6.4 The film is seen to consist of an underlying "carpet" with many irregularly shaped particles embedded in it. The large striated cones are formed by liquid Si droplets ejected from the

target by laser ablation,[13-15] which rapidly cool and solidify on hitting the substrate. Other droplets which cool off more slowly form flatter, disc-like structures. Both are characteristic of pulsed laser film deposition (see, for example, figure 5 of Antoni et al.[16]).† The more-or-less uniform "carpet" layer is laid down by light Si species ($Si_n$, small $n$) which are also produced by laser vaporization. This layer has a thickness of approximately 0.2 μm. The open area to the right is a portion of the Si wafer substrate that was masked during deposition.

Element maps for the Er:Si composites were collected using Energy Dispersive X-ray Spectroscopy (EDS) in the SEM. An element map is shown in Figure 6.5, where bright areas in parts (b) and (c) represent regions of higher Er or Si density respectively. The bright spherical particles present in the SEM image, part (a), are thus identified as large (> 1 μm) Er particles. As noted previously, the P LA-SSE cluster source produces a wide range of particle sizes, and nanoscale Er clusters are certainly present, but could not be resolved in the SEM

Cathodoluminescence (CL) maps of the composite were also generated in the SEM by using a Ge photodetector to collect light emission from the sample as the electron beam was rastered across the sample. Figure 6.6shows that cathodoluminescence is strongest from the solidified Si droplets but is absent from the spherical Er particles.It is reasonable to assume that the same luminescent centers are responsible for light emission from Er:Si composites regardless of the mode of excitation. The absence of CL from Er particles is therefore consistent with the absence of PL from PLA-SSE Er clusters deposited without a Si host matrix.

It is possible that nanometer-scale Er quantum dots embedded in the large Si droplets are responsible for the 1.54 μm luminescence observed, but there have been no previous reports of light emission from metallic nanoclusters,

---

† The Si cones and discs shown in Figure 6.4 bear a strong resemblance to chocolate-chip candy because the methods of synthesis are similar for both materials. Chocolate chips are formed by dropping liquid chocolate onto cooled surfaces, with the shape of the drop depending on the viscosity and thermal properties of the chocolate and the cooling rate (B. W. Minifie, *Chocolate, Cocoa and Confectionery: Science & Technology*, The Avi Publishing Company, Westport, CT, 1970; J. Urbanski, "Chocolate manufacturing: Drops, Chips, Chunks, etc.," The Manufacturing Confectioner, vol. 74 , pg. 47, November 1994).

(a) SEM Image

(b) Er map

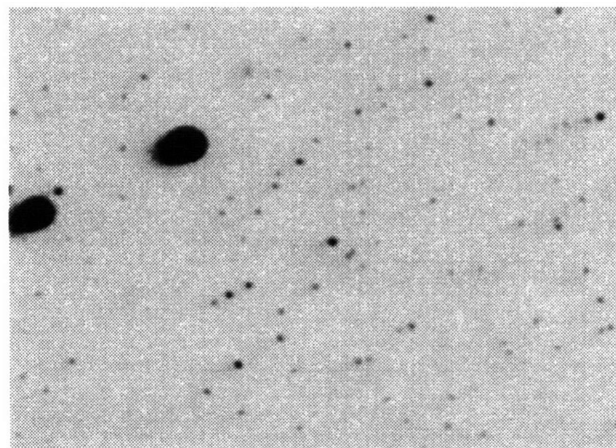

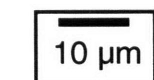


(c) Si map

Figure 6.5 SEM image and EDS element maps of an Er:Si composite deposited at room temperature for 3 hours on a Si substrate. (a) SEM image; (b) Er L X-ray map; (c) Si K X-ray map. Areas of higher concentration appear brighter in the element maps.

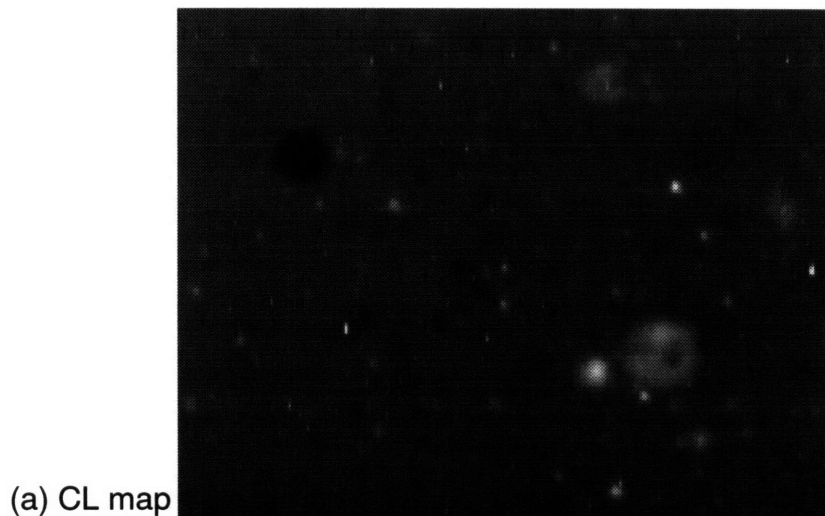


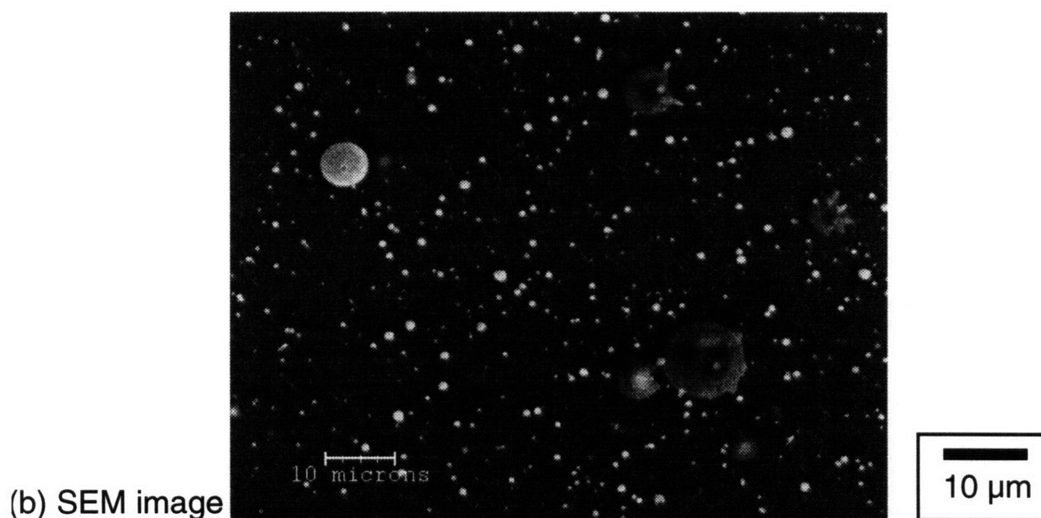


Figure 6.6 Cathodoluminescence map and SEM image of Er:Si composite. Light emission is strongest from cones formed by the rapid solidification of liquid Si droplets. The dark spot in the upper left quadrant of part (a) correponds to an Er particle, seen as a bright sphere in part (b).

and even if quantum confinement resulted in some change in the energy levels of neutral Er nanoclusters, it is unlikely that it would result in emission exactly at 1.54 μm, a transition that has already been assigned to the $^4I_{13/2} \rightarrow {^4I_{15/2}}$ transition in the $Er^{3+}$ *ion.*

It is more likely, therefore, that the luminescence mechanism in PLA-SSE Er:Si is similar to that in Er-implanted Si, and involves complexes of Er with impurities such as O, C, N or F.[6]

## 6.6 Film composition

The strong "G" line in the PL spectra of unannealed Er:Si composites shows that a high level of C is present in the codeposited Er:Si composite. In addition, the observed $Er^{3+}$ luminescence is known to be associated with Er-O complexes, and suggests that the the Er:Si composites also contain high levels of oxygen† Direct evidence for high C and O levels in the composite are seen in analyses of the composite by Auger Electron Spectroscopy (AES).

Figure 6.7 shows the atomic concentration of Er, Si, C and O in an Er:Si composite as successive layers of material were sputtered off with an $Ar^+$ ion gun. The approximate etch rate was 30Å/min. High C and O levels are recorded at the surface of the sample, prior to sputtering, because adventitious carbon and native oxide layers are present on the surface. Even after sputtering for 5 minutes, however, 20–25 at. % each of carbon and oxygen are observed in the Auger spectrum.

This result is confirmed by concentration profiles collected by XPS as well, where similar concentrations of C and O were observed in the Er:Si composite after 4–5 minutes of sputtering. XPS is ~10 times less sensitive to Er than to Si, and the main Er *4d* peak at 169 eV is broad and overlaps with shake-up and energy-loss peaks from the Si *2s* peak at 153 eV. This makes it difficult to separate the Er signal from that of Si, so quantitative Er concentration profiles were not obtainable by XPS.

In both the XPS and AES instruments, the sputter gun is at an angle to the sample, and because of the roughness of the Er:Si deposit, parts of the sample will be shadowed from the sputter gun. As a consequence, the observed C and

---

† The "C" line present in unannealed Er:Si composites is also associated with O, but this was shown to arise from C-O pairs in the Si substrate, rather than in the deposited composite.

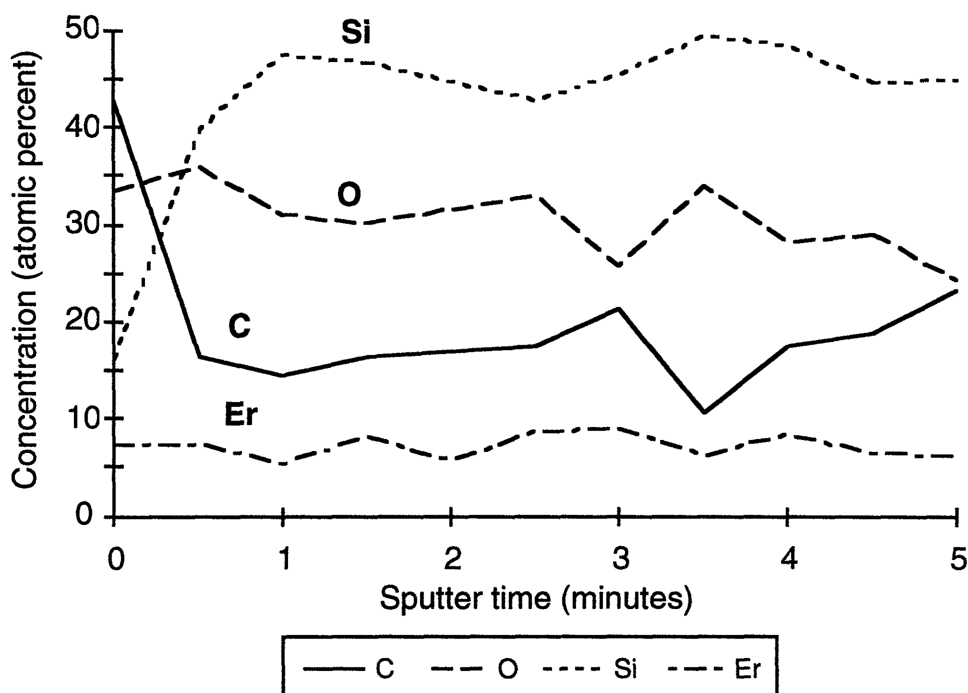


=

Figure 6.7 Auger concentration profiles for an Er:Si composite deposited on a Si wafer. Composite was annealed at 500°C for 0.5 hours prior to Auger analysis. Sputter rate is approximately 30 Å/min.

O signals overestimate the actual concentrations below the surface of the sample. Despite this caveat, it is clear that high levels of C and O are present in the deposited Si matrix.

For comparison, when $SiO_x$ composites deposited by reactive laser evaporation were analyzed by XPS, a high C level was observed at the surface due to adventitious C contaminants (pump oil, etcetera), but the C level dropped rapidly with depth and no C was detectable within 1-2 minutes of sputtering.

The He used for PLA-SSE is 99.999% pure, and both the Er and Si rods used for laser ablation are 99.99% pure, so the high level of contamination does not originate from the PLA-SSE or laser evaporation processes *per se*. In Chapter 4, it was noted that high contamination levels in Si films deposited by $Si_2H_6$ CVD were due to poor vacuum conditions in the secondary chamber. The same considerations apply for laser evaporation in the primary chamber: There is no load lock and the chamber must be exposed to atmosphere every

time a sample is mounted. This repeated contact with room air results in contamination of the chamber walls, and high residual gas levels during deposition.

In the case of $SiO_x$ deposition, the $O_2$ gas supplied to the system appears to reduce the level of C in the deposited film. Possibly, organic contaminants react with $O_2$ to evolve $CO_2$, which is released, and little C is incorporated into the growing film. No carbon removal occurs during laser evaporation of Si without added $O_2$, however, so C from organic contaminants in the chamber is incorporated into the Er:Si composites.

## 6.7 Luminescence mechanism

Apart from being enhanced by ion-implanting O, photoluminescence in Er-implanted Si can also be enhanced by ion-implanting C, N or F.[6] The strong 1.54 µm luminescence from Er:Si composites may thus be a consequence of the high concentration of C and O in the deposited composites, rather than any quantum confinement effects. Enhanced photoluminescence intensity compared to Er-implanted Si has been reported previously for Er-implanted semi-insulating polycrystalline silicon (SIPOS), which is poly-Si containing up to ~25 at. % oxygen.[11]

Nanometer-scale Er clusters are not visible by SEM at the resolution of either the secondary electron image or the EDS map. These are generated by the PLA-SSE cluster source along with the larger micron-scale particles and are incorporated into the Si host as well. Ion implantation can be used to dope Si with Er up to peak concentrations of ~ 0.5 at. %. Auger analysis showed that the Er concentration in PLA-SSE Er:Si composites was significantly higher, ~ 7 %. However, a large fraction of this is present as large Er particles. The larger micron-scale Er particles are optically inactive, and only Er dissolved in Si is responsible for luminescence. Large concentrations of C and O are also present so Er-C and Er-O complexes in the silicon must account for a large portion of the luminescence.

It is possible that small (nanometer-scale or polyatomic) Er clusters are responsible for some of the strong 1.54 µm luminescence, but it is not *necessary* to invoke any mechanism other than previously identified Er-impurity complexes to explain the luminescence from PLA-SSE Er:Si composites. Quantum confinement effects are also strongly size-dependent,

and because of the broad size distribution of PLA-SSE Si nanocrystals, photoluminescence peaks are broad, with FWHM on the order of 100 nm (Section 2.4.1) Narrow PL peaks are only seen when a narrow size distribution is achieved, as in the case of size-selected CdSe nanocrystals.[17,18] The FWHM of the 1.54 μm peak in PLA-SSE Er:Si is only 7.5 nm[12], which makes it unlikely that the PL originates from PLA-SSE Er nanoclusters which are *not* size-selected prior to deposition in the Si matrix.

That said, it should be noted that the temperature-dependence of the PL is markedly different in PLA-SSE Er:Si composites and ion-implanted Er-doped Si. The PL intensity of PLA-SSE Er:Si composites falls by a factor of 2 from 4 K to 300 K, but falls by a factor of $10^3$ for Er-implanted Cz Si. A reduced temperature dependence is also observed for Er-implanted amorphous Si,[9] so a possible explanation for the change in temperature dependence is that the disordered matrix (amorphous Si or laser-evaporated Si) has fewer competing non-radiative pathways than crystalline Si.

## 6.8 Suggested work

If Er nanoclusters are not in fact implicated in the luminescence, then subsituting the PLA-SSE cluster source with another Er souce, say a thermal or e-beam evaporator, will have little effect on the PL of Er:Si composites. Performing this experiment could therefore help to clarify whether Er nanoclusters are responsible for the enhanced 1.54 μm luminescence.

The deposited PLA-SSE Er:Si composites are very rough, with micron-scale pyramids, etc. on the surface. This is clearly detrimental to its integration with planar microelectronic or optoelectronic devices, so it would be desirable to improve the smoothness of the films. This could be achieved by using thermal or e-beam evaporation rather than laser evaporation to deposit the Si host. The enhanced Er PL in PLA-SSE composites may be related in some way to the high temperature at which liquid Si droplets hit the substrate after laser evaporation, however. If this is the case, then Er:Si composites synthesized by thermal or e-beam evaporation would not exhibit enhanced luminescence.

## 6.9 Summary

Er:Si composites were synthesized by codepositing Er from PLA-SSE with laser-evaporated Si. A 1.54 μm PL line characteristic of Er-doped Si is observed

in as-deposited PLA-SSE Er:Si composites, and the intensity of this line is increased by annealing in Ar between 200 and 1000 °C, with the maximum PL intensity observed following a 500 °C anneal. The temperature dependence of PL intensity is much smaller in PLA-SSE Er:Si composites than in Er-implanted Si, with only a 50% reduction in PL intensity as T is increased from 4 K to 300 K. The PL efficiency of PLA-SSE Er:Si composites is substantially higher than that of Er-implanted Si at the same temperature. The PLA-SSE Er:Si composites were found to contain many large particles which were formed by liquid Si droplets ejected from the target by laser vaporization and deposited on the substrate. Cathodoluminesce was localized in these Si-rich particles which shows that the luminescence is due to Er *in* Si, not to Er particles. High concentrations of C and O were evidenced by characteristic PL lines in unannealed Er:Si composites, and by Auger and photoelectron spectroscopy. The luminescence mechanism in PLA-SSE Er:Si composites has not been established, but it is most likely that high Er, C and O concentrations are responsible for the formation of a high density of optically active Er-impurity luminescence centers.

## REFERENCES


1. M. L. Mandich, W. D. Reents, and V. E. Bondybey, "Main group clusters: A review," in *Atomic and molecular clusters*, edited by E. R. Bernstein (Elsevier Science Publishers, Amsterdam, 1990), p. 69.
2. S. Wolf and R. N. Tauber, *Silicon Procesing for the VLSI Era* (Lattice Press, 1986).
3. S. M. Sze, *VLSI Technology* (McGraw-Hill, New York, 1988).
4. S. Hüfner, *Optical spectra of transparent rare earth compounds* (Academic Press, New York, 1978).
5. E. Desurvive, *Erbium-doped fiber amplifiers: principles and applications* (John Wiley & Sons, New York, 1994).
6. J. Michel, J. L. Benton, R. F. Ferrante, D. C. Jacobson, D. J. Eaglesham, E. A. Fitzgerald, Y. H. Xie, J. M. Poate, and L. C. Kimmerling, "Impurity enhancement of the 1.54-μm Er3+ luminescence in silcion," J. Appl. Phys. **70** (5), 2672 (1991).
7. B. Zheng, J. Michel, F. Y. G. Ren, L. C. Kimerling, D. C. Jacobson, and J. M. Poate, "Room-temperature sharp line electroluminescence at $\lambda = 1.54$ μm from an erbium-doped, silicon light-emitting diode," Appl. Phys. Lett. **64** (21), 2842 (1994).
8. H. Przybylinska, G. Hendorfer, M. Bruckner, L. Palmetshofer, and W. Jantsch, "On the local structure of optically active Er centers in Si," Appl. Phys. Lett. **66** (4), 490 (1995).
9. J. H. Shin, R. Serna, G. N. van den Hoven, A. Polman, W. G. J. H. M. van Sark, and A. M. Vredenberg, "Luminescence quenching in erbium-doped hydrogenated amorphous silicon," Appl. Phys. Lett. **68** (1), 46 (1996).
10. G. Davies, "The optical properties of luminescence centres in silicon," Phys. Rep. **176** (3-4), 83 (1989).
11. S. Lombardo, S. U. Campisano, G. N. van den Hoven, A. Cacciato, and A. Polman, "Room-temperature luminescence from Er-implanted semi-insulating polycrystalline

silicon," Appl. Phys. Lett. **63** (14), 1942 (1993).

12. A. Thilderkvist, J. Michel, S.-T. Ngiam, L. C. Kimmerling, and K. D. Kolenbrander, "Photoluminescence from Erbium nanoparticles embedded in a silicon matrix," in *Materials Resarch Society symposia proceeedings* (Materials Research Society, Pittsburgh, PA, (in press)), Vol. 405.
13. Y. Xia, Q. Wang, L. Mei, C. Tan, S. Yue, B. Xu, and Z. Liu, "Laser ablation of Si, Ge, $ZrO_2$, and Cu in air," Journal of Physics D (Applied Physics) **24**, 1933 (1991).
14. J. T. Cheung and H. Sankur, "Growth of Thin films by laser-induced evaporation," CRC Crit. Rev. Solid State Mater. Sci. **15**, 63 (1988).
15. D. B. Chrisey and G. K. Hubler, "Pulsed laser deposition of thin films," (John Wiley & Sons, New York, 1994).
16. F. Antoni, E. Fogarassy, C. Fuchs, J. J. Grob, B. Prevot, and J. P. Stoquert, "Pulsed excimer laser deposition of $Si_{1-x}Ge_x$ thin films," Appl. Phys. Lett. **67** (14), 2072 (1995).
17. C. B. Murray, D. J. Norris, and M. G. Bawendi, "Synthesis and Characterization of Nearly Monodisperse CdE (E = S, Se, Te) Semiconductor Nanocrystallites," J. Am. Chem. Soc. **115**, 8706 (1993).
18. D. J. Norris, M. Nirmal, C. B. Murray, A. Sacra, and M. G. Bawendi, "Size Dependent Optical Spectroscopy of II-VI Semiconductor Nanocrystallites (Quantum Dots)," Z. Phys. D **26** (1-4), 355 (1993).

# Chapter 7
# Summary

Pulsed Laser Ablation-Supersonic Expansion (PLA-SSE) has been combined with a variety of vacuum-compatible deposition techniques to synthesize novel composite materials consisting of nanoclusters embedded in a solid host matrix. Ge, Si and Er clusters were synthesized by PLA-SSE and codeposited into Si and silicon oxide hosts grown by chemical vapor deposition (CVD) and laser evaporation.

Ge:Si cluster:host composites were synthesized by depositing Ge clusters onto a heated Si wafer substrate and simultaneously depositing Si by CVD from disilane. The Ge content of the composites was approximately 1 atomic percent as determined by RBS. Rutherford backscattering and X-ray diffraction showed that the Si host was polycrystalline. Transmisson Electron Microscopy showed the presence of nanocrystalline Ge, and element maps collected by X-ray spectroscopy in a STEM showed that discrete Ge nanoparticles were embedded in the Si host matrix. No visible or near-infra-red photoluminescence was observed from Ge:Si composites or from Ge clusters deposited without a Si matrix. This was unexpected as photoluminescence had been predicted, based on theoretical calculations of quantum confinement in Ge nanoclusters, and on published reports of visible PL from Ge nanoclusters synthesized in $SiO_2$ matrices. Ge nanocrystals synthesized in solution without an $SiO_2$ matrix do not exhibit photoluminescence, however, suggesting that the PL observed from Ge:$SiO_2$ host systems in fact arose from $SiO_2$. Photoluminescence from Ge:Si composites may be absent because of poor surface passivation of the Ge nanoclusters, or because quantum confinement in Ge does not result in enhanced radiative transition probabilities or blue-shifting of the bulk band gap.

Silicon oxide host matrices were deposited by laser evaporating Si in the presence of oxygen. The deposited $SiO_x$ ($1.4 \le x \le 1.8$) oxide was sub-stoichiometric, however, and the O/Si ratio could not be increased even by varying the substrate temperature, evaporation laser power or the distance between the Si target and the substrate. X-ray photoelectron spectroscopy (XPS) showed that Si-Si as well as Si-O bonding was present in the $SiO_x$ , and XRD showed that crystalline Si particles were present. The Si crystals were not

completely oxidized even after oxidation in pure oxygen at 1000°C for 5 hours, indicating that a large proportion of the particles were at least a micron in diameter. This was confirmed by Scanning Electron Microscopy (SEM) where particles larger than 1 μm in size were observed. The shape of these particles suggested that they were created by liquid droplets ejected from the Si target and rapidly solidifying on impact with the substrate. The oxygen flux to the substrate was estimated to be insufficient to completely oxidize Si arriving at the substrate, but this flux could not be increased because the PLA-SSE cluster source has to be operated at pressures below ~$10^{-4}$ torr. The deposited $SiO_x$ matrix is therefore substoichiometric because of the presence of many large Si particles and insufficient oxygen flux during deposition. PLA-SSE Si clusters deposited without a matrix emit visible orange-red photoluminescence, but the Si:$SiO_x$ composites did not exhibit any PL either as-deposited, or after annealing in nitrogen or oxygen. This is because the $SiO_x$ matrix fails to passivate the surface of the nanoclusters, leaving a high density of dangling bonds and defects on the Si cluster surface which act as non-radiative recombination centers.

Er:Si composites were deposited by combining PLA-SSE for deposition of Er with deposition of Si by laser evaporation. Weak photoluminescence at 1.54 μm is observed in as-deposited Er:Si composites, and this PL band is strongly enhanced by annealing in $N_2$ at 500°C. The 1.54 μm luminescence band arises from intra *4f* shell transitions in $Er^{3+}$ and has been observed in other Er-doped systems. The PL intensity of PLA-SSE Er:Si falls by half from 4 K to 300 K, but this is a significantly smaller temperature effect than in Er-implanted crystalline Si, where the PL intensity falls by a factor of $10^3$ over the same temperature range. Cathodoluminescence maps of the Er:Si composite show that light emission is localized in Si particles formed by the freezing of liquid Si droplets created by laser evaporation of the Si matrix. Micron-scale Er particles do not exhibit any cathodoluminescence. Co-implantation of C or O into Er-implanted Si is known to enhance the Er-related luminescence, and high levels of C and O were detected in the PLA-SSE Er:Si composites by Auger and photoelectron spectroscopy. Luminescence from PLA-SSE Er:Si composites is therefore more likely due to Er-C and Er-O complexes than to quantum confinement of Er.

Because the PLA-SSE process is dependent on the rapid cooling achieved by the adiabatic expansion of a carrier gas into vacuum, the system has to be

kept under medium-to-high vacuum. This severely constrains any chemical reaction-based technique used to deposit a host matrix. In the case of CVD of Si from $Si_2H_6$, the maximum growth rate that could be achieved was exceedingly small, less than 0.1 μm/hr. In the case of the reactive laser evaporation of Si in oxygen to produce $SiO_x$, a sub-stoichiometric oxide was produced, partly because of the low $O_2$ flux that could be sustained in the PLA-SSE chamber. Physical vapor deposition techniques are not constrained by the low gas density and high growth rates can be achieved, as in the case of laser evaporation of Si. While it is not inherent to the PLA-SSE process, a relatively high level of contamination by C and O was experienced using the present apparatus. Fortuitously, this C and O "doping" enhanced the photoluminescence from Er:Si composites.

# Chapter 8
# Conclusions

A novel technique for synthesizing nanostructured heterocomposites was developed, and used to synthesize Ge:Si, Si:$SiO_x$ and Er:Si composites. Nanoclusters were synthesized by Pulsed Laser Ablation-Supersonic Expansion (PLA-SSE) and codeposited into host matrices deposited by chemical vapor deposition, reactive laser evaporation or laser evaporation.

Nanoclusters have previously been shown to have enhanced optical and electronic properties relative to their bulk counterparts, and these properties are strongly influenced by nanocluster surface conditions. Thus, whereas PLA-SSE Si nanoclusters deposited without a host matrix photoluminesce following passivation of their surfaces with oxide or hydride groups, Si nanoclusters codeposited in an sub-stoichiometric oxide host ($SiO_x$) do not photoluminesce. Photoluminescence from the Si:$SiO_x$ composite is quenched by a high density of non-radiative recombination sites at the Si nanocluster–$SiO_x$ host interface. A major factor in the formation of the poorly-passivated interface is the low $O_2$ flux that can be sustained during deposition because of the vacuum required by the PLA-SSE process.

Rapid cooling of a carrier gas by expansion into vacuum is essential for nanocluster synthesis by PLA-SSE, and PLA-SSE generates bare, uncapped nanoclusters *in vacuo*. This is in contrast to other quantum dot synthesis techniques such as precipitation from liquid or solid solutions, which produce encapsulated clusters. The uncapped PLA-SSE clusters can then be codeposited into a wide variety of host matrices, making PLA-SSE a very flexible base technique for fabricating nanocluster:host composites. The vacuum associated with PLA-SSE is key to its flexibility. At the same time, the vacuum impedes passivation of the nanoclusters, and limits our ability to enable quantum confinement effects from the nanoclusters.

The vacuum is not a constraint in systems with less stringent demands on interface passivation, however. For example, when PLA-SSE is combined with laser evaporation to synthesize Er:Si, the Er:Si photoluminesces more intensely than Er-doped Si synthesized by ion implantation. PLA-SSE could thus be a useful approach to developing Er-based optoelectronic and photonic materials.

# Appendices

## A.1 Disilane deposition system Standard Operating Procedure

Disilane ($Si_2H_6$) is a pyrophoric (i.e. *spontaneously flammable in air*) gas with a b.p. of -14°C. Its vapour pressure at 20°C is 3 atm. The primary hazard associated with its use is its ability to ignite spontaneously in air. Disilane must not be exposed to air, oxygen or other oxidizers except after dilution in large quantities of inert gas.

A lecture bottle of disilane is stored in the fume hood and connected to the vacuum chamber by 27 ft of 1/4 inch SS tubing. Due to the cost of venting the disilane from this length of tube after every run, the section of tube between V12 and V14 will be left filled with $Si_2H_6$ even between runs.

This document describes the normal operating procedures as well as the appropriate responses to abnormal conditions such as power failures (page 5).

Author: Shih-Tung Ngiam 66-250 x3-6633 (O) 621 3108 (H)
Revised: June 3, 1993

---

Colour Code

The 1/4 inch tubes are marked with coloured tape to indicate their normal contents. The 1/2 inch tubes are exhaust lines.

| Nitrogen | Blue |
| --- | --- |
| Disilane | Yellow-Green |

---

Initial Disilane Charge

The feed line is purged with $N_2$, pumped down, then charged with $Si_2H_6$.

Initial Conditions: V11, V12, V13, V14, V15, V16, V18, V19, V20, V21 closed.
Disilane cylinder valve closed.

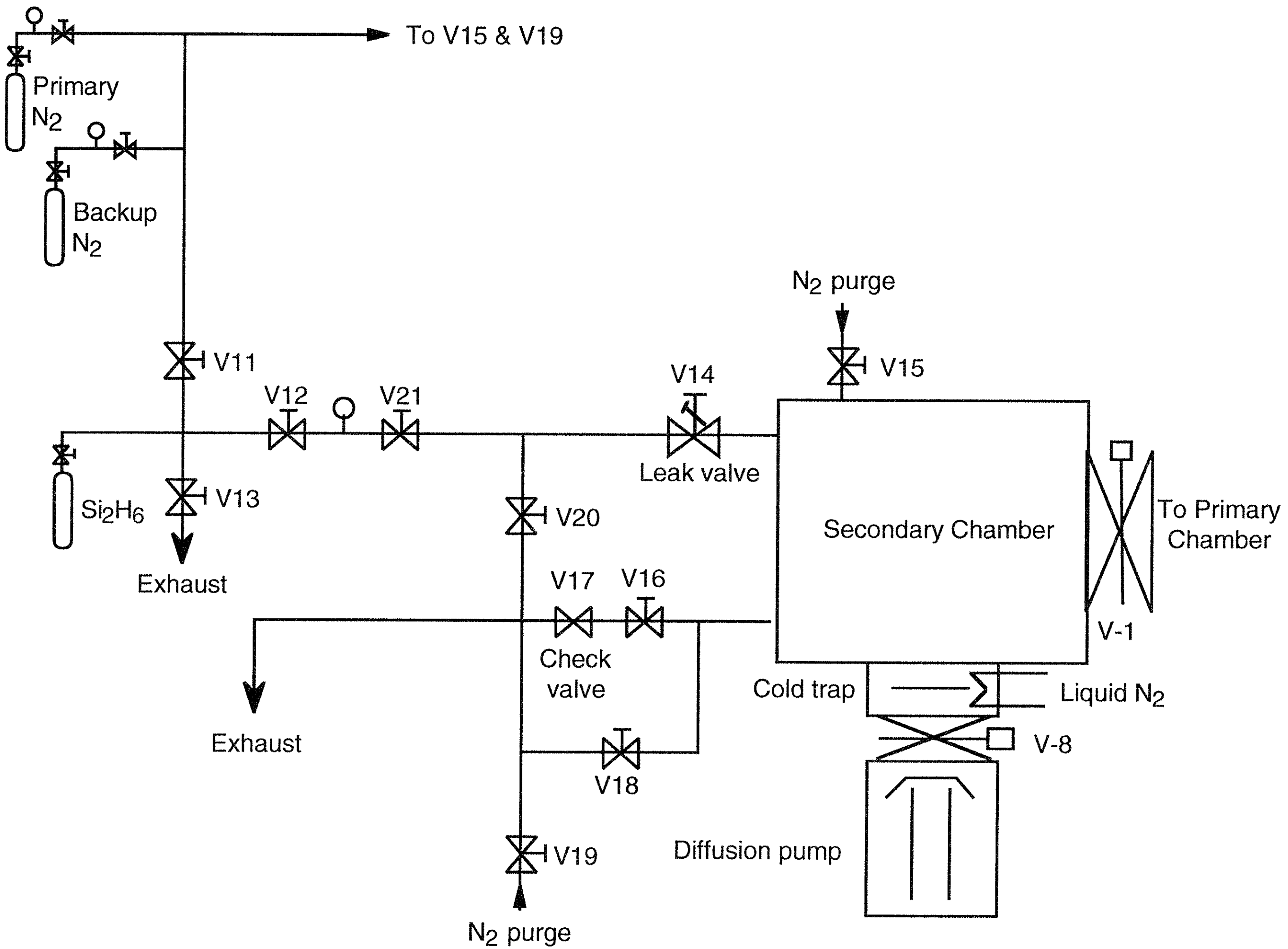


Figure A.1 Disilane gas handling system

1. Open primary $N_2$ cylinder valve; Set regulator to 40 psig; Open regulator outlet valve.
2. Rough secondary chamber to $10^{-2}$ torr according to chamber SOP.
3. Open V11, V12 and V21.
4. Open V20 to flush air from the feed line. Continue flushing for 1 minute then close V20. The feed line will now be filled with $N_2$.
5. Close V11. Leave V12 and V21 open.
6. Check that the secondary chamber is isolated from the diffusion pump. Gate valves V-1 and V-8 must be closed.
7. Open the leak valve V14 to the fully open position. The feed line will be evacuated through the secondary chamber.
8. Rough the chamber and pump down with the diffusion pump. The minimum pressure attainable will be approximately 2 x $10^{-6}$ torr after 1 hour.
9. Close V14.
10. Close V12 and V21.
11. Open $Si_2H_6$ cylinder valve. Open V12 and set the $Si_2H_6$ regulator at 5 psig
12. Open V21 to fill the feed line with disilane.
13. Close $Si_2H_6$ cylinder valve, V12 and V21.

Final conditions: V11, V12, V13, V14, V15, V16, V18, V19, V20, V21 closed.
Disilane cylinder valve closed.
Feed line filled with $Si_2H_6$ at 5 psig. Purge assembly and regulator also filled with $Si_2H_6$.

Normal Operation

Disilane is introduced into the secondary chamber at a controlled flow rate and condensed on the cold trap. Note that the secondary chamber door must be bolted closed when running disilane. This is because positive pressures will be created in the chamber during venting. The $N_2$ supply line is pressurized so that $N_2$ will be available for purging if necessary.

Inital Conditions: V11, V12, V13, V14, V15, V16, V18, V19, V20, V21 closed.
Disilane cylinder valve closed.
Feed line filled with $Si_2H_6$ at 5 psig.
Ensure that a back-up $N_2$ gas cylinder is connected to the $N_2$ manifold.

1. Open primary $N_2$ cylinder valve; Set regulator to 30 psig; Open regulator outlet valve.

2. Pump secondary chamber to $10^{-7}$ torr according to chamber SOP.
3. Fill cold trap with liquid nitrogen.
4. Open V14 at desired flow rate

Final Conditions: V11, V12, V13, V15, V16, V18, V19, V20, V21 closed.
V14 open.
The line between V21 and V14 acts as a $Si_2H_6$ reservoir from which $Si_2H_6$ is bled into the deposition chamber.

Shut-down

After completing a deposition run, the disilane trapped in the liquid $N_2$-cooled baffle must be safely vented before the secondary chamber can be opened. Positive pressures will be created in the secondary chamber during venting. The door must therefore be firmly bolted to prevent it from opening before the disilane has been completely vented.

Inital Conditions: V11, V12, V13, V15, V16, V18, V19, V20, V21 closed.
Ensure that the secondary chamber door is bolted closed.
Ensure that a back-up $N_2$ gas cylinder is connected to the $N_2$ manifold.

1. Open primary $N_2$ cylinder valve; Set regulator to 30 psig; Open regulator outlet valve.
2. Close V14.
3. Isolate secondary chamber from primary chamber and diffusion pump by closing V-1 and V-8.
4. Open V16. The check valve will now be protecting the vacuum chamber from backflow of air.
5. Gradually open V15 one full turn to backfill chamber with $N_2$. The check valve (V17) will open when the pressure within the chamber exceeds 1/3 psig.
6. Displace liquid $N_2$ from cold trap by blowing it out with house air. This will take about 1 hour.
9. Close V16.
10. Open V18 (bypass valve) to release the overpressure (1/3 psig) in the secondary chamber. Do not release the bolts on the chamber door until V18 has been opened.
11. Close V15 and V19.
12. Close V18.

Final Conditions: V11, V12, V13, V14, V15, V16, V18, V19, V20, V21 closed

Chamber will be at atmospheric pressure.
Line between V21 and V14 will still be filled with $Si_2H_6$.

Complete purge

The line between V21 and V14 is normally left filled with $Si_2H_6$. In addition, all fittings upstream of V21 (regulator and deep purge assembly) will be filled with $Si_2H_6$. When making any adjustments to the piping system, or when the $Si_2H_6$ will not be used for an extended period, the $Si_2H_6$ should be completely purged from the system.

Inital Conditions: V11, V12, V13, V14, V19, V20, V21 closed
Feed line filled with $Si_2H_6$ at 5 psig. Purge assembly and regulator also filled with $Si_2H_6$.
Ensure that a back-up $N_2$ gas cylinder is connected to the $N_2$ manifold.

1. Open primary $N_2$ cylinder valve; Set regulator to 60 psig; Open regulator outlet valve.
2. Open V19.
3. Open V11, V12 and V21. Open the regulator to its maximum setting.
4. Open V20. Flush for at least 5 minutes.
5. Close V20 and V19. The feed line, regulator and purge assembly will now be filled with $N_2$.
6. Close V11.

Final Conditions: V11, V12, V13, V14, V16, V18, V19, V20 closed
Feed line, regulator and purge assembly filled with $N_2$.

## Abnormal Events

Several modes of departure from smooth operation can be envisaged: i) diffusion pump failure, ii) building power failure, iii) $N_2$ gas supply failure, iv) sudden unexplained rise in chamber pressure

### Diffusion Pump Failure

The diffusion pump will shut down if the foreline pressure exceeds approximately 0.1 torr (a beeper will be activated when this interlock activates). The diffusion pump heater will also shut off if it overheats. No audible warning will be given in this case, but system pressure will rise, and the diffusion pump will go cold.

If a silicon deposition run is in progress, the appropriate response is to cut off disilane flow into the chamber, and to switch off the susceptor heater. The cryotrap will retain its charge of liquid $N_2$ for 6 hours.

1. Close leak valve V14.
2. Switch off power to susceptor heater.
3. Isolate secondary chamber by closing gate valves V-1 and V-8.
4. Perform normal shut-down procedure.

### Building Power Failure

Building-wide power failures occasionally occur, leading to total darkness in the laboratory. Gate valves V-1 and V-8 remain stationary in the event of power loss.

If a silicon deposition run is in progress, the appropriate response is to cut off disilane flow into the chamber, and to switch off the susceptor heater. The cryotrap will retain its charge of liquid $N_2$ for 6 hours. If power is not restored within that time, additional liquid $N_2$ should be added to ensure that condensed disilane does not evaporate.

1. Close leak valve V14.
2. Switch off power to susceptor heater. This is to ensure that the heater is not inadvertently re-energized after power is restored.
3. Perform normal shut-down procedure after power is restored.

### $N_2$ Gas Supply Failure

Nitrogen is used to dilute $Si_2H_6$ when venting the chamber and purging the feed lines. Loss of $N_2$ during a purging operation could lead to the $Si_2H_6$ concentration exceeding its lower flammability limit. To prevent this, the primary $N_2$ cylinder pressure should be at least 300 psig at the start of a run. In addition, a full back-up cylinder must always be connected to the $N_2$ manifold.

Sudden Rise In Chamber Pressure

Chamber pressure may rise suddenly during a deposition run due to a leak, evaporation of condensate in the cold trap (due to insufficient liquid nitrogen) or other reasons. Operator actions should be directed at preventing disilane ignition, and preventing excessive pressure buildup in the chamber.

1. Close leak valve V14 to cut off disilane flow into chamber.
2. Switch off power to susceptor heater
3. If the chamber pressure exceeds the TC1 set-point (TC1 light goes off)
   a. Open exhaust valve V16. This will allow the chamber to be vented if the internal pressure exceeds 1 atm (Check valve V17 opens at 1/3 psig ).
   b. Open nitrogen purge valve V15. This is to ensure dilution of $Si_2H_6$ in nitrogen.
   c. By this time, valves V-1 and V-8 should have automatically closed. Continue with normal shut-down procedure.
4. Investigate cause of pressure rise.

## A.2 Kinetic model for silicon deposition from $Si_2H_6$

Buss et al.[1] model the deposition of Si from $SiH_4$ and $Si_2H_6$, and extract kinetic parameters from experimental data for Si growth rate under a range of temperature and molecular flux conditions. The decomposition of $Si_2H_6$ is modelled with the following reaction mechanism:

$$Si_2H_6 + *{-}*{-}* \rightarrow 3SiH_2* \qquad (6)$$

$$2SiH_2* \rightarrow SiH_4 + *{-}* \qquad (4)$$

$$SiH_2* \rightarrow * + H_2 \qquad (5)$$

where the numbering system used by Buss et al. has been retained for ease of comparison. Surface species are designated with a * suffix, with no distinction being made between Si* and vacant sites represented by the * symbol.

Writing a steady-state balance for $SiH_2*$, we get

$$3\,k_3\,[Si_2H_6]\,N^3\,(1-\theta)^3 = 2\,k_4\,N^2\theta^2 + k_5\,N\,\theta$$

where $N$ is the surface site density, taken as $10^{15}$ cm$^{-2}$, $\theta$ is the surface coverage and $[Si_2H_6]$ the number density of disilane. The reactive sticking coefficient for disilane, RSC($Si_2H_6$), is defined as the Si deposition rate, in units of Si atoms cm$^{-2}$ s$^{-1}$, divided by twice the incident $Si_2H_6$ flux. With $F$ defined as the incident disilane flux,

$$RSC(Si_2H_6) = k_5'\,\theta\,/\,3F$$

and

$$\theta = \left(-\frac{a}{2} + \sqrt{\frac{a^2}{4} + \frac{b^3}{27}}\right)^{1/3} + \left(-\frac{a}{2} - \sqrt{\frac{a^2}{4} + \frac{b^3}{27}}\right)^{1/3} + 1 - \frac{2k_4'}{9\,k_6'\,F}$$

where

$$a = 3\left(1 - \frac{2k_4'}{9k_6'F}\right)\left(1 + \frac{k_5'}{9k_6'F}\right) - 2\left(1 - \frac{2k_4'}{9k_6'F}\right)^3 - 1$$

$$b = 3\left[1 + \frac{k_5'}{9k_6'F} - \left(1 - \frac{2k_4'}{9k_6'F}\right)^2\right]$$

$$k_4' \equiv k_4N^2$$

$$k_5' \equiv k_5N$$

$$k_6' \equiv 4k_6\,N^3/v$$

$v$ is the average molecular velocity, taken as $3.18 \times 10^4$ cm s$^{-1}$ for disilane. The best fit rate constants were determined from Si growth rate data using a Monte Carlo optimization procedure, and found to be

$k_4 = 2.15 \times 10^{-7} \exp(-25\,000 / RT)\ cm^2\ s^{-1}$
$k_5 = 5.34 \times 10^{13} \exp(-54\,000 / RT)\ s^{-1}$
$k_6 = 9.70 \times 10^{-43} \exp(-2500 / RT)\ cm^7\ s^{-1}$

The Si growth rate predictions shown in Figure 4.3 for the PLA-CVD system were calculated by setting F to $1.3 \times 10^{15}\ cm^{-2}\ s^{-1}$ and $2.6 \times 10^{14}\ cm^{-2}\ s^{-1}$ respectively for $P_{Si_2H_6}$ of $5 \times 10^{-6}$ and $1 \times 10^{-6}$ torr. A Si density of $5 \times 10^{22}$ atoms $cm^{-3}$ was then used to convert reactive sticking coefficients, RSC($Si_2H_6$), to film growth rates in units of μm/hr.

## A.3 Kinetic model for oxidation of Si particles

### A.3.1 Oxidation of planar Si wafers

Following the initial formation of an $SiO_2$ film on a Si wafer, thermal oxidation proceeds by the diffusion of $O_2$ through the $SiO_2$ layer to the Si-$SiO_2$ interface, where it reacts with Si to form $SiO_2$ in a first order reaction with rate constant $k$,

$$Si(s) + O_2(d) \rightarrow SiO_2(s) \qquad (7)$$

where $O_2$(d) represents molecular $O_2$ dissolved in the $SiO_2$ layer.[2]

In the initial stages of oxide growth, the growth rate is controlled by the rate of reaction at the interface while in later stages, after an $SiO_2$ film has built up, the growth rate is controlled by diffusion through the $SiO_2$ film. This is expressed in the Deal-Grove model for Si oxidation,[3] also known as the linear-parabolic model:

$$x_o^2 + A x_o = B(t + t_i) \qquad (8)$$

where $x_o$ is the thickness of the oxide layer at time $t$. The parameters A, B and $t_i$ are given by

$$A = 2\mathcal{D}(1/k + 1/h) \qquad (9)$$

$$B = \frac{2\mathcal{D}c^*}{\rho_{SiO_2}} \qquad (10)$$

$$t_i = \frac{x_i^2 + A x_i}{B} \qquad (11)$$

where $\mathcal{D}$ is the diffusion coefficient for dissolved $O_2$ in $SiO_2$, $k$ is the reaction rate constant defined above, $h$ is the mass-transfer co-efficient for diffusion of $O_2$ from the bulk of the gas to the gas-solid interface, $c^*$ is the concentration of

dissolved $SiO_2$ in the oxide layer at the gas-solid interface, $\rho_{SiO_2}$ is the molar density of $SiO_2$, and $x_i$ is the initial thickness of the oxide layer at time $t$=0.

For long oxidation times $t \gg t_i$, equation (7) reduces to the parabolic growth law,

$$x_o^2 = Bt$$

so B is called the parabolic rate constant. At short times, however, the oxide growth is described by a linear growth law,

$$x_o = (B/A)(t + t_i)$$

and the quantity (B/A) is termed the linear rate constant.

### A.3.2 Oxidation of spherical Si particles

The Deal-Grove model cannot be applied directly to the oxidation of PLA-SSE Si nanoparticles because of the curvature of the Si surface. In the planar geometry of a Si wafer, surface area remains constant with depth, but in a sphere, surface area decreases with depth (i.e., distance from the outside of the Si/$SiO_2$ sphere). In a Si sphere covered by an oxide shell, the concentration of oxidant at the Si-$SiO_2$ interface is higher than that in a slab with an oxide layer of the same thickness, leading to more rapid conversion of the sphere.

Gas-solid reactions where a solid reactant in pellet form is converted to a solid product can be modelled using the Shrinking Core Model (SCM)[4,5] which assumes that the reaction front moves into a spherical particle from the outer surface, leaving behind a product layer. The inner core of the particle is assumed to be unreacted and shrinks as the reaction progresses. In the conventional SCM, the particle size is assumed to remain fixed, but this is not the case for Si oxidation, where the molar density of $SiO_2$($3.7 \times 10^{-2}$ mol cm$^{-3}$) is smaller than that of Si($8.3 \times 10^{-2}$ mol cm$^{-3}$). The Si particle therefore expands as it is oxidized, and this must be taken into account in the kinetic model.

In Figure 8.2, $r_c$ is the radius of the unreacted core and $\delta$ the thickness of the oxide layer. The concentration of $O_2$ at the Si-$SiO_2$ interface, at the gas-solid interface, and in the bulk gas are denoted $c_i$, $c^*$ and $c_g$ respectively. Let $N_{Si}$ be the total amount of unreacted Si remaining, then $dN_{Si}/dt = \dot{N}_{Si}$ is the rate of consumption of Si. The rate of shrinkage of the unreacted core must be equal to the rate of reaction,

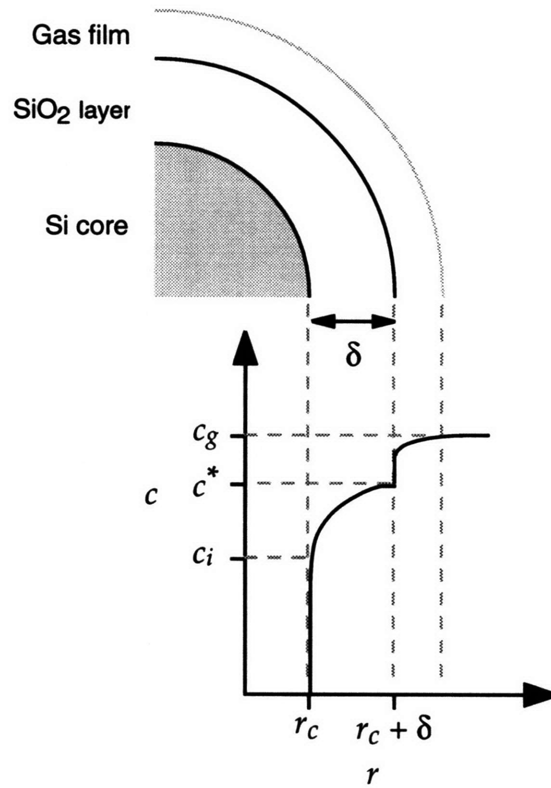


Figure A.2 Schematic representation of $O_2$ concentration, $c$, as a function of radius, $r$, for a spherical particle undergoing thermal oxidation and consisting of an unreacted Si core surrounded by a $SiO_2$ shell. $c_i$, $c^*$ and $c_g$ are the concentration of $O_2$ at the Si-$SiO_2$ interface, gas-solid interface, and bulk gas respectively. $\delta$ is the thickness of the oxide layer.

$$\dot{N}_{Si} = \rho_{Si}\left(\begin{array}{c}\text{Rate of volume change}\\ \text{of unreacted Si core}\end{array}\right) = (\text{Rate of Reaction})$$

$$\dot{N}_{Si} = \rho_{Si}\, 4\pi r_c^2\, dr_c/dt = -k\, 4\pi r_c^2\, c_i \qquad (12)$$

where $\rho_{Si}$ is the molar density of Si.

Furthermore, the rate of consumption of Si is equal to the rate of transport of $O_2$ to the Si-$SiO_2$ interface, which is equal to the product of oxygen flux and area at any $r$, where the flux is given by Fick's law as $\mathcal{D}\frac{dc}{dr}$,

$$\dot{N}_{Si} = -\,4\pi r_c^2\, \mathcal{D}\frac{dc}{dr} \qquad (13)$$

Integrating in $r$ from $r_c$ to $r_c+\delta$ and in $c$ from $c_i$ to $c^*$,

$$\dot{N}_{Si} \int_{r_c+\delta}^{r_c} \frac{dr}{r^2} = -4\pi \mathcal{D} \int_{c_i}^{c^*} dc$$

$$\dot{N}_{Si} \left( \frac{1}{r_c} - \frac{1}{r_c+\delta} \right) = 4\pi \mathcal{D} \left( c^* - c_i \right) \quad (14)$$

From (12), $c_i = \dfrac{-\rho_{Si}\, 4\pi r_c^2\, dr_c/dt}{k\, 4\pi r_c^2}$ and substituting this into (13), we get

$$\frac{dr_c}{dt} \left( r_c - \frac{r_c^2}{r_c+\delta} - \frac{\mathcal{D}}{k} \right) = \frac{\mathcal{D}}{\rho_{Si}} c^* \quad (15)$$

To account for the volume change of oxidation, equate the moles of Si consumed to the moles of $SiO_2$ produced,

$$\rho_{Si} \left( \begin{matrix} \text{Original volume of sphere} \\ -\text{ volume remaining} \end{matrix} \right) = \rho_{SiO_2} \left( \text{Volume of } SiO_2 \text{ shell} \right)$$

$$\rho_{Si} \frac{4}{3}\pi \left( r_o^3 - r_c^3 \right) = \rho_{SiO_2} \frac{4}{3}\pi \left( (r_c+\delta)^3 - r_c^3 \right)$$

to get an expression for $\delta$, the thickness of the oxide layer,

$$(r_c + \delta)^3 = \mu r_o^3 + (1-\mu) r_c^3$$

where $\mu$ is the ratio of the molar densities of Si and $SiO_2$, $\mu = \rho_{Si}/\rho_{SiO_2}$.

Rewriting (15) in terms of $\mu$ and the linear and parabolic rate constants from the Deal-Grove model (the resistance due to gas-phase mass transfer, $1/h$, is assumed to be negligible),

$$\left( r_c - \frac{r_c^2}{\left( \mu r_o^3 + (1-\mu) r_c^3 \right)^{1/3}} - \frac{A}{2} \right) dr_c = \frac{B}{2\mu} dt \quad (16)$$

The indefinite integral of the left hand side is

$$-\frac{A}{2} r_c + \frac{1}{2} r_c^2 + \frac{\left( \mu r_o^3 + (1-\mu) r_c^3 \right)^{2/3}}{2\,(\mu-1)}$$

and taking the definite integral of (16) over the interval $[r_o, 0]$ in $r_c$, and $[0,\tau]$ in $t$,

$$\tau = \frac{\mu}{B} \left( \frac{\mu^{2/3} - \mu}{\mu - 1} r_o^2 + A\, r_o \right) \quad (17)$$

$\tau$ thus represents the time required for complete oxidation of a Si sphere with original radius $r_o$. as a function of the (temperature- and pressure-dependent) Deal-Grove parameters and $\mu$, which accounts for the expansion of Si upon oxidation.

In the limit $\mu = 1$, i.e., no volume change on reaction, equation (17) simplifies to

$$\tau = \frac{r_o^2}{3B} + \frac{A}{B} r_o$$

or,

$$\tau = \frac{\rho_{SiO_2}}{6\,\mathcal{D}c^*} r_o^2 + \frac{\rho_{SiO_2}}{k c^*} r_o$$

which is identical to the standard form of the Shrinking Core Model, where the first R.H.S. term represents the time constant for diffusion through the oxide layer, and the second term represents the time constant for reaction.[4,5]

This model assumes that the oxide shell is able to rearrange itself by viscous flow to accomodate the expansion of the inner core, and that the rate constants and physical properties of the Si and $SiO_2$ are unaffected by stress within the particle. Several authors have found, however, that the oxidation of sub-micron Si cylinders and spheres is retarded relative to the oxidation of a planar wafer.[6-9] This is attributed to stress-induced changes in the reaction rate constant, the solubility and diffusivity of $O_2$ in oxide, and the viscosity of the oxide. In addition, I assume that there is negligible mass transfer resistance between the surface of the particle and the bulk of the gas stream. While this is usually true in a gas-solid reactor, in this system the Si particles are embedded in an $SiO_x$ film, which may present a significant obstacle to $O_2$ diffusion. Equation (17) would thus underpredict the time required for total oxidation of a Si particle.

## REFERENCES


1. R. J. Buss, P. Ho, W. G. Breiland, and M. E. Coltrin, "Reactive sticking coefficients for silane and disilane on polycrystalline silicon," J. Appl. Phys. **63** (8), 2808 (1988).
2. E. A. Irene, "Models for the oxidation of silicon," CRC Crit. Rev. Solid State Mater. Sci. **14** (2), 175 (1988).
3. S. Wolf and R. N. Tauber, *Silicon Procesing for the VLSI Era* (Lattice Press, 1986).
4. O. Levenspiel, *Chemical Reaction Engineering*, 2nd ed. (John Wiley & Sons, New York, 1972).
5. O. Levenspiel, *The Chemical Reactor Omnibook* (OSU Bookstores, Inc., Corvallis, Oregon, 1993).
6. D. B. Kao, J. P. McVittie, W. D. Nix, and K. C. Saraswat, "Two-dimensional oxidation of silicon- I. Experiments," IEEE Trans. Electron Devices **ED-34** (5), 1008 (1987).
7. D. B. Kao, J. P. McVittie, W. D. Nix, and K. C. Saraswat, "Two-dimensional oxidation of silicon- II. Modeling stress effects in wet oxides," IEEE Trans. Electron Devices **ED-35** (1), 25 (1987).

8. H. I. Liu, N. I. Maluf, R. F. W. Pease, D. K. Biegelsen, N. M. Johnson, and F. A. Ponce, "Oxidation of sub-50 nm Si columns for light emission study," J. Vac. Sci. Technol. B (1992).
9. R. Okada and S. Iijima, "Oxidation property of silicon small particles," Appl. Phys. Lett. **58** (15), 1662 (1991).